PERMEABILITY OF HYPOEUTECTIC ALUMINUM ALLOYS

by

Ehsan Khajeh

A THESIS SUBMITTED IN PARTIAL FULFILLMENT OF THE REQUIREMENTS FOR THE DEGREE OF

DOCTOR OF PHILOSOPHY

in

The Faculty of Graduate Studies

(Materials Engineering)

THE UNIVERSITY OF BRITISH COLUMBIA
(Vancouver)

July 2011

© Ehsan Khajeh, 2011

Abstract

The interdendritic permeability is a critical parameter that defines the feedability of the mushy zone during solidification. In this study, a theoretical expression to describe the evolution of permeability throughout the complete solidification range (from dendritic to dendritic/eutectic) of hypoeutectic aluminum alloys has been derived, verified and validated through physical and numerical modeling. The permeability of the primary, equiaxed, dendritic phase has been characterized using geometries obtained by X-ray microtomographic analysis of Al-4.5wt%Cu alloy samples quenched at different temperatures after the start of solidification. The permeability during equiaxed eutectic solidification was characterized on simulated dendritic/eutectic microstructures predicted using a Cellular Automaton technique. For both the dendritic and dendritic/eutectic structures, the permeability was characterized i) physically using large-scale analogues of the characterized microstructures and ii) numerically by predicting the flow through the simulated microstructures. The microstructural parameters were then linked to more practical parameters available in solidification models through i) developing an inverse analysis technique to characterize eutectic solidification and ii) development of a geometric model for dendritic solidification. The permeability values determined through physical and numerical modeling are in good agreement with each other and are consistent with the mathematical expression. The proposed permeability expression is valid over the complete solidification range and for a wide range of compositions. The expression reduces to the conventional Carman-Kozeny expression during dendritic solidification and/or dendritic/eutectic solidification with low density of eutectic grains. However, it deviates from the conventional Carman-Kozeny expression as the density of eutectic grains increases.

Preface

The following journal papers have been arisen from the work presented in dissertation. With the exception of my supervisor, Dr. Daan Maijer, who commented on experimental and numerical procedures, analysis methods, and results interpretation, I am the primary contributor to the work assembled below.

1. Khajeh E, Maijer DM, "Numerical determination of permeability of Al-Cu alloys using 3D geometry from X-ray microtomography", **Materials Science and Technology**, (2010) 26, pp. 1469-1476.
2. Khajeh E, Maijer DM, "Physical and numerical characterization of the near-eutectic permeability of Al-Cu alloys", **Acta Materialia**, (2010) 58, pp. 6334-6344.
3. Khajeh E, Maijer DM, "Inverse analysis of eutectic nucleation and growth kinetics in hypoeutectic Al-Cu alloys", **Metallurgical and Materials Transactions A**, (2011) 42, pp.158-169.
4. Khajeh E, Maijer DM, "Permeability of dual structured hypoeutectic aluminum alloys", **Acta Materialia**, (2011) 59, pp. 4511-4524.

Chapter 2 is based on papers "1", "2" and "3". Chapter 3 is based on papers "1", "2", and "4". Chapter 4 is based on papers "1" and "2". Chapter 5 is based on paper "4". Check the first pages of these chapters to see footnotes with similar information.

Table of Contents

Abstract ii
Preface iii
Table of Contents iv
List of Tables vi
List of Figures vii
Acknowledgements xi
Dedication xii
1 Introduction 1
1.1 Defects in aluminum alloy casting 1
1.2 Solidification mode 1
1.3 Feeding mechanisms 3
1.4 Permeability 6
1.4.1 Analytical determination of the permeability 6
1.4.2 Experimental determination of the permeability 8
1.4.3 Numerical determination of permeability 16
1.4.4 Summary of available research on permeability determination 27
1.5 Microstructure characterization 28
1.5.1 Experimental characterization 28
1.5.2 Numerical simulation 31
1.6 Scope and objective of thesis 33
2 Microstructure Characterization 36
2.1 Experimental characterization of dendritic solidification 37
2.1.1 Near-eutectic microstructure of Al-Cu alloys 37
2.1.2 Microstructure evolution during solidification of Al-4.5wt%Cu 42
2.2 Numerical characterization of eutectic solidification 52
2.2.1 Experimental procedure 53
2.2.2 Numerical methods 60
2.2.3 Results and discussion 68
2.3 Summary 79
3 Physical and Numerical Characterization of Permeability 81
3.1 The near-eutectic permeability of Al-Cu alloys 82
3.1.1 Numerical model 82
3.1.2 Physical model 85
3.1.3 Results and discussion 90
3.2 Permeability evolution during equiaxed dendritic solidification 96
3.2.1 Physical determination of permeability 96
3.2.2 Numerical determination of permeability 97
3.2.3 Comparison of physical and numerical permeabilities 99
3.3 Permeability evolution during equiaxed eutectic solidification 100
3.3.1 Physical determination of permeability 102
3.3.2 Numerical determination of permeability 104
3.3.3 Comparison of physical and numerical permeabilities 105

3.4 Summary 106
4 Permeability of Equiaxed Dendritic Structures 107
4.1 The near-eutectic permeability of Al-Cu alloys 108
4.1.1 Effect of mesh 108
4.1.2 Comparison with conventional permeameter measurements 110
4.2 Permeability of equiaxed dendritic structures during solidification of Al-4.5wt%Cu 112
4.2.1 Comparison with related studies 112
4.2.2 Extension to macroscale models 114
4.3 Summary 115
5 Permeability of Dual Structured Hypoeutectic Aluminum Alloys 117
5.1 Theory 118
5.1.1 Permeability based on Brinkman-Darcy equation 118
5.1.2 Extension to dendritic/eutectic structure 120
5.1.3 Extension to equiaxed dendritic structure 123
5.2 Verification of the dual structured permeability expression 124
5.3 Permeability prediction via mathematical expression for hypoeutectic alloys 126
5.4 Comparison with Carman-Kozeny expression 127
5.5 Extension to macroscale models 131
5.6 Summary 132
6 Concluding Remarks 134
6.1 Summary and conclusions 134
6.1.1 Microstructure characterization 134
6.1.2 Physical and numerical characterization of permeability 135
6.1.3 Mathematical expression for predicting the permeability 136
6.2 Future work 138
References 139

List of Tables

Table 2.1 Near-eutectic microstructural parameters of Al-Cu alloys 41
Table 2.2 Microstructural parameters during solidification of Al-4.5wt%Cu alloy 47
Table 2.3 Description of experimental conditions 53
Table 2.4 Chemical composition of cast samples 56
Table 2.5 Experimentally measured parameters and calculated fraction solid for quenched samples listed in Table 2.3. 70
Table 2.6 Obtained parameters through employing the inverse algorithm 74
Table 2.7 Calculated parameters using β_q values in Table 2.6. 74
Table 2.8 Calculated parameters using the average of β_q values in Table 2.6. 79
Table 3.1 Numerically and physically determined permeabilities of near-eutectic aluminum-copper samples. 90
Table 3.2 Numerical and physical permeabilities 100
Table 3.3 Numerical and physical permeabilities for Al-20wt%Cu with N_v=90 mm^{-3}. Reported values are for unscaled microstructure. 105
Table 4.1 Calculated permeability and microstructural length scale for unstructured and uniform meshes. 110

List of Figures

Figure 1.1 Schematic of freezing mode in alloys having a) short, b) intermediate, and c) long freezing range [2]. 2
Figure 1.2 Forms of shrinkage in sand cast alloys with a) long, and b) short freezing range [2]. 3
Figure 1.3 Schematic representation of the feeding mechanisms in a solidifying casting [6]. 4
Figure 1.4 Interdendritic feeding in a) columnar dendrites and flow parallel to the axis of dendrites, b) columnar dendrites and flow normal to the axis of dendrites, and c) a network of equiaxed dendrites. 5
Figure 1.5 Schematic illustration of the experimental setup used for measurement of interdendritic permeability in the mushy zone of Pb–Sn alloys [29]..... 9
Figure 1.6 Variation of a) molten metal height in outlet pipe, and b) –ln(1-βh) with time for Pb-25wt%Sn at testing temperature of 185^{o}C [29]. 11
Figure 1.7 Typical microstructure of Pb-25wt%Sn a) before and b) after the permeability test [29]. 12
Figure 1.8 Plot of the dimensionless permeability, KS_v^2, as a function of volume fraction of solid, g_s. Different experimental results have been compared with the Carman-Kozeny expression with $k_C=5$. 14
Figure 1.9 Effect of particle distribution on normalized permeability of cylindrical fiber arrays. a) Fully random, b) square packing with random location, c) square packing with random size, and d) square packing with random size and location [40]. 17
Figure 1.10 3D illustration of perturbation in FCC alloys with preferred growth direction of <100>. P_d is the extent of dendrite distention versus a sphere with the same volume and the radius of R_d [29]. 18
Figure 1.11 The flow cell, used to compute the permeability [29]. 19
Figure 1.12 Iso-pressure map for a typical microstructure [29]. 19
Figure 1.13 Estimated curve for K(f_s,*Pe*). The coefficient of correlation (R^2) for this estimation was 0.951..... 20
Figure 1.14 Simulated evolution of an equiaxed dendrite for an Al-3%Cu-3%Si alloy at effective solid fractions of 0.001, 0.01, 0.06 and 0.55..... 21
Figure 1.15 Determined values of KS_v^2 versus solid fraction compared with values expected from the Carman-Kozeny expression. 22
Figure 1.16 Cross-section of a flow cell for Pb-Sn alloy (right) and steel (left). The direction of flow is normal to the image. 23
Figure 1.17 Dimensionless permeability for flow parallel to the axis of dendrites assuming sinusoidal perturbation along the axis of the dendrite (*a* is the amplitude). 24
Figure 1.18 Velocity vectors resulted from FE simulation of fluid flow around dendritic structure..... 25
Figure 1.19 Dimensionless permeability for flow normal to the axis of dendrites. Results have been compared with two typical geometries. 25
Figure 1.20 Illustration of four experimental approaches to X-ray microtomography data collection: a) pencil, b) fan, c) parallel, and d) cone beam methods. 'P' is X-ray source, 'C' is

collimator, ‘O’ is object being imaged, ‘x2’ is axis about which sample is rotated to produce different views required for reconstruction, ‘S’ is slit, and ‘D’ is detector. 30
Figure 2.1 Schematic of a section of the mold and chill used to create tapered cylindrical casting. Sample (S) locations identified relative to chill. Units are in millimeters. 38
Figure 2.2 3D representation of the primary Al phase and mid-length cross-sectional slice extracted from XMT data for (a) Al–12 wt.% Cu, 50 mm from chill; (b) Al–19 wt.% Cu, 50 mm from chill; and (c) Al–19 wt.% Cu, 10 mm from chill. 40
Figure 2.3 Isolated liquid fraction as a function of microstructural length scale, S_v^{-1}, for the different Al–Cu alloys analyzed in this study. Distance from the chill has been specified.... 41
Figure 2.4 Schematic of the experimental setup used to produce castings for thermal analysis, XMT analysis, and microstructural analysis. 43
Figure 2.5 Measured temperature histories of baseline (non-quenched) samples with mold diameters of 19 and 29 mm. Arrows identify the temperatures at which samples have been quenched. 44
Figure 2.6 Example cross-sectional slices extracted from XMT analysis of the quenched samples for the mold diameters of 29 mm (a, b and c) and 19 mm (d, e and f). The quench temperatures were (a) 915 K, (b) 910 K, (c) 893 K, (d) 915 K, (e) 910 K, and (f) 883 K. 45
Figure 2.7 (a) Example cross-sectional slice extracted from the XMT data for the sample with a mold diameter of 29 mm and a quench temperature of 910 K. (b) and (c) are processed images of (a) after 1 and 4 segmentation steps, respectively. 46
Figure 2.8 Solid fraction versus temperature for the samples listed in Table 2.2. Solid line and dash line represent the Scheil model and Lever rule, respectively. 48
Figure 2.9 SDAS versus the inverse of solid/liquid interfacial area per unit volume of solid (S_v^{-1}) for samples listed in Table 2.2. Dash line represents S_v^{-1} variation with SDAS (d_2) assuming a cylindrical shape for dendrite arms (i.e. $S_v^{-1} = d_2/4$). 49
Figure 2.10 2D images extracted from XMT data showing different coarsening mechanisms in the scale of dendrite arms: (a) remelting of smaller dendrite arms; (b) joining of the tips of dendrite arms. 50
Figure 2.11 S_v^{-1} versus the cube root of time spent in the solid/liquid zone ($t^{1/3}$) for samples listed in Table 2.2. Dash line represents a fitted curve in the form of $S_v^{-1} = Bt^{1/3}$ resulting a B value of 4.2 μm $s^{-1/3}$. 52
Figure 2.12 Schematic of the experimental set-up used to produce castings for thermal analysis, XMT analysis and microstructural analysis. Five air channels, each with 6 nozzles were equally spaced around the copper mold and were activated for samples 1 and 2. 54
Figure 2.13 Measured temperature history for non-quenched samples listed in Table 2.3. .. 55
Figure 2.14 a) Cooling curve, first derivative and Newtonian zero curve, and b) calculated evolution of solid fraction with time and temperature for sample 3. 58
Figure 2.15 3D representation of the primary Al phase extracted from XMT data for a) sample 3, and b) sample 6. The cube edge length is 1 mm. 60
Figure 2.16 Example application of periodic boundary condition to a 2D computational domain where grain 1 grows out of the domain and a new grain (grain 2) is introduced on the opposite side with its center outside the domain. Grain 1 has the same distance (L) from right side as grain 2 has from the left side. 63
Figure 2.17 Variation of a) Cu, Si, Mg and Zn, and b) Fe and Mn concentration in the liquid with temperature for the alloy listed in Table 2.4. 65

Figure 2.18 Variation of solid fraction with temperature for the alloy listed in Table 2.4. The plot also contains the stability temperature of different phases and eutecic temperature of binary Al-Cu alloy (Dash-Dot line). 66
Figure 2.19 SEM micrographs of quenched sample 4 with the magnification of a) 200X and b) 800X. "A" is the primary Al phase, "B" is the pre-quench coarse Al-Al_2Cu eutectic, and "C" is the post-quench fine eutectic structure..... 69
Figure 2.20 Variation of residuals (Equation 2-13) for samples 1, 3, 4, and 6..... 73
Figure 2.21 Predicted microstructure of sample 6 at solid fraction of a) 0.54, b) 0.70, and c) 0.86. The cube edge length is 1 mm. 75
Figure 2.22 Predicted solidified microstructure of sample a) 6, b) 3, and c) 1. The cube edge length is 1 mm..... 76
Figure 2.23 Evolution of the calculated β_q parameters as a function of computational domain size with $N \times N \times N$ cubic cells of 5.55 μm. 78
Figure 3.1 (a) 2D section of Al–19wt%Cu (30 mm) microstructure from original voxel based geometry, (b) Marching square (2D equivalent of Marching–Cube) transformation of (a), (c) simplified triangulated surface and (d) final mesh 84
Figure 3.2 (a) Surface-based (triangulated interface) representation of Al-12 wt%Cu, 50 mm from chill, with an edge length of 1 mm; (b) polyamide replica of (a) with an edge length of 50 mm. 86
Figure 3.3 Layout of the apparatus built to measure the permeability of replica samples showing the cross-section area surrounding the sample holder (Section A–A) and close-up image of sample inside the holder (Section B–B). 88
Figure 3.4 Pressure gradient in the x-direction, measured for two replicas of Al–12 wt.% Cu (30 and 50 mm from chill) vs. viscosity multiplied by the superficial velocity. The slope of each line corresponds to the inverse of the permeability resulting in K_{xx} of 1.37×10^{-8} and 3.66×10^{-8} m^2 for samples, 30 and 50 mm from chill (samples #5 and #7 in Table 3.1), respectively. 92
Figure 3.5 Pressure contours for a) Al-12wt%Cu, 50 mm from chill, and b) Al-19wt%Cu, 50 mm from chill. An inlet condition of superficial velocity (q) equal to a) 0.045 m/s and b) 0.032 m/s was applied in z-direction. The calculated pressure drop was a) 9.4×10^4 Pa, and b) 1.5×10^4 Pa resulting in a permeability of a) $K_{zz}=3.35\times10^{-8}$ m^2 (sample #7 in Table 3.1), and b) $K_{zz}=1.46\times10^{-7}$ m^2 (sample #14 in Table 3.1)..... 93
Figure 3.6 (a) Surface-based (triangulated interface) representation of the microstructure of a sample cast with a mold diameter of 29 mm and quenched at 898 K. (b) SLS replica of (a). 98
Figure 3.7 Simulated pressure contour for the unstructured mesh of a domain corresponding to a sample cast with a mold diameter of 29 mm and quenched at 898 K. An inlet condition of superficial velocity equal to 1.0 mm/s was applied in the z-direction resulting in a permeability of $K_{zz}=6.3\times10^{-12}$ m^2..... 99
Figure 3.8 Predicted microstructure for Al-20wt%Cu with N_v=50 mm^{-3} at solid fraction of a) 0.6, b) 0.7, c)0.8, and d) 0.9. In the 3D maps, the primary phase is grey, the remaining liquid has been removed, and the colored phase represents the eutectic phase with different colors for each index factor, i.e. each grain. The cube edge length is 1 mm..... 101
Figure 3.9 (a) Surface-based (triangulated interface) representation of solidifying microstructure for Al-20wt%Cu with N_v=90 mm^{-3} at solid fraction of 0.73, with the edge length of 1 mm and (b) SLS replica of (a) with the edge length of 50 mm..... 103

Figure 3.10 Simulated pressure contour for solid sample in Fig. 4 for flow in x-direction. An inlet condition of superficial velocity equal to 1 mm/s was applied in x-direction resulting in a permeability of $K_{xx}=2.71\times10^{-11}$ m^2..... 104
Figure 4.1 Dimensionless permeability versus effective solid fraction. Blue crosses represent measured permeability normalized with S_v obtained from unstructured mesh (data in Table 3.1); Closed (red) circles represent calculated permeability for unstructured mesh geometries with S_v obtained from the mesh (data in Table 3.1); Closed diamonds represent calculated permeability for uniform mesh with S_v obtained from uniform mesh (data in Table 4.1); and open diamonds are results reported by Brown et al. (2002). Lines indicate dimensionless permeability based on the Carman-Kozeny expression with k_C equal to *1*, *3* and *5*. 109
Figure 4.2 Comparison of dimensionless numerical and measured permeabilities with experimental data obtained from permeameter measurements. 111
Figure 4.3 Comparison of dimensionless numerical and physical permeabilities with various reported results. Lines represent dimensionless permeability based on the Carman–Kozeny expression with k_C = 1, 3 and 5. 113
Figure 4.4 Comparison of the variation of calculated permeability based on the Carman-Kozeny expression as a function of solidification time with physically and numerically characterized permeabilities..... 115
Figure 5.1 The "real microstructure" of hypoeutectic aluminum alloy during equiaxed eutectic solidification is regarded as a "dendritic network" overlaid by a "eutectic network". The "hypothetical microstructure" is defined for this analysis in which the void space of the "eutectic network" is filled with the "dendritic network". The geometries of flow channels in both real and hypothetical microstructures are the same. 121
Figure 5.2 G(θ) function (refer to Equation 5-3) and $1/\theta^2$ versus θ. G(θ) is converged to 1/3 when $\theta\rightarrow0$ and $1/\theta^2$ when $\theta\rightarrow\infty$. 122
Figure 5.3 Dimensionless permeability versus solid fraction for eutectic network with four distributions of grains location. Line indicates dimensionless permeability based on the Carman-Kozeny expression for packed beds (refer to Equation 5-16)..... 125
Figure 5.4 Absolute permeability versus solid fraction for Al-20wt%Cu eutectic. Closed symbols represent the numerically determined permeabilities for N_v equal to 6, 50, and 90 mm^{-3}. Open circles with error bars represent measured permeability for N_v equal to 90 mm^{-3}. Lines indicate permeability based on the Equation 5-17 for N_v equal to 0.1, 1, 6, 50, and 90 mm^{-3}. 127
Figure 5.5 Dimensionless permeability versus solid fraction for Al with 12, 20, and 25 wt%Cu alloys for N_v equal to a) 90 mm^{-3}, and b) 0.1 mm^{-3}. Symbols represent the numerically determined permeabilities. Solid lines represent calculated permeabilities from Equation 5-17 for Al with 12, 20 and 25 wt%Cu alloys and normalized with S_v obtained from triangulated microstructure, i.e. CA simulation. Dash lines indicate dimensionless permeability based on the Carman-Kozeny expression with k_C equal to 1, 2.5 and 5. 128
Figure 5.6 Variation of θ versus solid fraction for Al with 12, 20, and 25 wt%Cu alloys. Lines represent calculated θ from Equation 5-19 for N_v equal to 0.1 and 90 mm^{-3}. 131

Acknowledgements

I would like to take this opportunity to express my utmost gratitude toward my supervisor, Dr. Daan Maijer for his continuous trust, patience, and guidance throughout the course of this work. My sincere thank goes to Dr. Andre Phillion whose efforts made XMT characterization possible. I also acknowledge Prof. Steve Cockcroft, Prof. David Dixon and Prof. Akram Alfantazi for their valuable comments.

I would like to thank all staff members in the Department of Materials Engineering at The University of British Columbia for their assistance on my research work. My especial thanks to all colleagues and officemates for providing a friendly environment that I was always pleased to work in. Natural Sciences and Engineering Research Council of Canada (NSERC) is greatly acknowledged for financial support.

Special thanks are owed to my parents, who have supported me throughout my years of education.

To my parents

1 Introduction

1.1 Defects in aluminum alloy casting

The auto industry is moving toward increased usage of lightweight aluminum alloy castings for many components previously made from steel and cast iron. Examples include cylinder heads, engine blocks, suspension components, brake components, and wheels. In many cases the mechanical properties of the cast aluminum parts are adequate; however, in some applications, porosity and segregation in the cast microstructure undermine the mechanical performance. The mechanisms governing the formation of these kinds of defects in castings is complex owing to its dependence on the interaction of a number of phenomena occurring during solidification [1, 2]. Among the contributing phenomena, the feeding behavior of compensatory flow due to the solidification shrinkage demand plays an important role.

1.2 Solidification mode

During the solidification of alloys, the variation of solute concentration ahead of the solid–liquid interface causes the evolving solid phase to form as dendrites. The volume change associated with the liquid to solid transformation must be compensated for by a flow of liquid metal through the interdendritic channels. The resistance of flow through the solid network causes a pressure drop in the liquid, which under the right conditions leads to pore nucleation and growth [3, 4]. The resistance of a solidifying microstructure is highly dependent on the solidification mode. Alloys can be classified into three types based on their freezing ranges. This classification is not precise, but the general solidification mode of each

type is illustrated in **Figure 1.1** [2]. In short freezing range alloys, a short crystalline growth front helps keep liquid metal in contact with the last solidifying region. This encourages directional solidification along with small temperature gradients in the solidifying casting. As the freezing range increases, feeding becomes more difficult. The various solidification modes result in very different typical shrinkage configurations in the casting and riser (**Figure 1.2**). Consequently, the design engineer is presented with distinctly different problems to overcome in the riser and casting sections depending on the freezing range of the alloy. Selection of an appropriate design depends largely on the ease of promoting directional solidification. It is important to note that other material and process variables such as metal and mold conductivity, metal superheating, mold pre-heat and solidification temperature also affect the development of directional solidification[2].

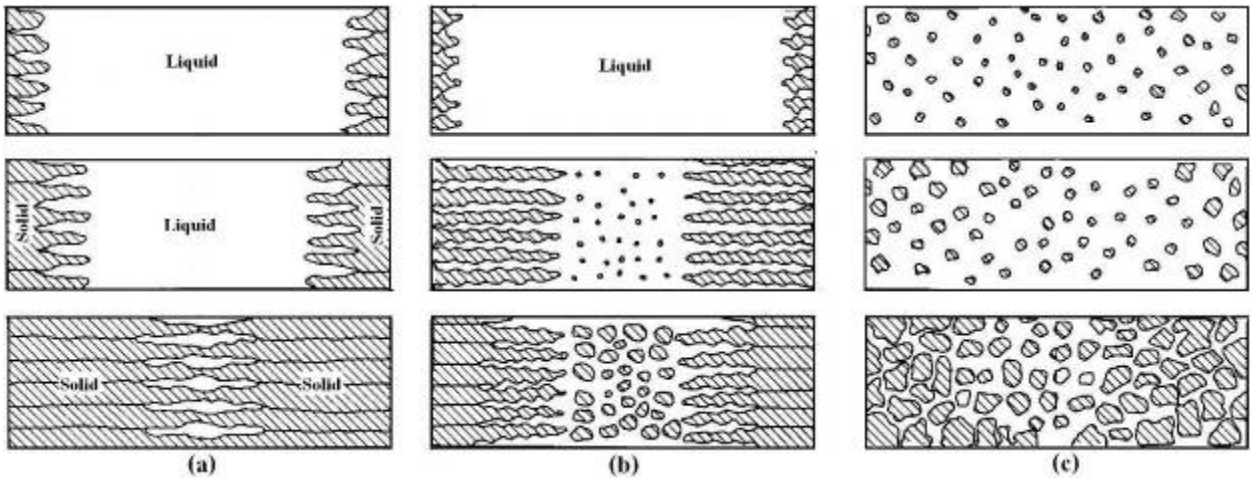

Figure 1.1 Schematic of freezing mode in alloys having a) short, b) intermediate, and c) long freezing range [2].

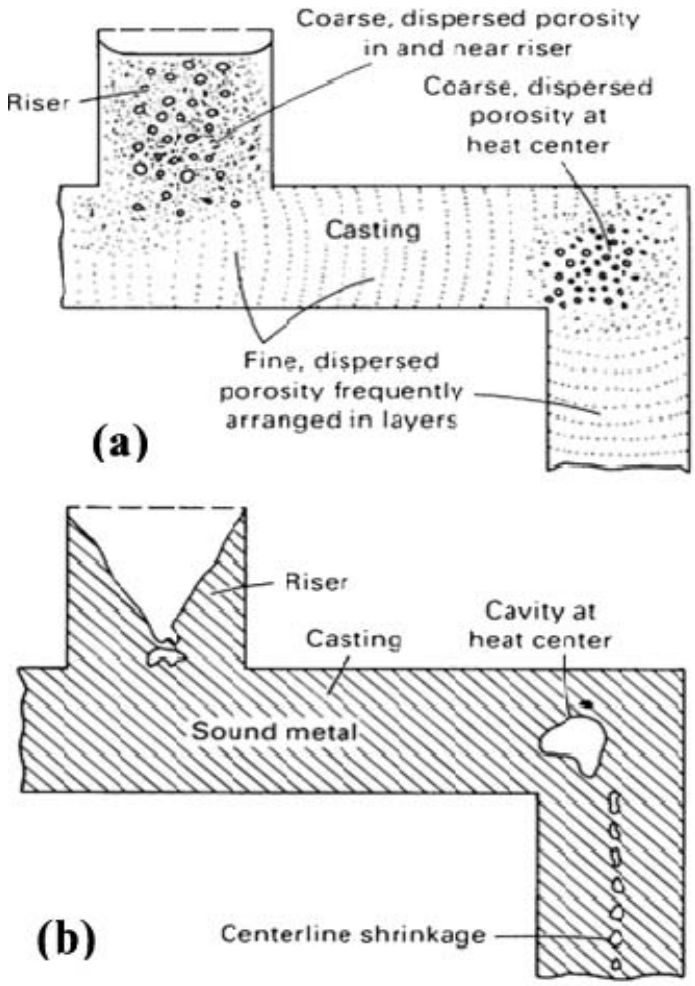

Figure 1.2 Forms of shrinkage in sand cast alloys with a) long, and b) short freezing range [2].

1.3 Feeding mechanisms

The different feeding mechanisms occurring during the solidification of alloys have been categorized by Campbell [5, 6]. The mechanisms, shown in **Figure 1.3**, are:

1. Liquid feeding: This mechanism is the most extensive feeding mechanism because liquid can flow under low pressure gradients. It is crucial only in low freezing range alloys. In wider freezing range alloys, other mechanisms are more important.

2. Mass feeding: In this mechanism, the contraction due to solidification is compensated by a flow of liquid in which there are floating solidified dendrites. This stage of feeding is the start of mushy state solidification. Once the floating dendrites form a coherent network, this feeding mechanism is stopped.

3. Interdendritic feeding: At this stage, the feeding of liquid metal continues but is limited to the interdendritic channels. As dendritic growth continues, the increased complexity of the interdendritic geometry increasingly restricts flow. This mechanism is the intermediate mechanism in mushy zone solidification.

4. Solid feeding: At late stages of solidification, it is possible that sections of the casting become isolated from the liquid. In this case, the solidification of the isolated region is accompanied by the development of high hydrostatic stress in the trapped liquid; sometimes high enough to cause the surrounding solidified shell to deform, sucking it inwards. This inward flow of the solid relieves the internal tension, like the other feeding mechanisms.

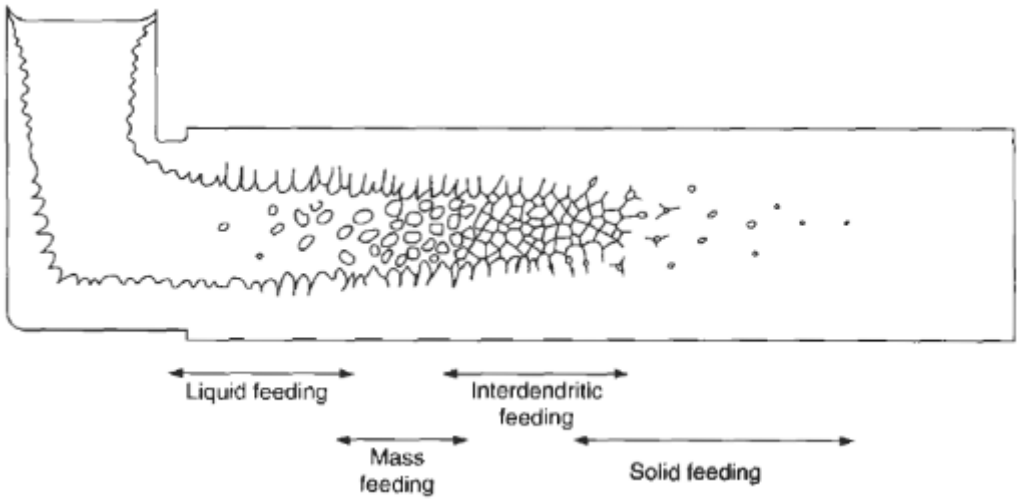

Figure 1.3 Schematic representation of the feeding mechanisms in a solidifying casting [6].

The morphology of solidifying dendrites (columnar or equiaxed) is an important factor affecting interdendritic feeding. These different microstructures affect the resistance to the compensatory flow through affecting the tortuosity of flow channels. In general, this forced flow has been studied for three situations (**Figure 1.4**):

1. Flow in columnar dendrites that is parallel to the axis of dendrites.
2. Flow in columnar dendrites that is normal to the axis of dendrites.
3. Flow in a network of equiaxed dendrites.

The resistance to feeding in these situations increases from 1 to 3 [7]. Also, in each case, as the mushy zone length increases, feeding becomes more difficult.

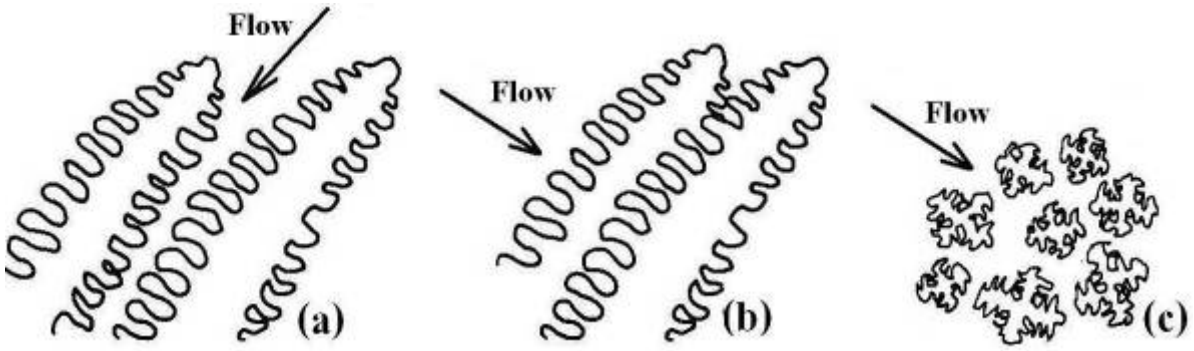

Figure 1.4 Interdendritic feeding in a) columnar dendrites and flow parallel to the axis of dendrites, b) columnar dendrites and flow normal to the axis of dendrites, and c) a network of equiaxed dendrites.

1.4 Permeability

During dendritic solidification of long freezing range alloys, a pressure drop occurs that under the right conditions leads to the nucleation and growth of pores [3, 4]. Various approaches have been adopted to solve for the pressure field within the mushy zone ranging from straightforward analytical expressions for steady state solidification [8] to more realistic transient solutions based on Darcy's Law and the continuity equation [4, 9-15]. For models employing Darcy's Law, the mushy zone is considered as a porous medium. Low velocity flow conditions, e.g. $Re < 1$, exist in the mushy zone during solidification. For this range of Re, the flow of a fluid through a porous medium can be described by Darcy's Law [16]:

$$q = \frac{K}{\mu}\frac{\Delta P}{L} \qquad \textbf{Equation 1-1}$$

where q is the superficial velocity, K is the permeability, μ is the dynamic viscosity, ΔP is the applied pressure difference, and L is the length of the porous medium. Any model describing the flow of interdendritic liquid with the Darcy equation is very sensitive to the permeability since it affects the pressure calculation [17, 18]. In the following section, some of the research related to permeability determination will be reviewed including the quantitative methods used to determine the permeability of mushy zones such as analytical solutions, experimental measurements and numerical simulations.

1.4.1 Analytical determination of the permeability

1.4.1.1 Isotropic permeability

For equiaxed structures, the Carman-Kozeny equation, derived from the solution of the Poiseuille equation, is often used to describe the permeability [19-21]:

$$K = \frac{(1-f_s)^3}{k_C S_v^2 f_s^2}$$ **Equation 1-2**

where f_s is the solid fraction, S_v is the solid/liquid interfacial area per unit volume of solid, and k_C is a constant. There is still ambiguity at the present time whether the Carman-Kozeny or any other analytical relationship is applicable over a wide range of solid fractions and microstructures [22]. One of the issues with this relationship is the value of k_C. It has been shown that k_C is close to ~1 [23] for dendritic and ~5 [24] for granular microstructures. Some researchers [25-27] have also reported that k_C is equal to 5 for both dendritic and globular microstructures. Another issue with employing **Equation 1-2** is to relate S_v to more practical parameters. There are some reports to link the solid/liquid interfacial area per unit volume, S_0 (which equates to $S_v f_s$), to d_2 (d_2 is the secondary dendrite arm spacing - SDAS) in which S_0 has been estimated by $1/ d_2$ [23] and $4/ d_2$ [10]. Additionally, there is another widely used expression in which $k_C S_v^2$ is considered equal to $180/d_2^2$ [4, 9, 14]. However, as discussed by Lee et al. [11], this commonly used equation results in very small permeabilities and leads to unrealistically high pressure drops.

1.4.1.2 Non-Isotropic permeability

For columnar dendritic structures (**Figure 1.4**), permeability is not isotropic, but rather depends on the direction of flow. For anisotropic porous materials, permeability is fully described by a 3×3 tensor with diagonal values corresponding to flow in each direction. Given the symmetry of columnar dendrites, the permeability can be effectively described by two components, a parallel and a normal component. Poirier [28] proposed a permeability relation for the flow normal and parallel to the axis of columnar dendrites for solid fractions

greater than 0.6. Heinrich and Poirier [22] later suggested another relation for complete solidification range. Santos and Melo [7] also derived an analytical relation, based on Poiseuille equation and Darcy's Law. Their derivation was based on the simplified geometry for interdendritic channels and a function of primary and secondary dendrite arm spacing.

1.4.2 Experimental determination of the permeability

To experimentally measure the permeability, an apparatus, called a permeameter, can be constructed which applies a pressure gradient to a mushy zone while measuring the discharge velocity. Different researchers have used various permeameter configurations to measure the permeability of Al alloys, Pb-Sn alloys and organic alloys. In the following section, the operational theory of the basic permeameter apparatus is discussed along with measurements on Pb-Sn alloys [29].

1.4.2.1 Permeameter design and testing

A permeameter cell can be constructed from pipe and fittings formed into a U-shaped system. As shown in **Figure 1.5**, the system consists of an inlet, outlet and connecting pipes to form a flow cell. The flow cell contains a test sample sandwiched between materials with eutectic composition. The permeability test sample and the top portion of eutectic material are cast separately as rods and are machined to fit in the inlet pipe. Additional eutectic material is cast directly into the connecting pipe. The system is assembled and then placed in an oven with a fan to achieve an isothermal environment. A thermocouple is used to monitor the temperature in the inlet pipe. With the aid of this thermocouple and a control system, the temperature of the system is held constant during the experiment within a desired temperature range. By monitoring the applied pressure in the mushy zone (difference in

metal height between the inlet and outlet pipes), along with the discharge velocity (rate of metal height increase in the outlet pipe), the permeability is calculated using Darcy's Law.

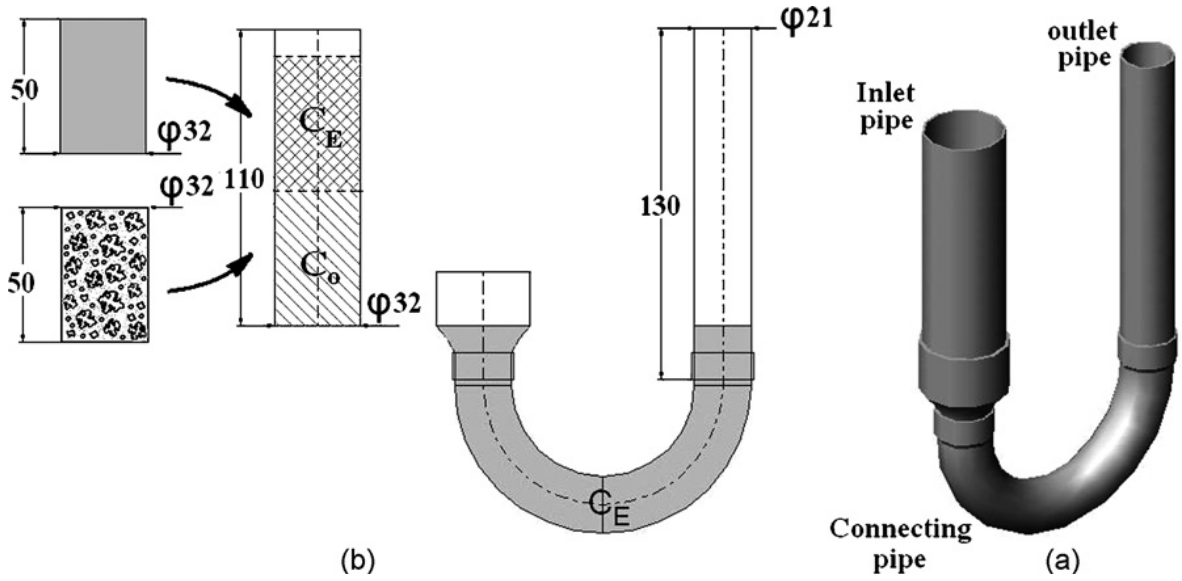

Figure 1.5 Schematic illustration of the experimental setup used for measurement of interdendritic permeability in the mushy zone of Pb–Sn alloys [29].

In this type of permeameter, the height difference between the liquid levels in the inlet and outlet pipes decreases continually and the pressure gradient varies during the test, thus an integrated form of Darcy's Law must be used. Using the analysis of Poirier and Ocansey [30, 31], assuming that K remains constant during the test, the integrated form of Darcy's Law is:

$$-\ln(1-\beta h) = \gamma K t \qquad \textbf{Equation 1-3}$$

with

$$\beta = \frac{\varepsilon}{\alpha} \qquad \varepsilon = 1 + \frac{A_i}{A_o} \qquad \alpha = \frac{A_i}{A_o} H_0 \qquad \gamma = \frac{\varepsilon \rho g}{\mu L}$$

where A_i and A_o are the cross-sectional areas of the inlet and outlet pipes, H_0 is the initial height of the permeability and eutectic samples, h is the instantaneous height of the molten metal in the outlet pipe, and L is the height of permeability sample. The slope of $-\ln(1-\beta h)$ versus γt is the permeability of the test sample. **Figure 1.6a** shows the variation of molten metal height in the outlet chamber versus time for a Pb-25wt%Sn sample [29]. The rate of change of the outlet metal height with time is slow, initially, before increasing rapidly during the middle of the test and finally, decreasing toward the end of the experiment. It is clear from **Figure 1.6b** that, K is not constant during the experiment. At the start of the experiment, the flow rate is slow because the interdendritic zone does not melt instantaneously. Once the material in the interdendritic zone is completely melted, the flow rate remains nearly constant. The flow rate increases slightly due to coarsening but this effect is difficult to observe via these measurements. Near the end of the experiment, the flow rate decreases as the difference between the heights of the molten metal in the inlet and outlet pipes becomes small. Ignoring the effect of coarsening during the test, the flow rate during the middle of the experiment is used to determine the permeability. The intermediate region of this curve, where the slope is relatively constant, is used to calculate the permeability.

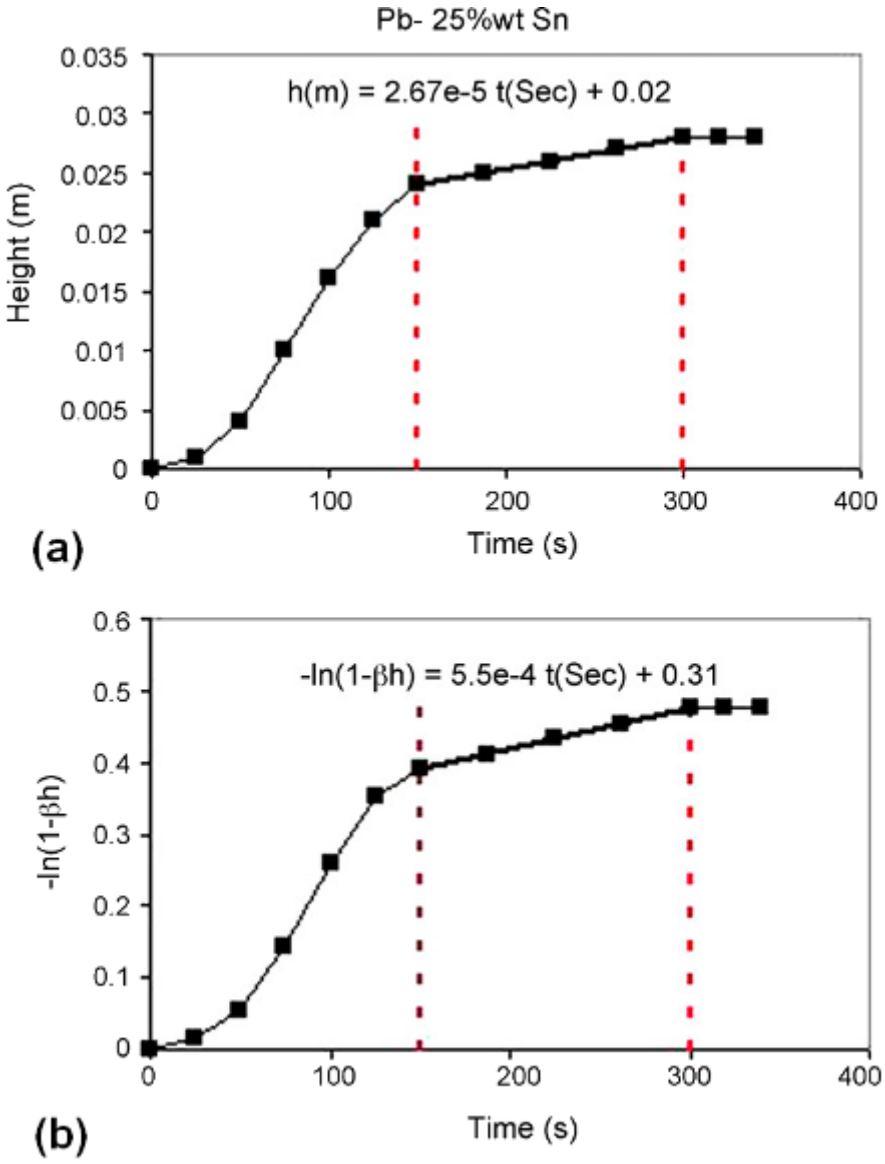

Figure 1.6 Variation of a) molten metal height in outlet pipe, and b) –ln(1-βh) with time for Pb-25wt%Sn at testing temperature of 185^{o}C [29].

The typical approach for comparing the permeability across different microstructures and alloys is to report the dimensionless permeability (KS_v^2). Since the microstructure changes during the permeability test (**Figure 1.7**), some researchers use the average S_v [29-31].

Others use a modified technique to address this problem and calculate the instantaneous permeability [25, 26].

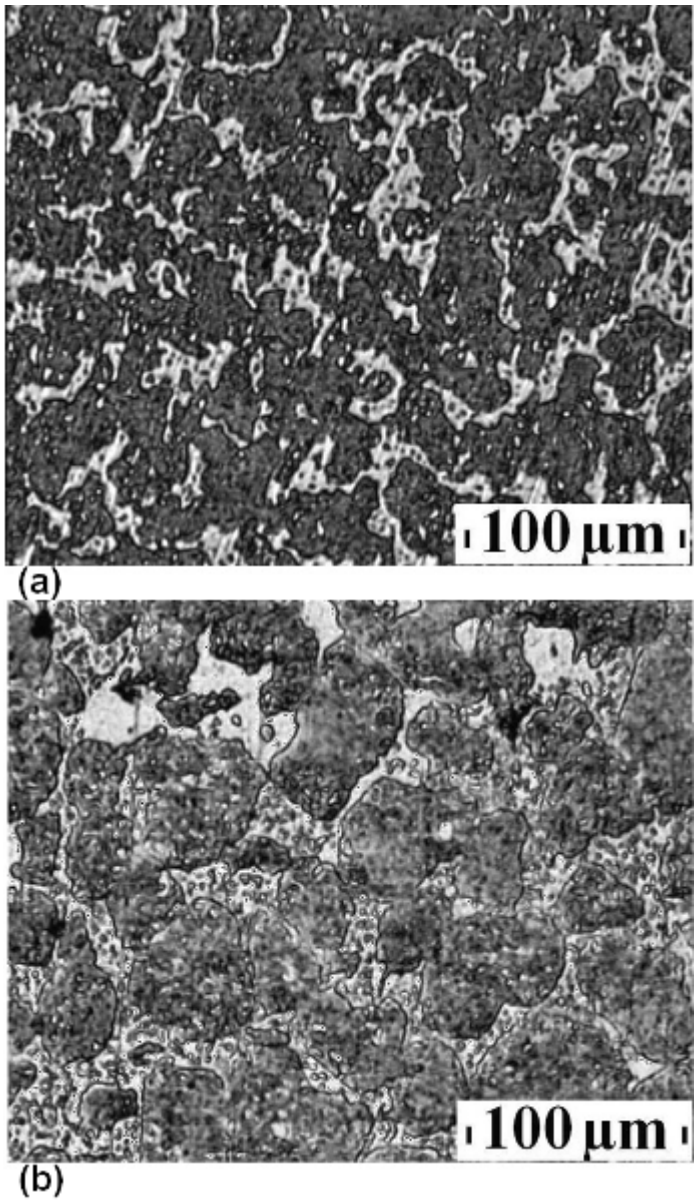

Figure 1.7 Typical microstructure of Pb-25wt%Sn a) before and b) after the permeability test [29].

1.4.2.2 History of experimentally measured permeability

Many experimental studies have been performed on equiaxed dendritic microstructures. Piwonka and Flemings [8] carried out the first measurement of liquid permeability using molten lead in solidifying Al–4.5wt%Cu. Apelian et al. [32] measured the permeability of Al–Si alloys using water as the working fluid. Streat and Weinberg [33] measured the permeability in a Pb–20wt%Sn alloy using a eutectic Pb–Sn alloy as the working fluid. Murakami et al. [34, 35] used borneol–paraffin organic alloy and an aqueous solution as the working fluid to study the permeability in equiaxed analogous structures. In these early investigations, the information reported on microstructural length scales was not suitable for use in describing the variation of permeability in solidification models.

Poirier et al. [30, 31, 36] performed measurements of permeability for Al–Cu and Pb–Sn alloys with equiaxed structures to investigate the influence of dendrite morphology. Duncan et al. [25, 26] examined the permeabilities of some Al-Cu and Al-Si alloys at just above the eutectic temperature. Recognizing that Poirier et al. [30, 31, 36] had determined an average value for permeability over a period of time, they used a modified technique for calculating experimental permeability as a function of time. Nielsen et al. [27] measured the permeability of equiaxed Al–Cu alloys for liquid fractions in the range of 0.09–0.32 to more rigorously examine the match between experimental data and the Carman-Kozeny equation. **Figure 1.8** shows the dimensionless permeability (KS_v^2) plotted versus the solid fraction measured by these different researchers. Despite the scatter in the reported values, a k_C value of 5 is used to reproduce the results when Carman-Kozeny relation is employed.

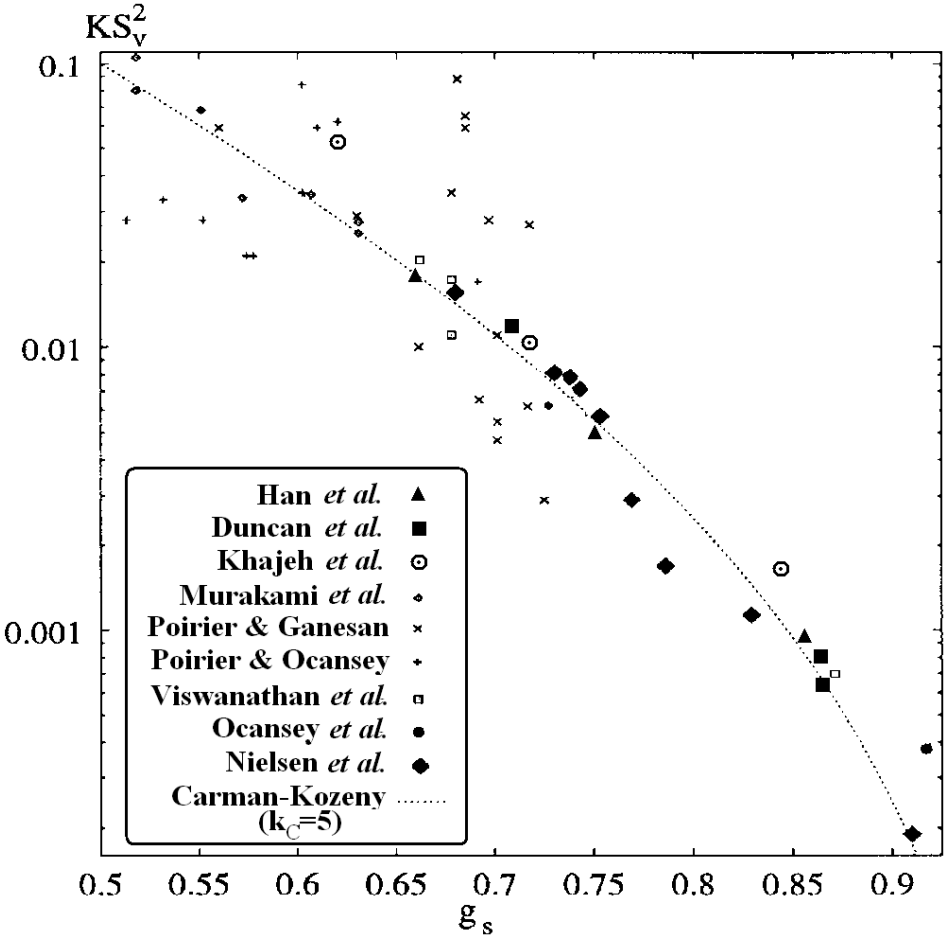

Figure 1.8 Plot of the dimensionless permeability, KS_v^2, as a function of volume fraction of solid, g_s. Different experimental results have been compared with the Carman-Kozeny expression with $k_C=5$.

1.4.2.3 Experimental difficulties and alternative methods

The most significant problems affecting experimental measurements of permeability with liquid metal include preparing test samples that exhibit uniformity of structure, maintaining a uniform temperature throughout the sample for the duration of the test, formation of oxide layers on samples and flux surfaces (interface between permeability and eutectic samples) which inhibits flow, formation of preferred-flow channels, and ensuring that the solid

dendritic grains remain interconnected and fixed during the test. An additional important source of error is the natural tendency of the microstructure to change during the test period due to coarsening and back diffusion in the solid. These experimental difficulties, as they applied to permeability measurements in Al alloys, were reviewed by Nielsen et al. [37].

Despite these errors caused by issues inherent with the experimental technique, the use of permeameters is still an effective means to measure permeability during primary dendritic solidification. For eutectic solidification, this measurement methodology cannot be employed because eutectic solidification is an isothermal transformation, making it impossible to maintain the instantaneous microstructure part way through the eutectic transformation. Considering that many commercially relevant casting alloys have significant fractions of eutectic phase in their microstructure, this technique can not act as an effective means of characterizing the permeability for all casting alloys.

To address the limitations of permeameters, some researchers have opted to use physical models to measure the permeability. Despois and Mortensen [38] measured the permeability of open-pore microcellular materials (open foam) by passing glycerin mixed with water through aluminum open-pore foams produced using a replication process. From this work, they proposed a permeability equation for open-pore materials. James et al. [39] passed oil through a large-scale physical model of repeating slotted plates to measure permeability. The results of both studies [38, 39] suggest that experiments on physical models are a suitable alternative to permeameter measurements. However, there has been no research reported on the use of replicas of dendritic geometry to measure permeability.

1.4.3 Numerical determination of permeability

Due to the complexity of the problem, relatively few studies have been carried out to estimate the permeability of interdendritic channels numerically. In numerical methods, in general, a flow cell consisting of one dendrite (regular array) or some dendrites (random array) may be chosen to represent the bulk material. By applying a low Reynolds number flow at one side and solving the continuity and momentum equations, the pressure drop is calculated which is used to compute the permeability.

There is some doubt whether using one dendrite or a small flow cell can represent the characteristics of the bulk material. Papathanasiou and Lee [40] investigated the effect of particle distribution on the permeability of unidirectional arrays of cylindrical fibers. They showed that for conditions with low liquid fractions, random perturbations in fiber size and location result in considerable variations in the permeability, as compared to the perfect square array of mono-sized fibers (**Figure 1.9**). This result confirms the limitation of using a small flow cell or regular array of dendrites.

The main factor limiting the application of numerical determination techniques is the lack of a computational domain that accurately represents the geometric complexity of the mushy zone. Numerical methods applied to determine the permeability of solidifying structures have used either simulated structures [23, 24, 29] or images of actual dendrites [41-44].

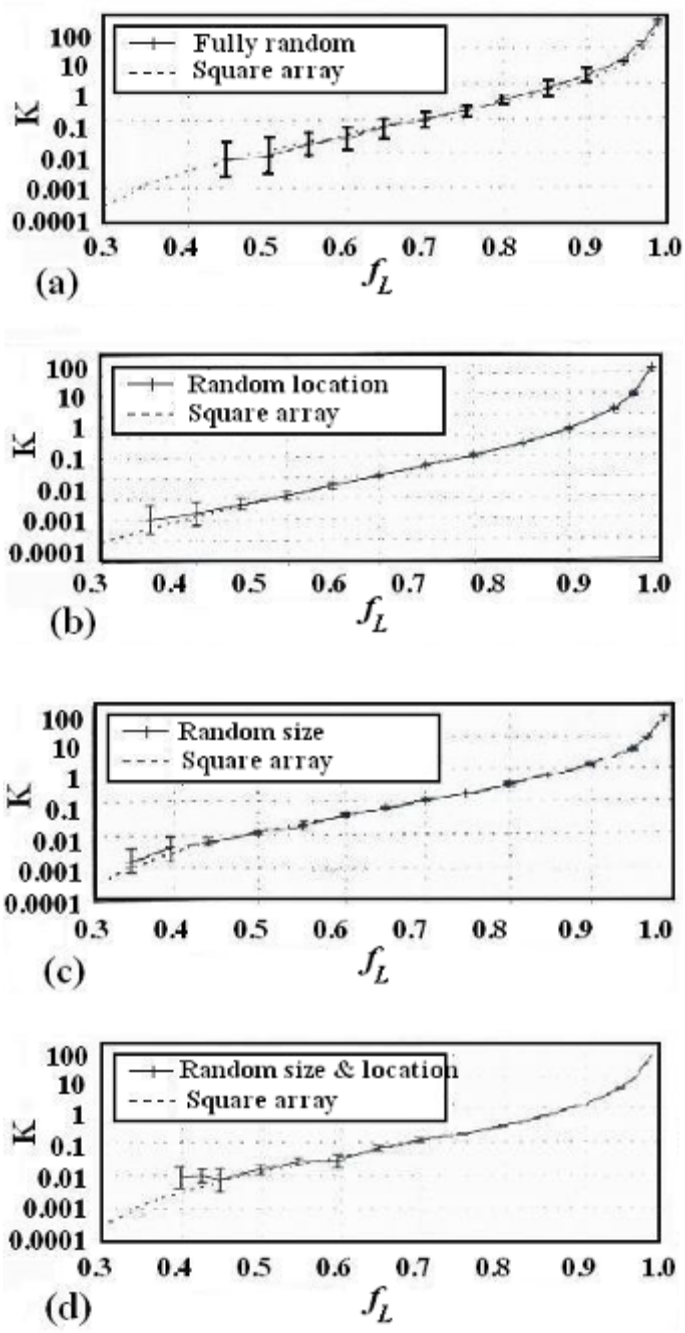

Figure 1.9 Effect of particle distribution on normalized permeability of cylindrical fiber arrays. a) Fully random, b) square packing with random location, c) square packing with random size, and d) square packing with random size and location [40].

1.4.3.1 Permeability determination using simplified microstructure

Simplified dendrite geometry can be described by defining an algebraic geometry or simulating the evolution of dendrite. Khajeh et al. [29] developed an algebraic function representing an equiaxed dendrite. A new geometric parameter, *Pe*, was defined to evaluate the deviation form globular shape. As shown in **Figure 1.10**, *Pe* (i.e. P_d/R_d) is the extent of perturbation while maintaining a constant solid fraction. The model defines the dendrite shape as a rotated polar function around the *x*, *y* and *z* axes (FCC alloys). By solving the continuity and momentum equations on the domain shown in **Figure 1.11**, the pressure drop across the domain is obtained and is used to determine the permeability (**Figure 1.12**).

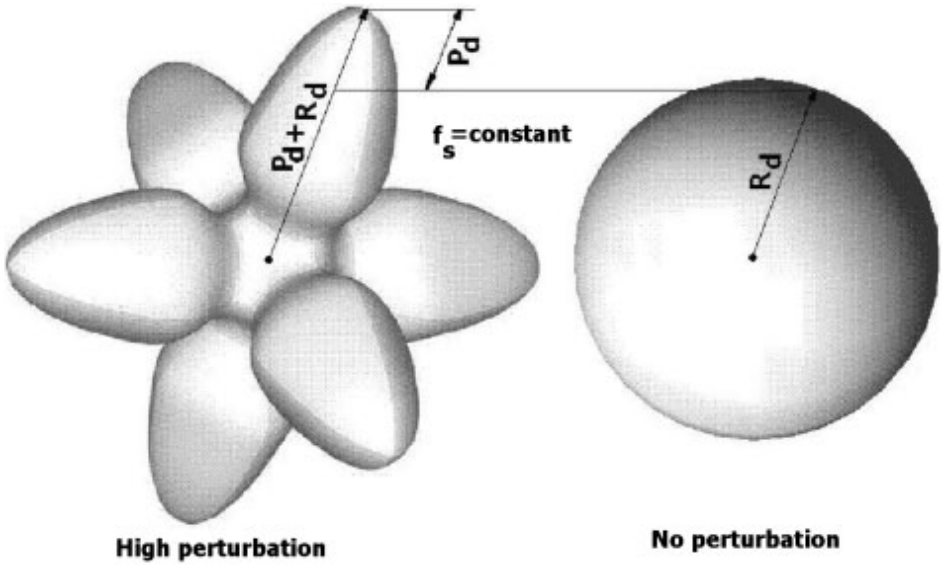

Figure 1.10 3D illustration of perturbation in FCC alloys with preferred growth direction of <100>. P_d is the extent of dendrite distention versus a sphere with the same volume and the radius of R_d [29].

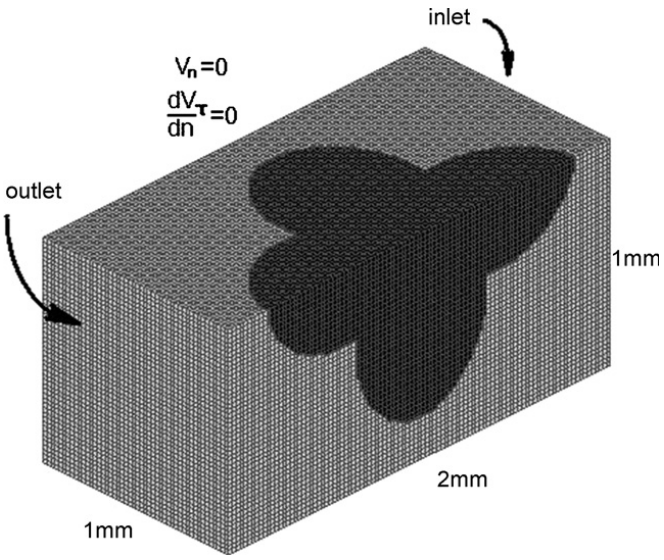

Figure 1.11 The flow cell, used to compute the permeability [29].

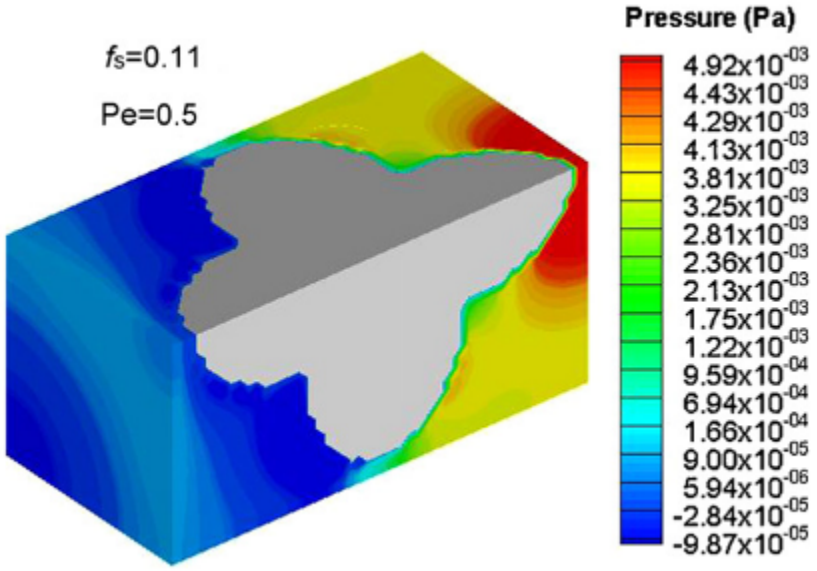

Figure 1.12 Calculated pressure contours for a typical microstructure [29].

With the pressure profile across the domain, one can determine the permeability using Darcy's Law. Using this approach, Khajeh et al. [29] numerically determined values of permeability to assess the dependency of permeability on f_s and Pe, shown in **Figure 1.13**. Simulation results are in good agreement with the Carman-Kozeny expression of permeability with a k_C value of 3.

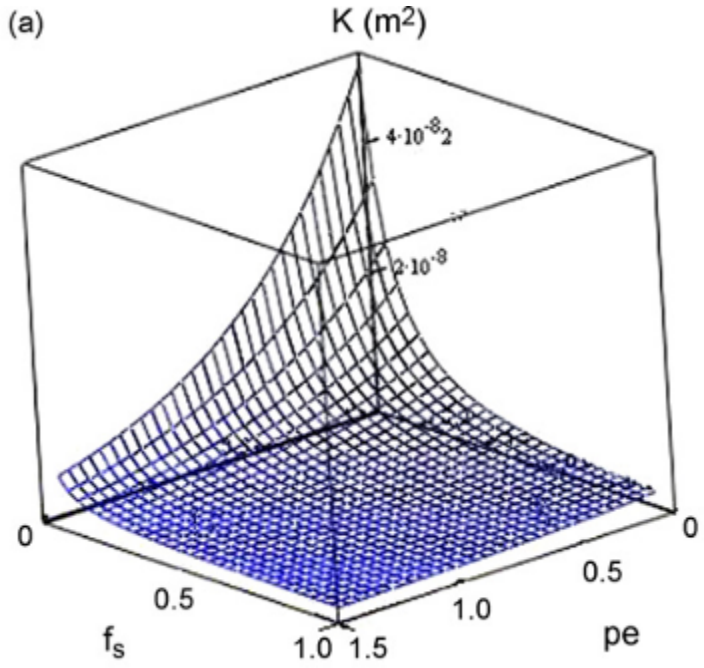

Figure 1.13 Estimated curve for K(f_s,*Pe*). The coefficient of correlation (R^2) for this estimation was 0.951.

Another approach to numerically determine permeability is to use simulated dendrites to define the computational domain for a permeability calculation. Brown et al. [23] predicted the variation in permeability of an evolving equiaxed dendrite for an Al-3wt%Cu-3wt%Si

alloy. They employed a Cellular Automaton Finite Difference (CAFD) model to predict the evolution of a single dendrite (cubic distribution of dendrites) in 3D (**Figure 1.14**) and solved the Navier-Stokes equation on a uniformly meshed domain to determine the permeability. In a follow-on investigation, Spittle and Brown [18] extended their model to the binary Al–Si, Al–Cu and Al–Mg systems. The permeability calculated by their new approach was more accurate because the microstructural predictions were based on randomly located grains growing in the domain. The length scale for normalizing the results was the computational S_v calculated from the meshed (simulated) domain. They concluded that a k_C value of 1 is appropriate for use in the Carman-Kozeny expression (**Figure 1.15**).

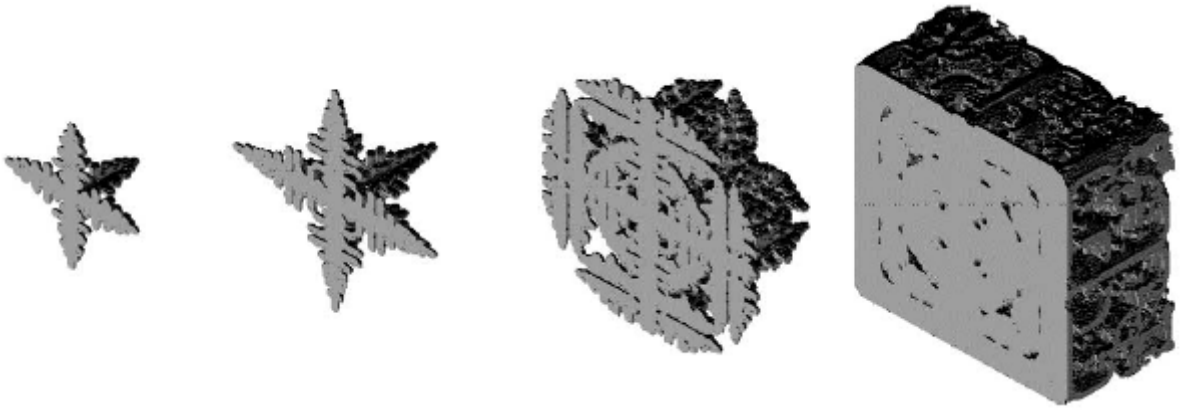

Figure 1.14 Simulated evolution of an equiaxed dendrite for an Al-3%Cu-3%Si alloy at effective solid fractions of 0.001, 0.01, 0.06 and 0.55.

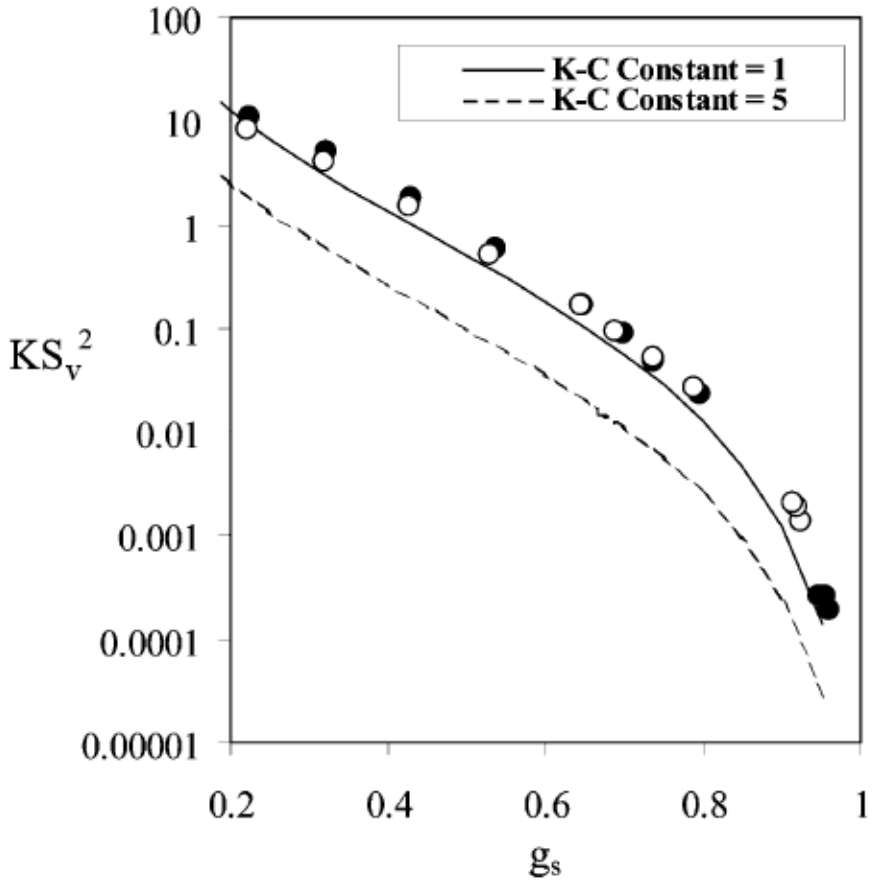

Figure 1.15 Determined values of KS_v^2 versus solid fraction compared with values expected from the Carman-Kozeny expression.

1.4.3.2 Permeability determination using images of real microstructure

Another method for constructing the computational domain for a permeability calculation is to use images of real microstructure. Over the past two decades, researchers have used different techniques to develop suitable geometry from 2D and 3D images of microstructure. Ganesan et al. [42] used this approach to compute the permeability for flow parallel to columnar dendrite arms. They quenched different alloys at different temperatures from the mushy state. By connecting the centers of adjacent dendrites on 2D images obtained from optical microscopy (**Figure 1.16**), they developed a flow cell to use as a computational

domain for fluid flow analysis and permeability determination. They presented their results as dimensionless permeability (Kd_1^2) versus $\log(f_l/f_s)$ with:

$$d_1 = \left(\frac{A}{B}\right)^{\frac{1}{2}} \quad , \quad f_l = \frac{A_l}{A} \qquad \textbf{Equation 1-4}$$

where A is the area of flow cell, A_l is the area of liquid phase, and B is the number of dendrites in a flow cell (for triangular flow cell, B=0.5, and for rectangular cell, B=1).

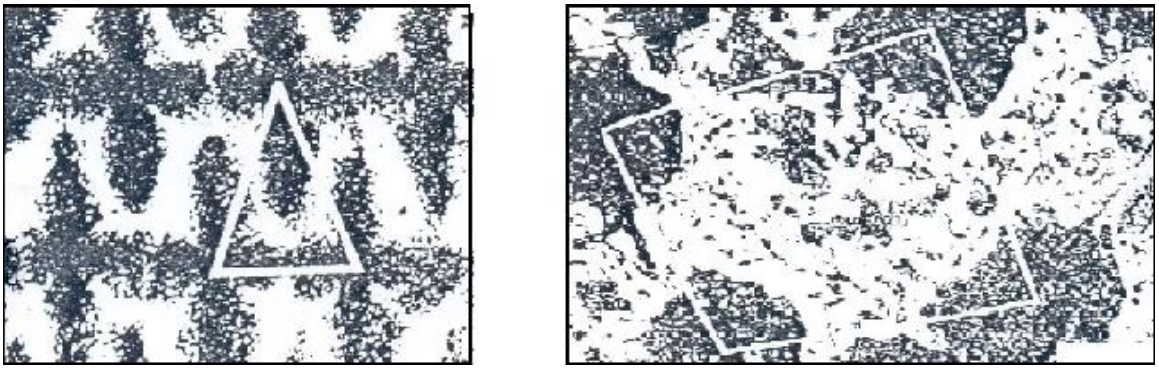

Figure 1.16 Cross-section of a flow cell for Pb-Sn alloy (right) and steel (left). The direction of flow is normal to the image.

The results of this technique are presented in **Figure 1.17** (the curve with a=0). Since these results were based on a straight dendrite (no perturbation along the axis of dendrite), the calculated permeabilities were much higher than the experimental (empirical) results. To solve this problem, they considered a sinusoidal perturbation along the axis of the dendrite. By increasing the amplitude of the perturbation, they reached an acceptable match between simulation and experimental results. They used this amplitude to extrapolate the dimensionless permeability to the ranges of solid fraction in which no experimental data were available.

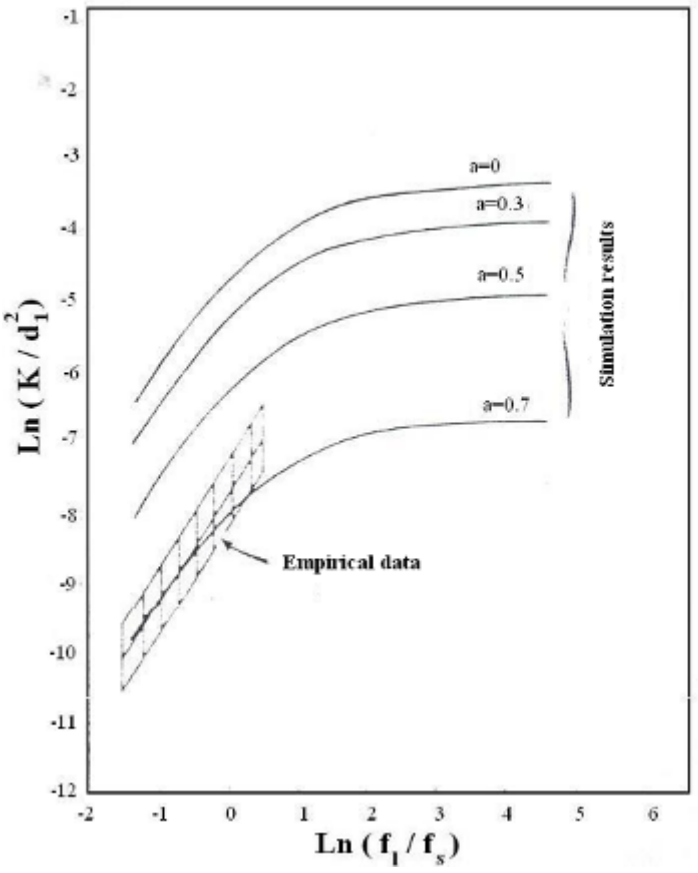

Figure 1.17 Dimensionless permeability for flow parallel to the axis of dendrites assuming sinusoidal perturbation along the axis of the dendrite (*a* is the amplitude).

Bhat et al. [41] used the same approach to calculate the permeability for flow normal to the axis of columnar dendrites. The geometry employed in this study consisted of more dendrites. Employing an unstructured mesh of the liquid phase, they solved the momentum equation using a FE method. An example of the calculated velocity vectors is presented in **Figure 1.18**. The permeability results, presented in the form of dimensionless permeability, KS_v^2 (S_v was measured using 2D metallography, i.e. the perimeter of solid/liquid interface to the area of solid phase), are given in **Figure 1.19**. These results were in good agreement with the available experimental data.

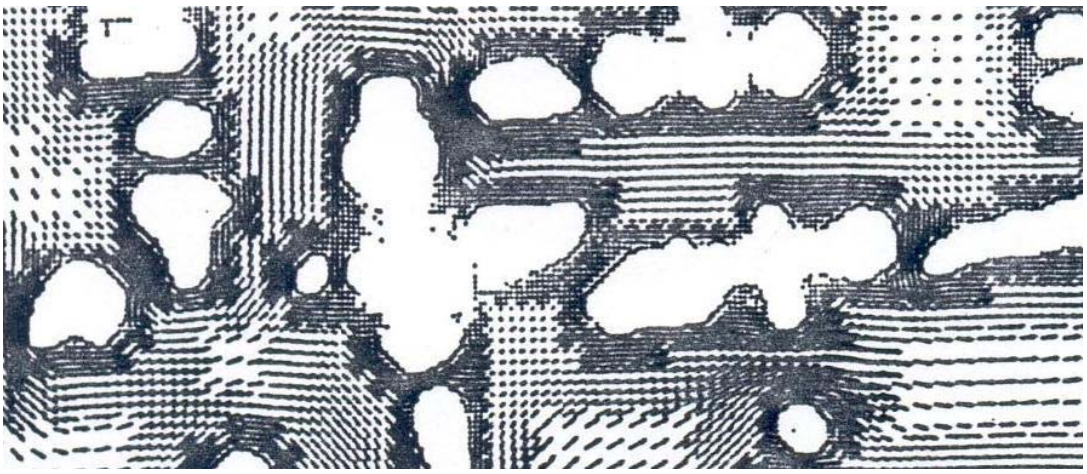

Figure 1.18 Velocity vectors resulted from FE simulation of fluid flow through dendritic structure.

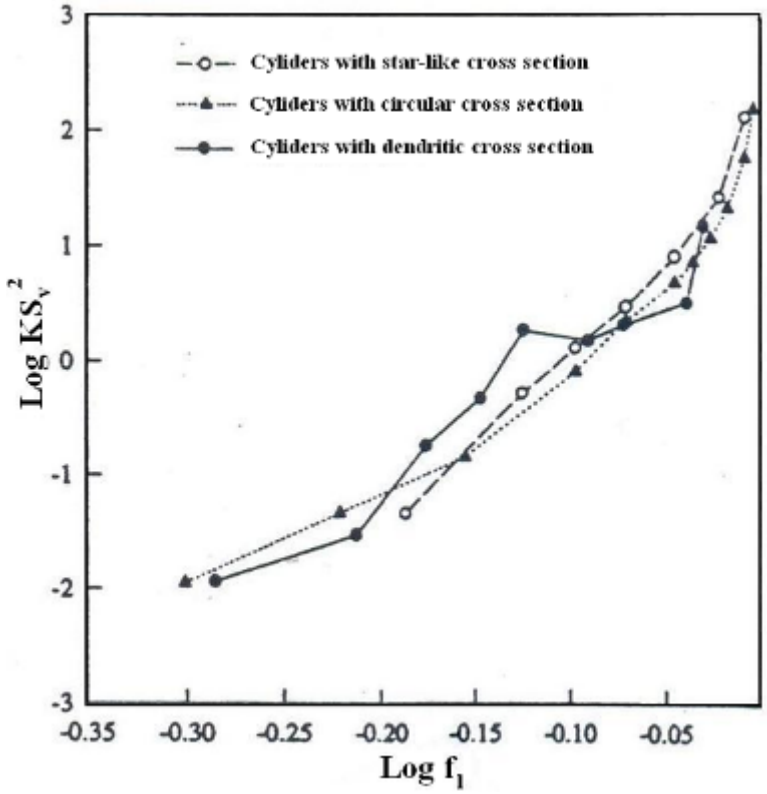

Figure 1.19 Dimensionless permeability for flow normal to the axis of dendrites. Results have been compared with two typical geometries.

Bernard et al. [43] computed the near-eutectic permeability of real microstructures in 3D. Samples of binary Al-Cu alloys were quenched from the mushy state and then characterized in 3D using X-ray Micro Tomography (XMT). The tomographs were binarised in order to separate the Al dendrite skeleton from the quenched eutectic phase, i.e. the liquid phase above the eutectic temperature. Subsequently, the complete permeability tensor was calculated for each sample by solving the Stokes equation in the 3D domain representing the interdendritic liquid. They employed a uniform mesh to construct the computational domain. However, instead of computing the specific surface area from the meshed geometry (as in Brown et al. [23]), they employed a Marching-Cube method to measure the area. The predicted permeabilities with this technique are closer to the Carman-Kozeny expression with a k_C of 5.

Madison et al. [44] computed the permeability of the dendritic structure obtained using serial-sectioning of a directionally solidified nickel-base super alloy. They employed an unstructured mesh to generate a computational domain and obtained the pressure and velocity fields by solving the momentum and continuity equations.

1.4.3.3 Limitations of numerical determination of permeability

Permeability is a geometric parameter which depends on the tortuosity of the active flow channels. Therefore accurate description of the geometry representing the interdendritic channels is crucial in any numerical model. In 2D representations of interdendritic channels or even simplified 3D geometries, the complexity of the computational domain is reduced compared to the real microstructure being represented. Therefore, the calculated permeability does not accurately represent the permeability. Techniques employing 3D characterization of interdendritic channels have been used in attempt to solve this problem. However, even with

3D characterization, it is necessary to generate a computational domain that can represent the real complexity of the flow channels.

1.4.4 Summary of available research on permeability determination

Not withstanding the challenges that exist in accurately characterizing the permeability for different microstructures, a comprehensive equation capable of accurately predicting the permeability of evolving microstructures is necessary for use in macroscale solidification models. For equiaxed structures, which are of relevance to this research, the Carman-Kozeny equation (refer to **Equation 1-2**) is often used to describe the permeability. However, uncertainty continues to exist as to whether the Carman-Kozeny is applicable over the complete solidification range and for the wide variation in microstructure observed during solidification. For example, many commercially relevant cast aluminum alloys have significant fractions of eutectic phase in their microstructures. During the growth of the eutectic grains, the geometry of liquid channels undergoes a transition from dendritic to globular.

As discussed, using a conventional permeameter for permeability determination can lead to errors caused by issues inherent with the experimental technique. However, it is still an effective means of measuring the permeability during the solidification of primary phase. For eutectic solidification, this measurement methodology cannot be employed because eutectic solidification is an isothermal transformation, making it impossible to maintain the instantaneous microstructure part way through the eutectic transformation. Numerical calculation of permeability, on the other hand, can resolve these limitations. However, careful attention must be paid to accurately formulating the analysis when numerically determining permeability. While the precision of most CFD commercial packages have been

tested through comparisons with analytical solutions to standard problems, the application of these packages to real world flow problems lacks extensive validation (i.e. to address whether the model itself is a good representation of the physics of the problem). Moreover, since the permeability is a geometric characteristic of a microstructure, which depends on flow channel widths and tortuosity, an accurate characterization of solidifying microstructure is essential in any method used to characterize the permeability.

1.5 Microstructure characterization

In the early research on permeability determination, the microstructure was characterized by 2D metallographic analysis. With this approach, it was not possible to accurately characterize the complex geometry of flow channels. Moreover, by using 2D metallography, it is not possible to distinguish between active flow channels that participate in the flow and the isolated liquid zones that act like solid. Accurate determination of permeability requires 3D characterization of solidifying microstructure either via experimental or numerical techniques.

1.5.1 Experimental characterization

1.5.1.1 Serial sectioning

Serial sectioning provides 3D microstructure characterization by combining conventional metallography techniques with computer-aided reconstruction [45]. The technique has been used in many fields including paleontology [46], biology [47, 48], and materials science [49-54]. In this technique, the representative sample is sequentially polished and the material removal rate is measured by measuring the thickness change. After each polishing sequence, an image is acquired and later used for 3D reconstruction of the microstructure [55].

Automated systems with fully integrated robotic cells that generate two-dimensional data for three-dimensional reconstruction may be used for accurate and fast serial sectioning. The main features of such systems are their convenience, safety and vibration-free images [56]. This technique was used by Madison et al. [44] for characterizing the permeability of directionally solidified Nickel-base superalloy.

1.5.1.2 X-ray microtomography

X-ray microtomography is a non-destructive characterization technique that provides 3D information of a sample's microstructure and has become a very popular tool in materials science [50, 57-62].

The basis of X-ray tomography is acquisition of a sequence of X-ray images by directing an X-ray beam at a sample and recording the transmitted intensity on a detector. According to the Beer–Lambert Law, the ratio of the number of transmitted to incident photons is related to the integral of the absorption coefficient of the material along the path that the photons follow through the sample. The absorption coefficient is linked to the density, the atomic number, and the beam energy (when the beam is monochromatic) by using an empirical Law. The resulting image is a projection of a volume in a 2D plane. In order to obtain a 3D image, a large number of radiographs are performed while carefully rotating the sample between 0 and 180°. A back-projection algorithm is then used to reconstruct the volume of the sample from these radiographs [57].

Generally, there are different approaches to perform X-ray tomography: pencil beam with point detector, fan beam with 1D detector, parallel beam with 2D detector, and cone beam with 2D detector (shown in **Figure 1.20**) [63].

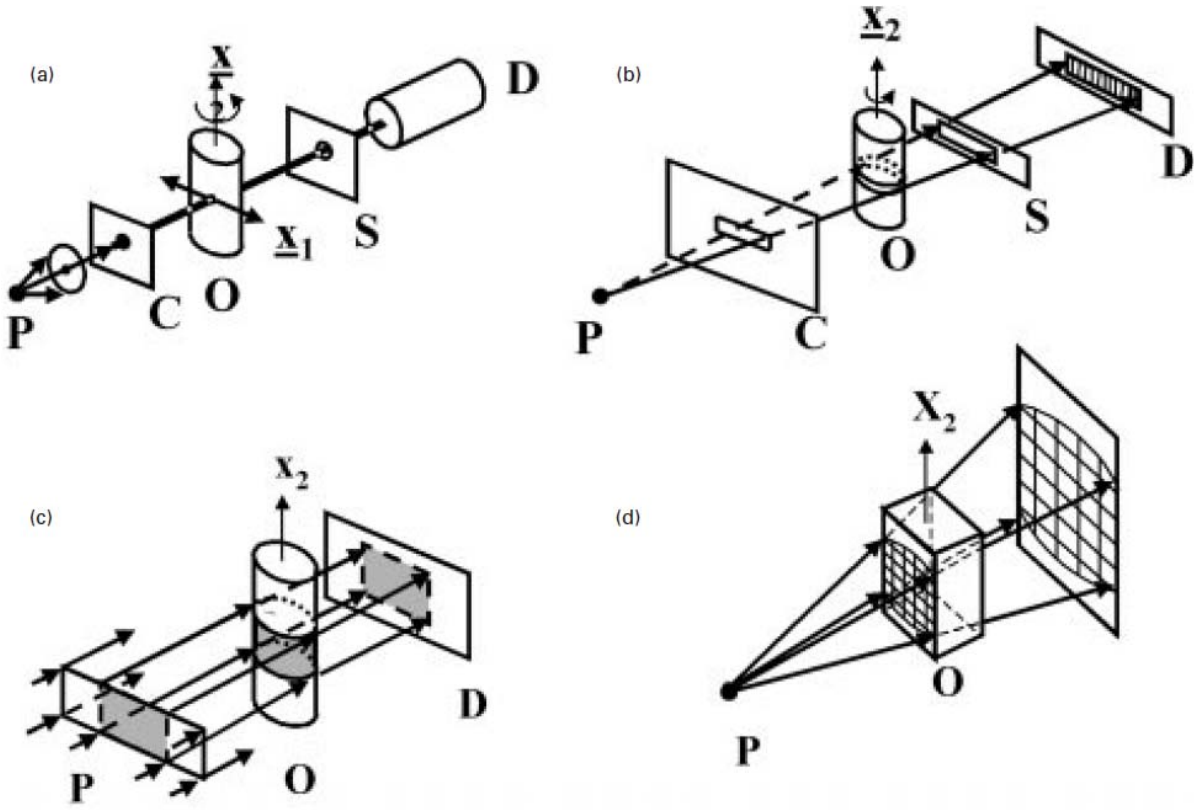

Figure 1.20 Illustration of four experimental approaches to X-ray microtomography data collection: a) pencil, b) fan, c) parallel, and d) cone beam methods. 'P' is X-ray source, 'C' is collimator, 'O' is the object being imaged, 'x2' is the axis about which sample is rotated to produce different views required for reconstruction, 'S' is slit, and 'D' is the detector.

Bernard et al. [43] employed X-ray tomography to generate a computational domain for computing the near-eutectic permeability of Al-Cu alloys. In their technique, samples were quenched during solidification to separate the pre-quench and post-quench phases. Due to the inability to carefully control the quenching process and the subsequent impact on characterizing the solidifying microstructure, an in-situ characterization technique is more appropriate for accurately characterizing the microstructure. Recently, Limodin et al. [64]

investigated the dendritic solidification of an Al-10wt%Cu alloy using an in-situ and real-time microtomography for a low cooling rate of 3°C/min. This technique provides an accurate characterization of a solidifying microstructure. However, the main challenge that must be addressed is that a low solidification rate is necessary to ensure that the microstructure does not evolve too much during image acquisition [64].

1.5.2 Numerical simulation

With the development of advanced numerical techniques and the improved understanding of the mechanisms governing microstructure development, there has been substantial progress in the field of microstructural modeling. For instance, the Phase Field method has been widely applied to improve our knowledge in the area of solidification [65]. However, one of the major challenges that must be addressed when employing phase field models is running realistic or relevant problems within the bounds of current computational resources. Stochastic models, on the other hand, are more computationally efficient. Brown and Spittle [66, 67] were one of the first to develop a stochastic model, based on the Monte Carlo (MC) technique, to predict the grain structure in a casting. Since this initial application, MC models have been shown to accurately predict the grain structure observed in real castings. However, models based solely on the MC technique do not properly account for the physical phenomena observed during the growth of dendritic or eutectic phases [68, 69]. To address this, physically-based modeling techniques such as the Cellular Automaton (CA) technique have been developed [69].

The CA technique was first developed by Hesselbarth and Gobel [70] to simulate recrystallization. In this method, the computational domain is divided into cells with associated state data (phase, orientation, etc.) and calculated fields (temperature,

composition, etc.). A cell changes state based on transition rules, which can be probabilistic or deterministic and often incorporate neighboring cell states [69]. A number of researchers have used the CA technique to describe solidification processes [68, 71-74]. Rappaz and Gandin [71] and Gandin et al. [72] developed a CA model to predict the grain structure during the solidification of an Al-Si alloy and a Ni-based superalloy, respectively. Rappaz et al. [68] coupled a CA growth model with a probabilistic nucleation relationship and a Finite Element (FE) heat transfer model to create the CAFE modeling technique. Charbon and Rappaz [73] adapted the CA technique into a 3D probabilistic model for equiaxed eutectic solidification. This model employed a deterministic nucleation relation at a number of random locations and a deterministic CA model to predict growth. Charbon and LeSar [74] proposed a 2D stochastic model to simulate equiaxed eutectic solidification that coupled macroscopic heat diffusion calculations with a microscopic quantification of nucleation and growth using deterministic relations. Careful attention must be paid to the relationships describing eutectic nucleation and growth in deterministic models. Most microscopic models of solidification assume that bulk heterogeneous nucleation takes place on nucleation sites that become active as the undercooling increases.

For modeling the eutectic solidification, the two most widely used functions to describe heterogeneous nucleation are: i) a Gaussian distribution [73] and ii) a power Law distribution, first introduced by Oldfield [75]. The constants in each function depend on the composition and cleanliness of the alloy and therefore must be determined experimentally for each system. The growth velocity of eutectic transformations is controlled by the interlaminar diffusion of solute elements in the liquid ahead of the solidification front and the surface energy associated with the tip curvature of laminas [76]. Jackson and Hunt [77]

derived a relationship for the growth velocity of regular eutectics which is proportional to the square of the undercooling ($v \propto \Delta T^2$). For irregular eutectic growth, Jones and Kurz [78] modified this model but maintained the proportionality to ΔT^2. Although the Jackson – Hunt growth equation is based on the assumption of steady-state growth, it has been successfully applied in deterministic models with transient growth conditions [73, 74, 79, 80].

For some alloy systems like grey cast iron, the Jackson-Hunt growth model or its modified version have been shown to accurately describe eutectic growth [73]. However, in the Al-Cu alloy system, the type of Al_2Cu-Al(Cu) eutectic formed depends on the thermal conditions under which the eutectic solidification occurs [81, 82]. Additionally, in some hypoeutectic alloys, when eutectic grains form in the presence of a widely distributed dendritic network of primary α phase, the corresponding α phase in the eutectic may form preferentially on the existing primary dendrites leading to the formation of divorced eutectic [83]. The variety of growth behaviors that eutectic phases exhibit highlights the need for improved understanding of their growth patterns. Developing a quantitative understanding of these types of eutectic transformations requires either simulations of the growth patterns at the micro-scale that are capable of resolving both phases within eutectic or developing more comprehensive deterministic relationships for the growth.

1.6 Scope and objective of thesis

The focus of this study is to characterize the permeability of hypoeutectic aluminum alloys over the complete solidification range (from equiaxed dendritic to equiaxed eutectic/dendritic). As discussed, using a conventional permeameter for permeability determination is prone to error for equiaxed dendritic microstructures and is not suitable for characterizing the permeability of eutectic/dendritic mixutres. Numerical techniques, on the

other hand, can resolve some of the issues associated with permeameter measurements but require extensive validation and difficult to acquire geometric information. Considerable ambiguity exists regarding the application of the available analytical and/or empirical relations over the complete solidification range and for a wide variation in microstructure. To address these issues, the objectives of the present work are defined as:

i) Developing an expression for the permeability of hypoeutectic aluminum alloys that applies to the complete solidification range (from equiaxed dendritic to equiaxed eutectic/dendritic);

ii) Developing a new experimental technique for measuring permeability that does not suffer from errors caused by issues inherent with conventional permeameter measurements;

iii) Developing a numerical technique to determine the permeability for the range of microstructures expected during equiaxed solidification of hypoeutectic aluminum alloys;

iv) Characterizing the evolution of microstructure during equiaxed solidification of hypoeutectic aluminum alloys for permeability characterization.

The thesis is organized as follows: In Chapter 2, the microstructure formed during equiaxed dendritic and eutectic/dendritic solidification will be analyzed both experimentally and numerically. The characterized microstructures will be used for permeability determination. In Chapter 3, a new experimental technique along with a numerical modeling technique will be presented for permeability determination. In Chapter 4, the permeability of Al-4.5%wtCu alloy and the near eutectic permeability of Al-Cu alloys during equiaxed dendritic solidification will be characterized. The analysis presented in this chapter will be used to develop a mathematical expression for permeability determination from practical

parameters available in solidification models. Using the obtained mathematical expression for the permeability of equiaxed dendritic structures, a new theoretical expression for predicting the permeability for the complete solidification range of hypoeutectic aluminum alloys will be presented in Chapter 5. The derived expression will be then verified and validated through physical and numerical modeling.

The results of this work provide a new knowledge on the evolution of permeability during solidification of hypoeutectic aluminum alloys.

2 Microstructure Characterization[1]

Since permeability is a geometric parameter that depends on the width and tortuosity of the active flow channels, accurate characterization of the evolving microstructure during solidification is essential for precise permeability calculations. As previously discussed, 2D characterization of solidifying microstructure does not adequately represent the geometry of the active flow channels. Instead, accurate determination of permeability requires 3D characterization of the solidifying microstructure either via experimental or numerical techniques. In this project, the evolution of equiaxed microstructures throughout the complete solidification range (from equiaxed dendritic to equiaxed eutectic/dendritic) of hypoeutectic aluminum alloys has been characterized and used for subsequent permeability determination. Equiaxed dendritic solidification has been characterized experimentally with the aid X-ray microtomography (XMT). To characterize the solidification of equiaxed eutectic grains, a combined experimental and numerical technique has been developed. In the following sections, experimental and numerical methodologies and the results of microstructure characterization are presented.

[1] A version of this chapter has been published in:

- Khajeh E, Maijer DM, "Physical and numerical characterization of the near-eutectic permeability of Al-Cu alloys", Acta Materialia, (2010) 58, pp. 6334-6344.
- Khajeh E, Maijer DM, "Numerical determination of permeability of Al-Cu alloys using 3D geometry from X-ray microtomography", Mat Sci Technol, (2010) 26, pp. 1469-1476.
- Khajeh E, Maijer DM, "Inverse analysis of eutectic nucleation and growth kinetics in hypoeutectic Al-Cu alloys", Metall Mater Trans A, (2011) 42, pp.158-169.

2.1 Experimental characterization of dendritic solidification

To provide a microstructure for characterizing the evolution of permeability during equiaxed dendritic solidification, the near-eutectic microstructure of some Al-Cu alloys and the evolution of microstructure during solidification of Al-4.5wt%Cu are characterized.

2.1.1 Near-eutectic microstructure of Al-Cu alloys

A technique was developed to produce directionally solidified castings of Al-Cu alloys for this investigation. Al-Cu binary alloys were selected because the difference in X-ray attenuation between Al and Cu facilitates the separation of the primary Al and eutectic structures following XMT. The near-eutectic permeability is then determined using the interdendritic geometry which represents the liquid domain prior to eutectic solidification.

2.1.1.1 Sample preparation

A series of experimental test castings with different eutectic volume fractions (0.15–0.7) were produced from Al with 10, 12, 15, 19 and 25 wt% Cu. The melts were prepared by melting different ratios of commercially pure Al and Al–50 wt% Cu master alloy. Prior to pouring, the melts were degassed for 10 min and skimmed to remove any dross that may have accumulated. The castings were poured with a melt temperature of 700 °C and directionally solidified against a water-cooled copper chill at the bottom of a tapered cylindrical mold made from a fireclay crucible, shown in **Figure 2.1**. From each test, a cylindrical sample, 3.0 mm in diameter and 60 mm long, was removed from the centerline of the casting for subsequent XMT analysis.

2.1.1.2 X-ray microtomography

XMT analysis was used to characterize the microstructure of each cast sample. The applications and benefits of XMT characterization in materials science have been discussed previously by Salvo et al. [57]. Bernard et al. [43] provided detailed instructions and procedures for analyzing Al–Cu samples to extract the 3-D geometry of interdendritic structures and thus these details are omitted here for brevity. The samples were scanned on the TOMCAT (X02-DA) beamline at the Swiss Light Source, Paul Scherrer Institute, Villigen, Switzerland. Scans were performed at three locations (10, 30 and 50 mm from the chill) along the length of the samples with a voxel edge length of 1.85 μm and energy of 35 keV. Each scan consisted of 900 slices at intervals of 1.85 μm, corresponding to a scanned length of 1.665 mm. Median filtering of five voxels was used to reduce noise and smooth small features.

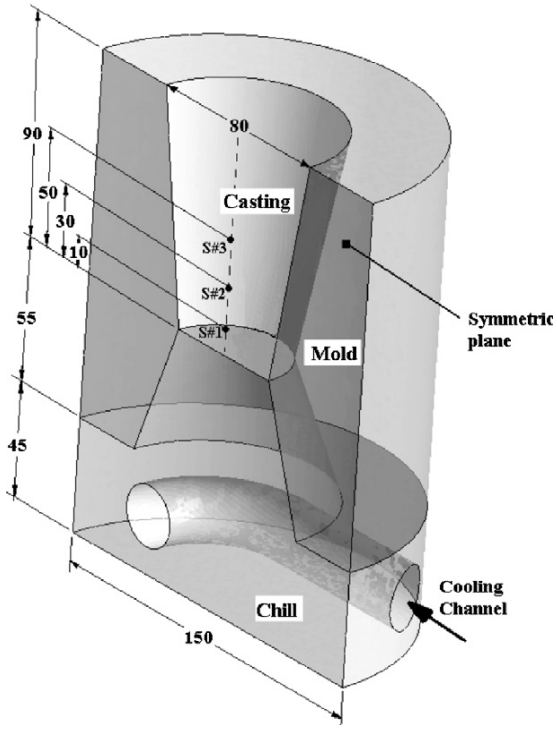

Figure 2.1 Schematic of a section of the mold and chill used to create tapered cylindrical casting. Sample (S) locations identified relative to chill. Units are in millimeters.

2.1.1.3 Microstructure

Examples of the resulting 3D geometry (constructed using AMIRA, a registered trademark of Visage Imaging GmbH, Berlin, Germany) of the primary phase along with a mid-length cross-sectional slice are shown in **Figure 2.2**. As shown in this figure, by increasing the copper content the fraction of eutectic phase increases. Moreover, by decreasing the cooling rate, i.e. increasing the distance from the chill, the microstructure becomes coarser. The inverse of the specific surface area (S_v^{-1}), solid fraction and the fraction of isolated liquid regions are summarized in **Table 2.1** for each sample. S_v^{-1} has been calculated based on the Marching Cube method which provides a more accurate estimation of surface area [84]. S_v^{-1} represents the tortuosity of the flow channels and is smaller for a more tortuous structure, i.e. finer microstructure. S_v^{-1}, reported in **Table 2.1** is referred to as the "effective" S_v^{-1} because it was calculated considering only those portions of the domain open to flow.

Brown et al. [23] observed that at high solid fractions some interdendritic regions become enclosed by solid phase and hence are isolated from the interdendritic channel network. When this occurs, these regions do not contribute to interdendritic flow and the effective values of f_s and S_v^{-1} are higher. In addition to the effect of solid fraction, the tortuosity of the interdendritic channels affects the size and distribution of isolated liquid regions. **Figure 2.3** shows the effect of S_v^{-1}, as a quantitative representation of the flow channel tortuosity, on the fraction of isolated liquid regions. The different Al–Cu alloys in this plot represent different f_s conditions. As shown in this figure, the fraction of isolated liquid regions increases as interdendritic channels become more tortuous, i.e. S_v^{-1} decreases, and as copper content is decreased, i.e. f_s increases. The ability to identify isolated regions of liquid and to determine

the effective f_s and S_v^{-1} is directly linked to availability of accurate 3D microstructure data such as that obtained from XMT.

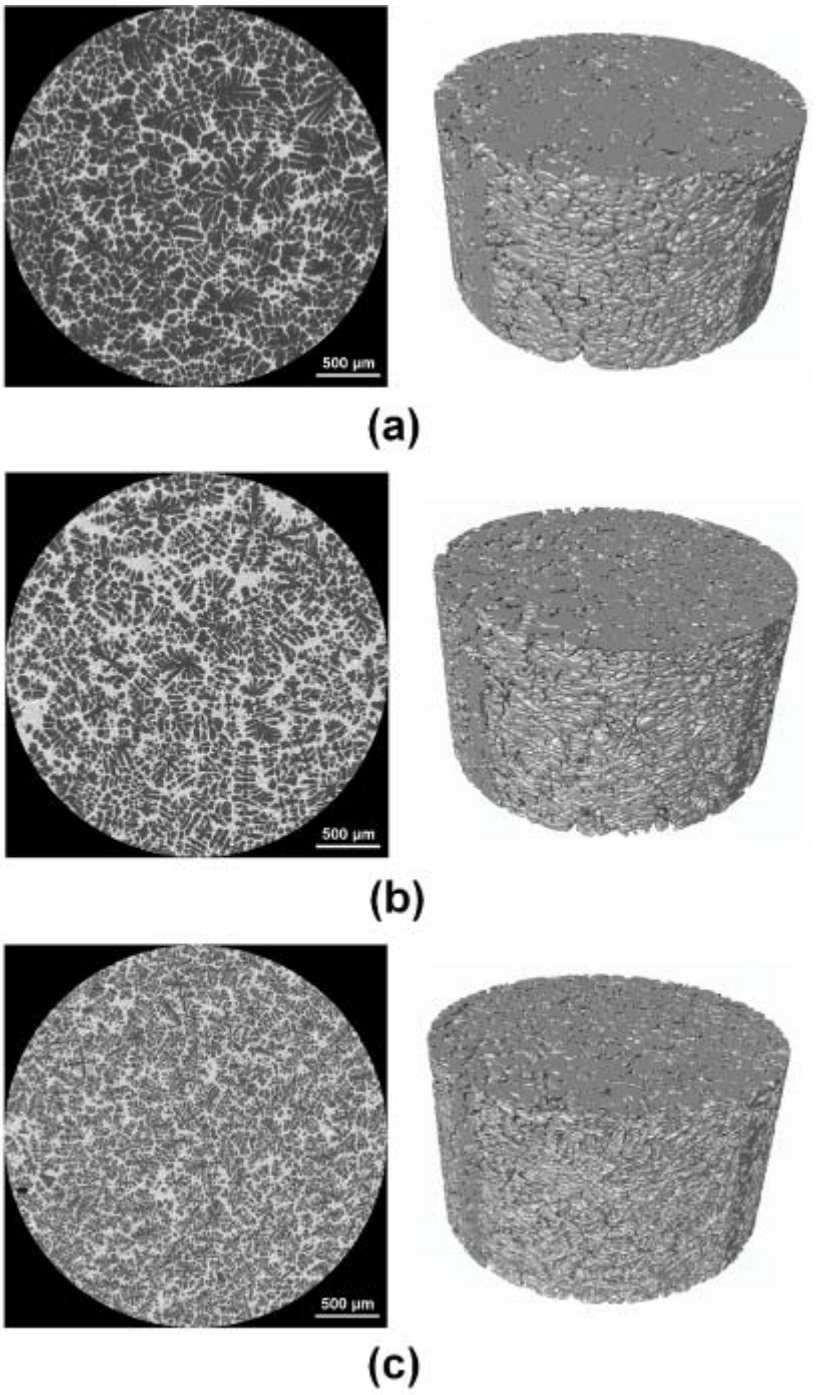

Figure 2.2 3D representation of the primary Al phase and mid-length cross-sectional slice extracted from XMT data for (a) Al–12 wt.% Cu, 50 mm from chill; (b) Al–19 wt.% Cu, 50 mm from chill; and (c) Al–19 wt.% Cu, 10 mm from chill.

Table 2.1 Near-eutectic microstructural parameters of Al-Cu alloys

Sample #	Alloy (wt%Cu)	Distance from chill (mm)	Solid fraction	Isolated liquid fraction	S_v^{-1} * (μm)
1	10	30	0.807	0.049	52.8
2	10	30	0.840	0.048	55.6
3	10	50	0.840	0.041	63.8
4	12	10	0.832	0.041	41.6
5	12	30	0.815	0.038	51.0
6	12	30	0.828	0.034	53.2
7	12	50	0.792	0.029	70.2
8	15	10	0.666	0.028	24.6
9	15	30	0.677	0.021	29.6
10	15	50	0.650	0.013	43.2
11	19	10	0.552	0.011	21.2
12	19	30	0.581	0.008	25.6
13	19	30	0.586	0.007	25.0
14	19	50	0.571	0.003	34.8
15	25	10	0.283	0.000	9.21
16	25	30	0.292	0.000	13.8
17	25	50	0.301	0.000	16.2

* reported S_v^{-1} is for non-scaled microstructure

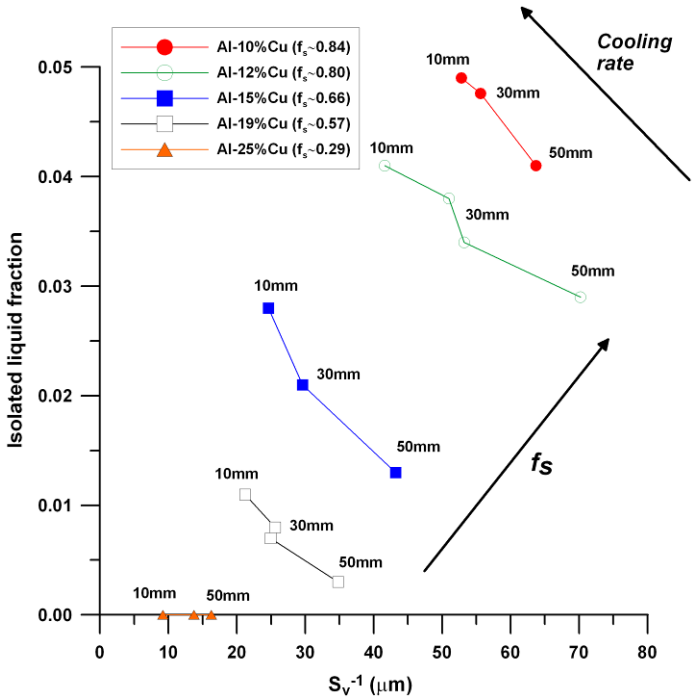

Figure 2.3 Isolated liquid fraction as a function of microstructural length scale, S_v^{-1}, for the different Al–Cu alloys analyzed in this study. Distance from the chill has been specified.

2.1.2 Microstructure evolution during solidification of Al-4.5wt%Cu

Al-4.5wt%Cu castings with a range of dendritic microstructures were produced for this investigation by varying the pre-solidification cooling rate and by quenching at intermediate points during solidification. This was done to characterize the evolution of microstructure during equiaxed dendritic solidification for different thermal conditions. Samples from these castings were characterized by XMT analysis, which allowed the pre-quench dendritic microstructure to be separated from the post-quench phases based on grey-scale. The permeability is then determined using the geometry of post-quench phase which represents the liquid domain prior to quenching.

2.1.2.1 Sample preparation

A series of castings, with the nominal composition of Al-4.5wt%Cu, were produced by melting appropriate amounts of commercially pure Al and Al-50wt%Cu master alloys in a resistance furnace. Prior to pouring, the melt was degassed by bubbling Ar through the melt and skimmed to remove any dross that may have accumulated. The castings were poured with a melt temperature of 720°C and solidified in cylindrical copper molds with two different diameters (D) of 19 and 29 mm, shown in **Figure 2.4**. The inside of each mold was coated with a thin layer of boron nitride and preheated to 300°C prior to pouring. The molds were insulated with N17 refractory board from Pyrotek (Pyrotek Inc., Spokane, WA, USA) on the bottom and the top (after pouring) to promote radial cooling. The temperature history in each casting was measured by placing a calibrated type-K thermocouple from OMEGA (OMEGA Engineering Inc., Stamford, CT, USA) at the mid-point of the centerline of the casting. Temperatures were recorded at 2 Hz using a 24-bit USB-based temperature data acquisition device (USB-TEMP) from Measurement Computing (Measurement Computing

Corporation, Norton, MA, USA).

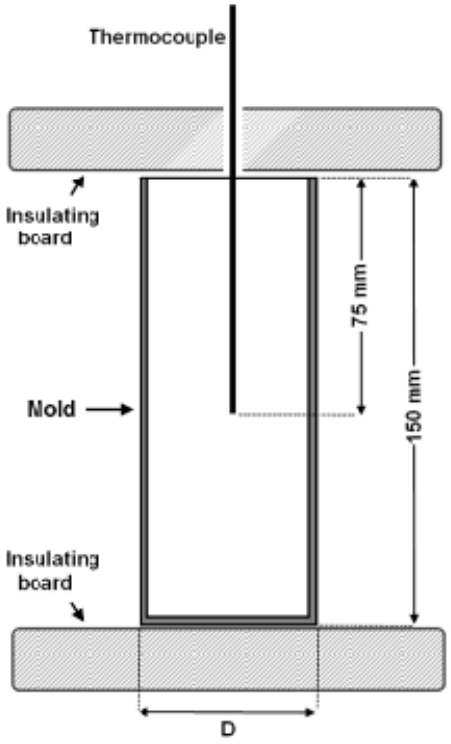

Figure 2.4. Schematic of the experimental setup used to produce castings for thermal analysis, XMT analysis, and microstructural analysis.

For each mold diameter, the first casting was allowed to completely solidify to establish a baseline cooling curve (refer to **Figure 2.5**). Six additional castings of each diameter were then poured and subsequently quenched at different temperatures (marked by arrows on the cooling curves in **Figure 2.5**) to obtain a variety of pre-quench dendritic volume fractions (0.35 to 0.8). Castings were quenched by plunging the copper mold into a water bath with a temperature of 25°C. Cylindrical samples, 3.0 mm diameter x 15 mm long, were removed from the centerline of each casting, near the thermocouple tip, for subsequent XMT analysis.

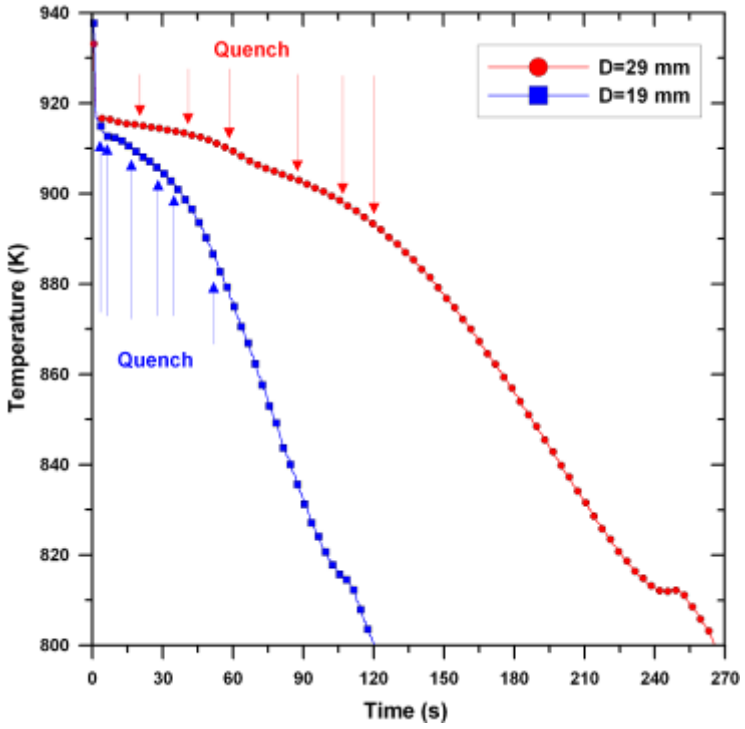

Figure 2.5 Measured temperature histories of baseline (non-quenched) samples with mold diameters of 19 and 29 mm. Arrows identify the temperatures at which samples have been quenched.

2.1.2.2 X-ray microtomography

XMT analysis was performed in the same manner as discussed in section **2.1.1.2**. Examples of the resulting cross-sectional slices from castings with different quench temperatures and mold diameters are shown in **Figure 2.6**. As shown, the volume fraction of pre-quenched dendritic phase increases as the quench temperature decreases. Moreover, the pre-quenched dendritic phase becomes finer as cooling rate increases, i.e. mold diameter decreases.

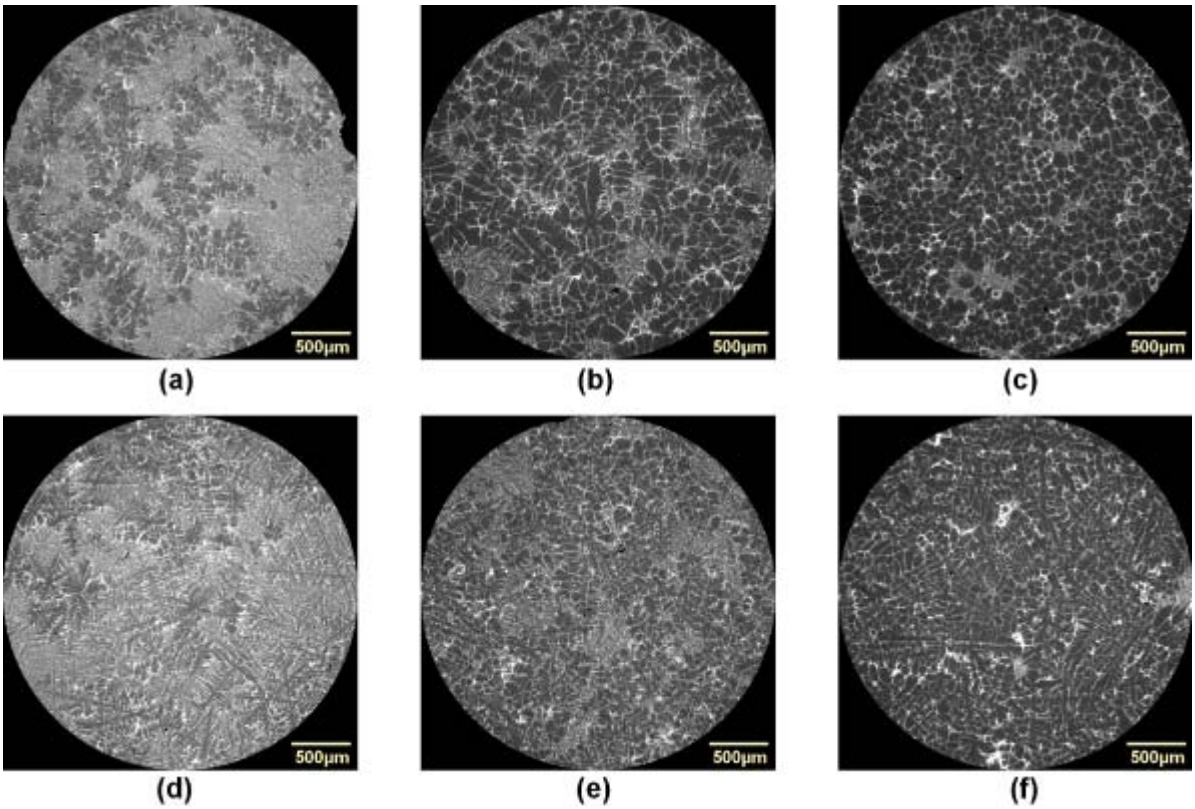

Figure 2.6 Example cross-sectional slices extracted from XMT analysis of the quenched samples for the mold diameters of 29 mm (a, b and c) and 19 mm (d, e and f). The quench temperatures were (a) 915 K, (b) 910 K, (c) 893 K, (d) 915 K, (e) 910 K, and (f) 883 K.

2.1.2.3 Image processing

The difference in X-ray attenuation between the Al-rich and Cu-rich phases results in contrast in the resulting image (refer to **Figure 2.6**) that allows the separation of the pre-quench and post-quench structures based on grey-scale. This phase contrast improves as the difference in Cu content between the different phases increases. Consequently, samples quenched at later stages in the solidification interval, i.e. lower quench temperature, show better contrast and separating the pre-quench and post-quench phases can be achieved using a single grey-scale threshold. However, samples quenched early in the solidification range

were more difficult to analyze due to the smaller grey-scale range of the resulting image. For such samples, pre- and post-quench phase separation was achieved by repeatedly post-processing the XMT data using the following procedure: i) applying a gray-scale threshold for each sample, ii) employing a median filter of 3 voxels to reduce noise and smooth small features, and iii) growing and then shrinking the darker phase (Al rich) by 1 voxel. This procedure was repeated 4 to 5 times on each image slice, in order to achieve an acceptable binary structure, i.e. with pre-quench and post-quench phases identified by black and white. An example of this process for one slice is shown in **Figure 2.7**.

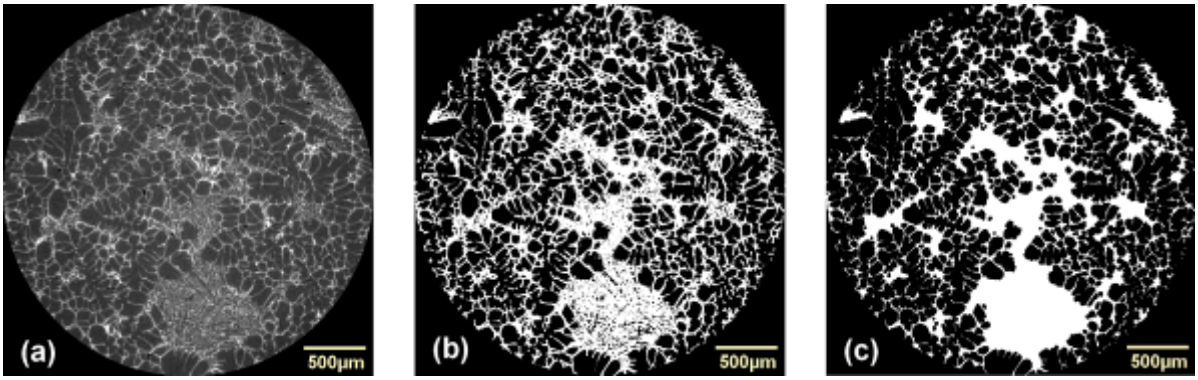

Figure 2.7 (a) Example cross-sectional slice extracted from the XMT data for the sample with a mold diameter of 29 mm and a quench temperature of 910 K. (b) and (c) are processed images of (a) after 1 and 4 segmentation steps, respectively.

Microstructural parameters, including the SDAS and the solid/liquid interfacial area per unit volume, were extracted from the geometry data following phase separation and isosurface extraction. The SDAS of each sample was determined by measuring the distance between 50 to 60 pairs of secondary dendrite arms on selected slices from the XMT analysis and averaging the measured values. S_v^{-1} and the solid fraction were extracted by analyzing the 3D isosurface data using Marching Cube method. These microstructural parameters will

then be used in the analysis of the permeability evolution.

2.1.2.4 Microstructure

The secondary dendrite arm spacing (SDAS), inverse of the specific surface area (S_v^{-1}), and the solid fraction for the Al-4.5wt%Cu samples solidified with different cooling rates and quench times are summarized in **Table 2.2**. In the following sections, the effects of the quenching process and subsequent image processing on determining the evolution of solidification and also the relation between two microstructural length scales (S_v^{-1} and SDAS) are assessed.

Table 2.2 Microstructural parameters during solidification of Al-4.5wt%Cu alloy

Sample #	Mold diameter (mm)	Quench Temp. (K)	Solid fraction	SDAS (μm)	S_v^{-1} (μm)
1	19	915	0.34	26±5	6.39
2	19	913	0.44	28±6	8.41
3	19	910	0.53	39±7	9.76
4	19	905	0.61	48±7	12.12
5	19	902	0.65	49±7	13.18
6	19	883	0.79	59±7	17.07
7	29	915	0.37	41±5	11.62
8	29	913	0.48	53±5	12.83
9	29	910	0.57	58±6	14.59
10	29	903	0.65	68±6	18.02
11	29	898	0.70	70±7	20.52
12	29	893	0.74	71±7	20.18

2.1.2.4.1 Solid fraction

To determine the effects of the quench procedure used during casting and the subsequent image analysis technique (described in section **2.1.2**) on the observed solid fractions, the measured solid fractions versus quench temperatures of the samples listed in **Table 2.2** were compared to those calculated using the Lever rule and Scheil model (**Figure 2.8**). For the Scheil model, the Scheil-Guilliver model implementation in Thermo-Calc (Thermo-Calc AB,

Sweden) using the TTAL6 database was used. As shown in **Figure 2.8**, the measured solid fractions from the characterized microstructures are in good agreement with the Scheil model predictions. These results indicate that the quench procedure and subsequent image analysis techniques employed in this study were effective in isolating and characterizing the microstructure at intermediate stages during solidification. More accurate information on the evolution of solid fraction can be obtained from Cooling Curve Analysis (CCA).

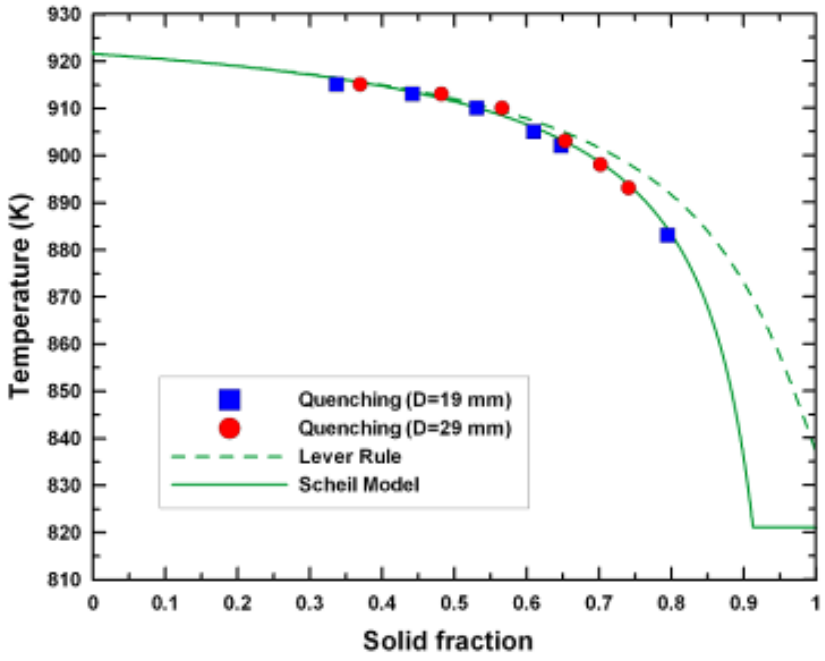

Figure 2.8 Solid fraction versus temperature for the samples listed in Table 2.2. Solid line and dash line represent the Scheil model and Lever rule, respectively.

2.1.2.4.2 S_v^{-1} versus SDAS

The dendritic morphology of a solidifying alloy is determined by the cooling rate and thermal gradient. At low cooling rates, the dendritic microstructure coarsens during cooling, i.e. within the mushy zone [64]. During this coarsening, the SDAS increases reflecting an increase in the length scale of the microstructure. In permeability expressions, the length scale commonly used to characterize a solidifying microstructure is the inverse of solid/liquid

interfacial area per unit volume of solid (S_v^{-1}). For dendritic structures, a regular array of dendrites with cylindrical arms [76] can be used to approximate this length scale. With such a geometric simplification and assuming the radius of a dendrite arm, R, is equal to $0.5d_2$ as in [76], S_v^{-1} is equal to $d_2 / 4$ where d_2 is the SDAS. **Figure 2.9** shows the SDAS versus S_v^{-1} for samples listed in **Table 2.2**. For comparison, the line representing S_v^{-1} equal to $d_2 / 4$ has been plotted. As shown in **Figure 2.9**, the cylindrical assumption of the secondary dendrite arm shape appears to be an acceptable representation of the dendritic structure. Hence, S_v can be roughly estimated as $4 / d_2$.

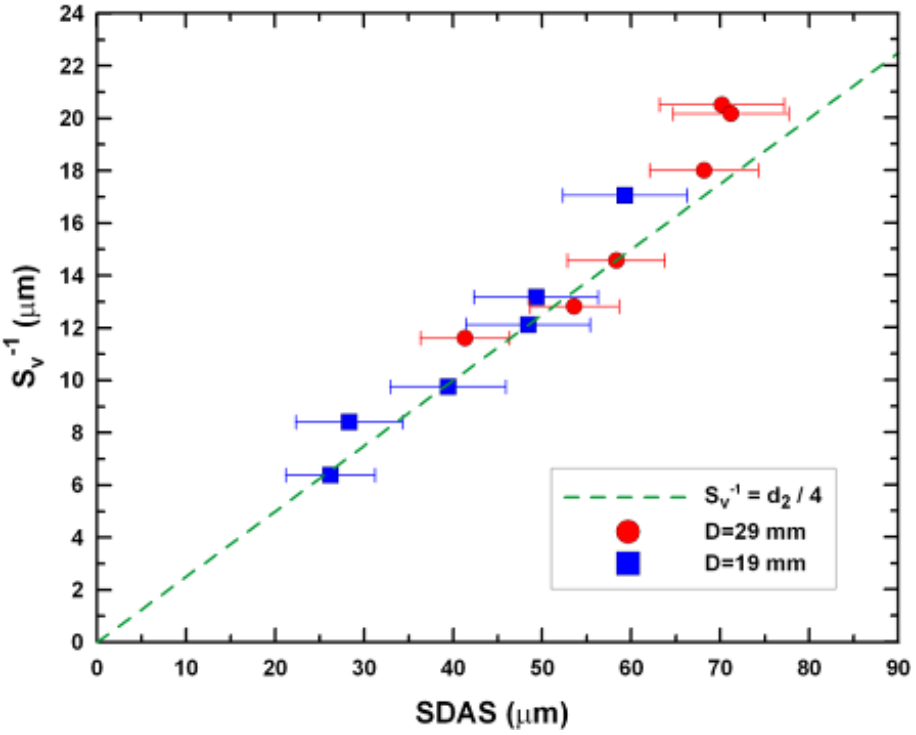

Figure 2.9 SDAS versus the inverse of solid/liquid interfacial area per unit volume of solid (S_v^{-1}) for samples listed in Table 2.2. Dash line represents S_v^{-1} variation with SDAS (d_2) assuming a cylindrical shape for dendrite arms (i.e. $S_v^{-1} = d_2/4$).

To accurately determine the evolution of the microstructural length scale (either d_2 or S_v^{-1}) during dendritic solidification of an alloy, knowledge of the mechanism governing

microstructural coarsening is required. Two coarsening mechanisms are usually observed during dendritic solidification. Ripening is the first coarsening mechanism where smaller dendrite arms disappear and feed the growth of larger dendrite arms. The other mechanism is the coalescence of adjacent dendrite arms, which leads to the progressive filling of the space between dendrite arms. Evidence of both types of coarsening mechanism was observed in the samples characterized for this study.

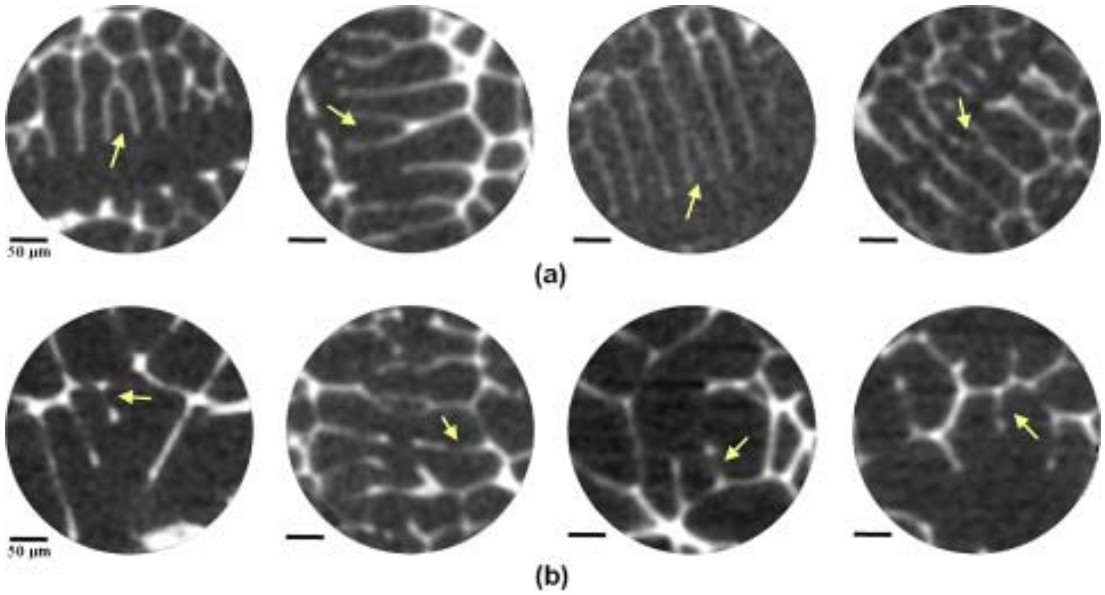

Figure 2.10 2D images extracted from XMT data showing different coarsening mechanisms in the scale of dendrite arms: (a) remelting of smaller dendrite arms; (b) joining of the tips of dendrite arms.

Figure 2.10 shows examples of these coarsening phenomena occurring within the microstructure where individual secondary dendrite arms appear to be growing at the expense of their neighbors (**Figure 2.10a**) as well as joining together (**Figure 2.10b**). Additionally, the dendrite arms shown in **Figure 2.10** have complex shapes rather than being cylindrical. Moreover, the deviation from the cylindrical shape appears to increase as coalescence dominates. Using in-situ and real time 3D microtomography characterization of dendritic

solidification in an Al-Cu alloy, Limodin et al. [64] recently observed that ripening is the dominant coarsening mechanism at low solid fraction and that this gives way to coalescence of adjacent dendrite arms at high solid fraction. Due to the complexity and uncertainty in describing dendritic coarsening, a comprehensive investigation focused on the evolution in the microstructural length scale is needed to further improve the microstructure characterization during dendritic solidification.

Previous research on evaluating the microstructural length scale assumes that those dendrite arms that spent more time in the mushy zone than others will have more time to coarsen. For example, based on a theoretical model of dendrite ripening [76], d_2 was found to be proportional to the cube root of time spent in the mushy zone ($t^{1/3}$). As discussed, for dendritic structures, S_v^{-1} is proportional to d_2. Hence, the variation of S_v^{-1} versus $t^{1/3}$, shown in **Figure 2.11**, is proposed in this work as a means of determining the length scale. As shown, fitting a curve in the form of $S_v^{-1}=Bt^{1/3}$, results in a B value of $4.2\ \mu m\ s^{-1/3}$ with a good R^2 of 0.94. Taking into account the cylindrical approximation of the dendrite arm shape, i.e. $S_v^{-1}=d_2/4$, this leads to $d_2=16.8t^{1/3}$. This is in close agreement with Young and Kirkwood's experimental results [85] where they reported the variation of d_2 with time as $d_2=16t^{0.31}$. The contribution of each coarsening mechanism may depend on the alloy and thermal condition. Although the results of this study (refer to **Figure 2.11**) suggest that the ripening mechanism dominates coarsening for the range of solid fraction and cooling rate studied, Terzi *et al.* [86] found that S_v^{-1} is proportional to $t^{1/4.4}$ based on in-situ 3D microtomography of an Al-10wt%Cu alloy. This deviation from proportionality to $t^{1/3}$ was attributed to the prevalence of coalescence during dendrite coarsening.

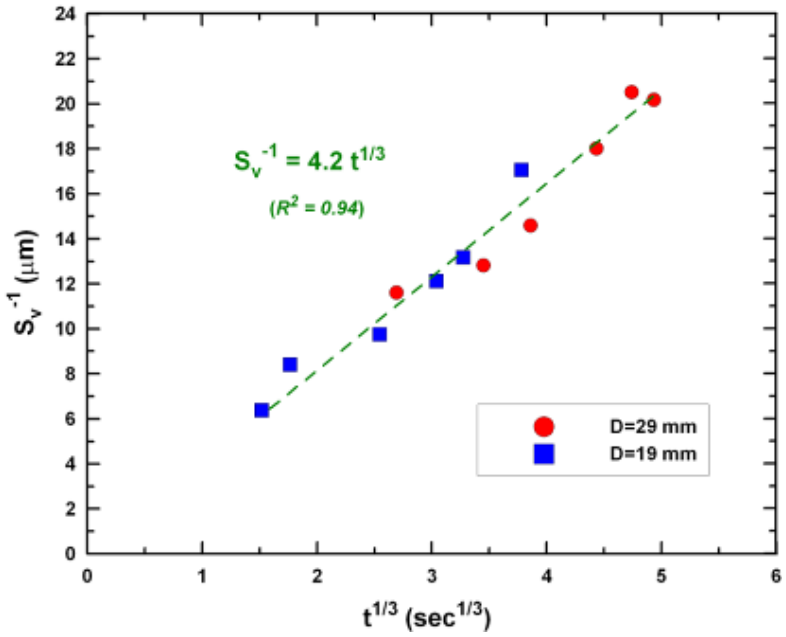

Figure 2.11 S_v^{-1} versus the cube root of time spent in the solid/liquid zone ($t^{1/3}$) for samples listed in Table 2.2. Dash line represents a fitted curve in the form of $S_v^{-1} = Bt^{1/3}$ resulting a B value of 4.2 μm $s^{-1/3}$.

2.2 Numerical characterization of eutectic solidification

To study the evolution of permeability during the solidification of hypoeutectic aluminum alloys, the evolution of microstructure for the complete solidification range must be characterized. As discussed in section **2.**1, the evolution of microstructure during equiaxed dendritic solidification of Al-Cu alloys may be readily obtained using 3D XMT. This is due to fact that because of small partition coefficient of copper in the solid and liquid phases, the copper content in the solidifying dendritic phase is lower than the liquid phase. During eutectic transformation, however, copper is not partitioned between solid and liquid phases which make the use of XMT characterization impractical. Alternatively, using 3D geometries of the near-eutectic microstructure, the eutectic transformation may be modeled to obtain the remaining evolution of the solidified microstructure. For this purpose, the nucleation and

growth behavior of the equiaxed eutectic grains formed during hypoeutectic Al–Cu alloy solidification have been modeled using a deterministic CA technique. To analyze the solidification kinetics, an inverse analysis algorithm has been applied to the microstructure prediction model to calculate the material constants in the nucleation and growth relationships through comparison with experimental observations.

2.2.1 Experimental procedure

A series of Al-Cu alloy castings were produced to i) perform thermal analysis to determine the evolution of solid fraction versus temperature, ii) analyze the eutectic grain structure resulting from mid-eutectic transformation quenching, and iii) characterize the 3D microstructure for use as the initial condition in the CA model.

The castings, listed in **Table 2.3**, were produced from Al with 20wt%Cu. One batch of melt was prepared for all castings by melting appropriate amounts of commercially pure Al and Al-50wt%Cu master alloy in a resistance furnace.

Table 2.3 Description of experimental conditions

Sample	Mold diameter (mm)	Cooling channels activated	Air pressure (bar)	Average cooling Rate* ($K\ s^{-1}$)
1	29	Yes	0.41	1.10
2	29	Yes	0.21	0.92
3	19	No	-	0.59
4	29	No	-	0.33
5	35	No	-	0.27
6	52	No	-	0.19

* Cooling rate during primary phase solidification

Prior to pouring, the melt was degassed by bubbling Ar through the melt and skimmed to remove any dross that may have accumulated. The castings were poured with a melt

temperature of 650°C and solidified in cylindrical copper molds with different diameters (D), shown in **Figure 2.12**. The inside of each mold was coated with a thin layer of boron nitride and preheated to 300°C prior to pouring. The molds were insulated with refractory board (Pyrotech N17) on the bottom and the top (following pouring) to promote radial cooling. For two castings (Samples 1 and 2 in **Table 2.3**), air was blown through nozzles uniformly distributed around the molds to increase the cooling rate.

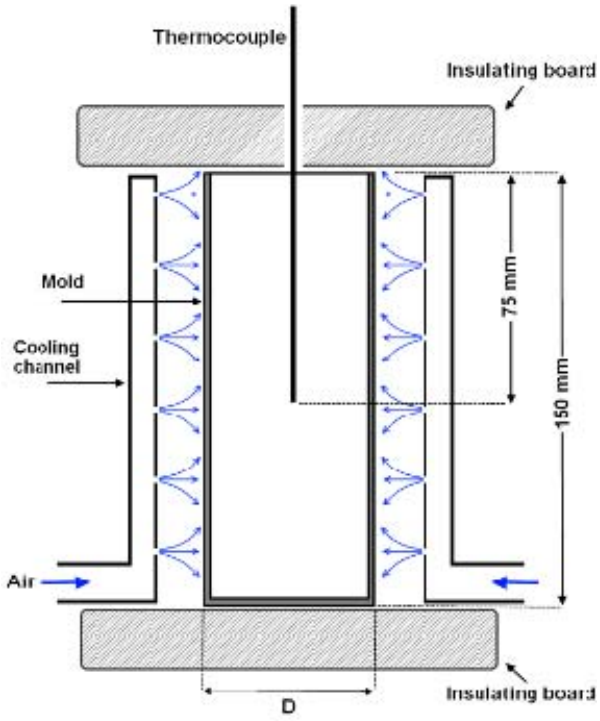

Figure 2.12 Schematic of the experimental set-up used to produce castings for thermal analysis, XMT analysis and microstructural analysis. Five air channels, each with 6 nozzles were equally spaced around the copper mold and were activated for samples 1 and 2.

The temperature history in each casting was measured by placing a calibrated type-K thermocouple (0.005" diameter with special limits of error from OMEGA) on the centerline, half way up the casting. Temperatures were recorded at 2 Hz using a 24-bit USB-based temperature acquisition device (USB-TEMP) from Measurement Computing. **Figure 2.13**

shows the measured cooling curves for the samples listed in **Table 2.3**. The chemical composition of the cast alloy was measured by Inductively Coupled Plasma Mass Spectrometry (ICP-MS). The main components of the alloy are summarized in **Table 2.4**.

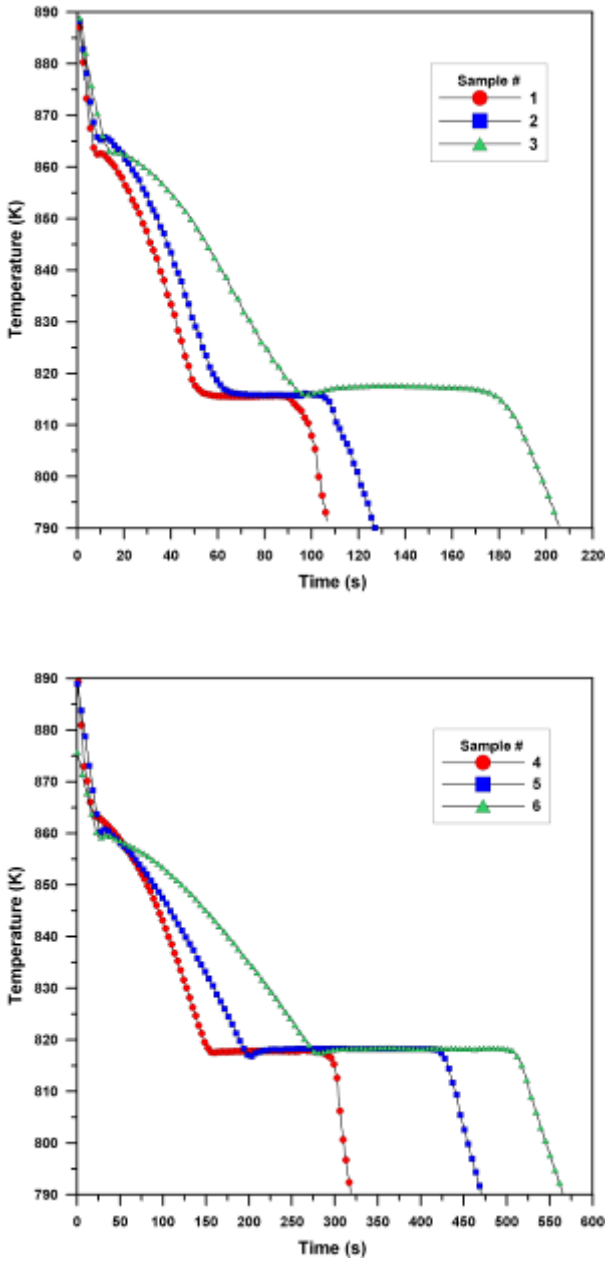

Figure 2.13 Measured temperature history for non-quenched samples listed in Table 2.3.

Table 2.4 Chemical composition of cast samples

Elements (wt%)							
Al	Cu	Si	Mg	Zn	Mn	Fe	Other
79.71	19.99	0.06	0.03	0.03	0.01	0.10	0.07

For each experimental condition (refer to **Table 2.3**), 2-3 castings were performed. The first casting for each condition was allowed to completely solidify; however, the additional castings were quenched at different times after the start of the eutectic transformation was observed via the measured temperature. Castings were quenched by plunging the copper mold into a water bath with a temperature of 25°C. The quenched samples were sectioned perpendicular to the axis of the cylinder at 65 mm from the bottom of the casting and prepared for metallography. A 3.0 mm diameter cylinder, 15 mm long, was removed from the centerline of the non-quenched samples for subsequent XMT analysis.

2.2.1.1 Cooling Curve Analysis (CCA)

The measured cooling curves of non-quenched samples for each experimental condition were analyzed with a CCA technique to provide information on the evolution of solid fraction versus temperature during solidification [87]. For the samples listed in **Table 2.3**, the *Biot* number (*hD/4k*) is smaller than 0.1, indicating that very small radial thermal gradients will develop and therefore, the sample temperature is a function of time alone and can be analyzed according to Newton's Law of cooling. Assuming heat loss to the surroundings is via convection only, the heat balance for a solidifying sample can be written as [88]:

$$\frac{dQ}{dt} - mC_p\left(\frac{dT}{dt}\right)_{CC} = hA_s(T - T_\infty) \qquad \textbf{Equation 2-1}$$

where *dQ/dt* is the rate of heat generated during solidification (J s^{-1}), *m* is the mass of the sample (kg), C_p is the specific heat of the sample (J kg^{-1} K^{-1}), $(dT/dt)_{CC}$ is the time derivative of temperature (K s^{-1}) calculated from the cooling curve, *t* is time (s), *h* is the effective heat transfer coefficient (W m^{-2} K^{-1}), A_s is the surface area of the sample (m^2), *T* is the sample temperature (K), and T_∞ is the ambient temperature (K). Before and after solidification, when *dQ/dt=0*, the cooling rate can be written as:

$$(\frac{dT}{dt})_{ZC} = -\frac{hA_s(T-T_\infty)}{mC_p} \qquad \textbf{Equation 2-2}$$

Equation 2-2 is called the "zero curve" and represents the cooling rate that would have occurred without the release of latent heat. It is obtained by fitting a polynomial to the first derivative of the temperature history in a region corresponding to single phase cooling. The rate of heat release during the liquid to solid phase transformation is then calculated by substituting **Equation 2-2** in to **Equation 2-1** as:

$$\frac{dQ}{dt} = mC_p\left[(\frac{dT}{dt})_{CC} - (\frac{dT}{dt})_{ZC}\right] \qquad \textbf{Equation 2-3}$$

By integrating **Equation 2-3**, the heat generated as a function of time is:

$$Q(t) = mC_p\int_0^t\left[(\frac{dT}{dt})_{CC} - (\frac{dT}{dt})_{ZC}\right]dt \qquad \textbf{Equation 2-4}$$

The solid fraction evolution with time is then calculated as [87, 88]:

$$f_s(t) = \frac{Q(t)}{Q_{total}} \qquad \textbf{Equation 2-5}$$

where Q_{total} is the total heat generated during solidification (J) and f_s is the solid fraction. **Figure 2.14** shows an example of the curves obtained for sample 3 using this method. These curves are then used as an input in the inverse analysis algorithm.

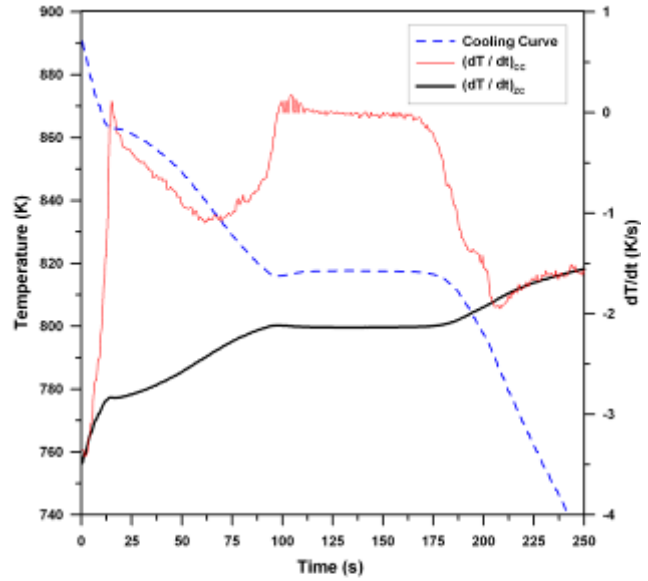

a)

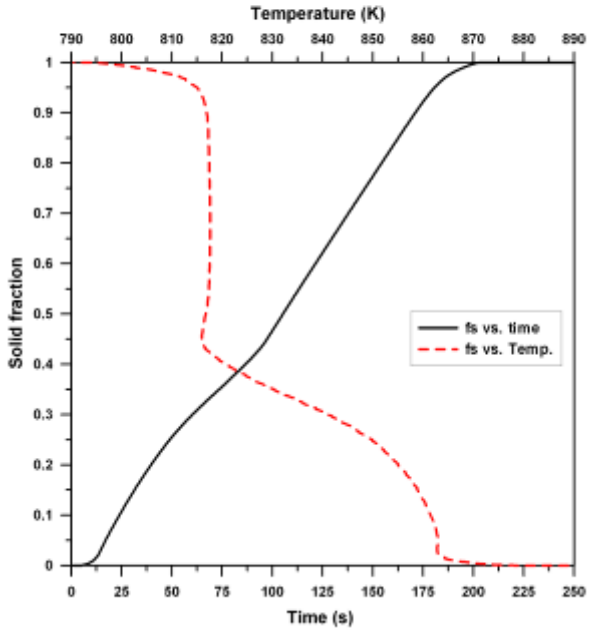

b)

Figure 2.14 a) Cooling curve, first derivative and Newtonian zero curve, and b) calculated evolution of solid fraction with time and temperature for sample 3.

2.2.1.2 Microstructural analysis

For each experimental condition, sections from each quenched sample were cut, mounted, ground, and polished with 1 μm diamond suspension. The polished samples were etched with a 0.1vol%HF solution to improve the contrast between the different phases during metallography. For each section, the number of eutectic grains in a unit area (N_A) and the average diameter of the eutectic grains (D_{cir}) at different locations on the polished surface were quantified as the mean value of measurements on 8 sequential images (each image had an area of 0.3 mm^2). N_A and D_{cir} were manually measured by counting the number of grains and dividing by the area of the image and by the intercept length method, respectively. The number of images used in this process was determined by evaluating the change in N_A and D_{cir} with progressively larger numbers of images. No appreciable change was noted in N_A and D_{cir} with more than 8 images. N_A and D_{cir} did not vary with location on the section indicating a uniform cross-sectional microstructure was achieved.

Employing stereology concepts, the mean diameter of randomly distributed spheres of the same size is proportional to $4/\pi$ times the mean diameter of the circles formed on an intersecting plane [89]. Approximating eutectic grains as uniform size spheres, the mean diameter of the eutectic grains in 3D is:

$$D_{sph} = \frac{4}{\pi} D_{cir} \qquad \textbf{Equation 2-6}$$

If there are n spheres randomly distributed in the volume, the average number of circles expected on an intersection plane with area w^2 is $nD_{sph.}/w$. Dividing by the area of the section, the number of spheres in unit of volume is [89]:

$$N_V = \frac{N_A}{D_{sph}} \qquad \textbf{Equation 2-7}$$

2.2.1.3 X-ray Microtomography

XMT analysis was performed in the same manner as discussed in section 2.1.1.2. Scans were performed at the mid-lengths of the cylinders cut from each of the non-quenched samples with a voxel edge length of 1.85 μm and energy of 35 keV. Examples of the resulting 3D geometry of the primary phase are shown in **Figure 2.15**. The reconstructed microstructures confirm that the dendritic structure coarsened with decreasing cooling rate.

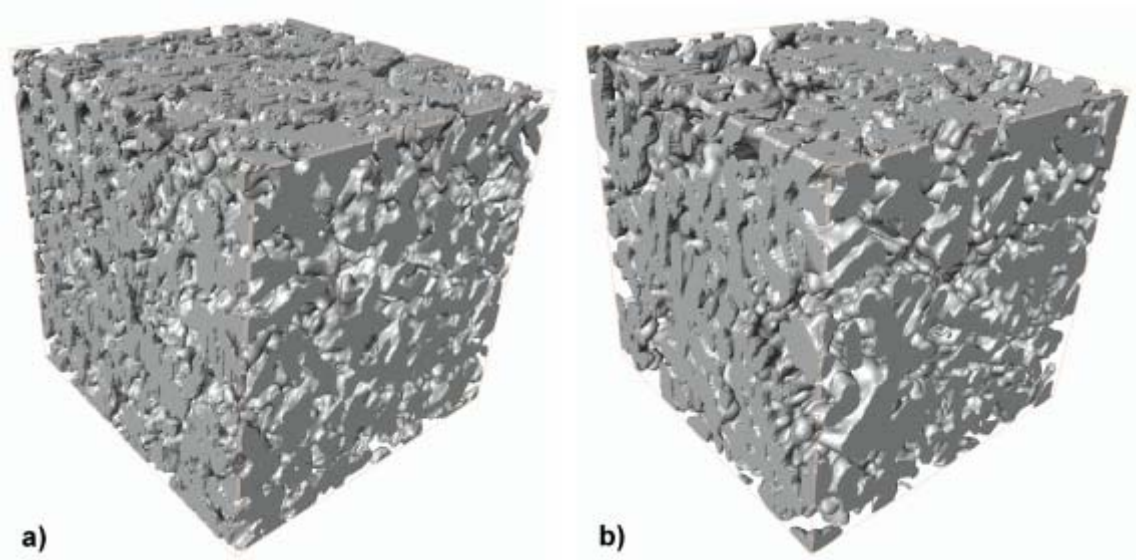

Figure 2.15 3D representation of the primary Al phase extracted from XMT data for a) sample 3, and b) sample 6. The cube edge length is 1 mm.

2.2.2 Numerical methods

A microstructure model has been developed to predict the evolution of eutectic grains. An inverse algorithm was then employed to calculate the constants in the nucleation and growth Laws to match the microstructure predictions with the experimental data for each condition (refer to **Table 2.3**), i.e. the calculated $f_s(t)$ from the CCA analysis of the non-quenched samples, and the measured $N_V(t)$ and $D_{sph.}(t)$ from the microstructural analysis of the

quenched samples. The microstructure model and the calculated nucleation and growth constants were then validated by comparison to additional experimental data.

2.2.2.1 Microstructure model

In developing the model described here, the diffusion of solute constituents in the liquid phase is assumed to be infinitely fast and that there is no diffusion in the solid phases. The temperature is assumed to be uniform throughout the domain and the link between the eutectic solidification on the microscopic scale and the heat flow occurring on the macroscopic scale is accomplished by using the recorded cooling curves of the non-quenched samples from the experiments. A Cellular Automaton (CA) model using deterministic relations for the nucleation and growth conditions has been developed to predict the evolution of the equiaxed eutectic phase formed during the solidification of hypoeutectic Al-20wt%Cu alloy. The domains used for these simulations employ the primary dendritic structures characterized by XMT analysis of the samples summarized in **Table 2.3** (i.e. different cooling rates).

2.2.2.1.1 Eutectic Cellular Automaton model

A CA model has been developed to predict the evolution of equiaxed eutectic grains by applying deterministic transformation rules. Although the nucleation and growth of eutectic grains are defined by deterministic relationships, the locations of the nucleation sites within the calculation domain are determined randomly. The calculation domain is a cube, with 1 mm edge length, that is divided into a regular network of uniform cubic cells with 5.55 μm edge length (180 cells in each direction). The state of each cell is characterized as either liquid, primary solid, or a eutectic grain number. After each time-step, the state of each cell is updated based on the transformation rules.

At the beginning of the calculation, the states of all cells are set to either -1 (primary solid) or 0 (liquid) based on the overlaid dendritic structure from the XMT data. Due to the small *Bi* number of the castings and the small size of the microstructure domain, the temperature is assumed to be uniform throughout the domain and equal to the measured temperature history of the non-quenched samples starting from the eutectic temperature.

The number of new grains which are formed between t-Δt and t is calculated as:

$$n = \left[\{N_V(t) - N_V(t-\Delta t)\}V_\Omega\right]_{\text{int}} \qquad \textbf{Equation 2-8}$$

where N_V is the number of nuclei per unit volume, V_Ω is the domain volume and $[]_{\text{int}}$ denotes the nearest integer function. For $n>0$, n random cells are chosen within the remaining liquid cells. The state variables of the selected cells are set to positive integer values representing a grain number.

The radius of each active eutectic grain is then updated according to **Equation 2-9**:

$$R_i^{t+\Delta t} = R_i^t + \frac{dR}{dt}\Delta t \qquad \textbf{Equation 2-9}$$

where dR/dt is the radial growth velocity of the eutectic grains. At this point, each cell in the domain is evaluated to determine the progression of the transforming grains. For each liquid cell, m, the distance from cell m to the center of grain i (d_{mi}) is calculated and if $d_{mi} \le R_i^{t+\Delta t}$, the cell index is changed to i.

A periodic boundary condition is applied to all six faces of the cubic domain. Although the dendritic structure is initially non-symmetric due to the stochastic nature of the solidified dendritic structure, by applying these boundary conditions to the domain, the effect of growing eutectic grains that may enter the domain is considered. A 2D example of how the periodic boundary condition has been applied is shown in **Figure 2.16**. Based on grain 1,

which is growing out the right face, a new grain (grain 2) with the same index (orientation) is introduced on the left side. The center of grain 2 has the same distance from the left face as grain 1 has from the right side.

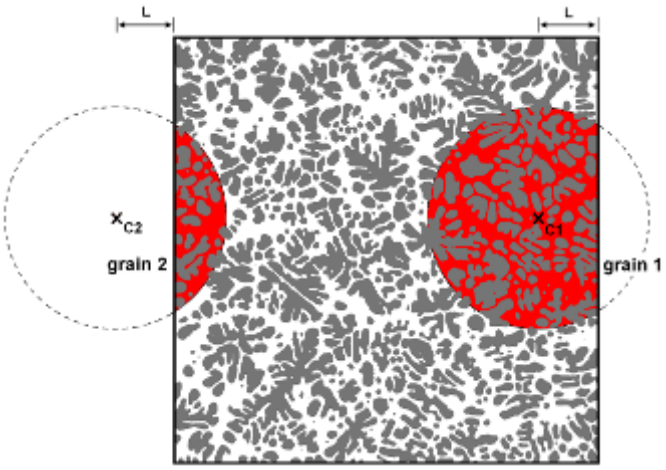

Figure 2.16 Example application of periodic boundary condition to a 2D computational domain where grain 1 grows out of the domain and a new grain (grain 2) is introduced on the opposite side with its center outside the domain. Grain 1 has the same distance (*L*) from right side as grain 2 has from the left side.

2.2.2.1.2 Nucleation and growth kinetics

Based on the work by Yang et. al. [80] on an Al-Si-Mg alloy (A356), continuous nucleation is assumed to occur in the Al-20wt%Cu alloy used in this study. Using the Oldfield nucleation Law [75], the number of active nuclei per unit volume is:

$$N_V = \beta_1 \Delta T^{\beta_2} \qquad \textbf{Equation 2-10}$$

where β_1 and β_2 are parameters that depend on the alloy type and nucleation potential and must be evaluated experimentally, and ΔT is the local undercooling.

The growth of both dendritic and eutectic phases in multicomponent alloys is complex. Most of the research on the growth of equiaxed microstructural phases characterize the growth velocity as a function of the undercooling using [80]:

$$\frac{dR}{dt} = \beta_3 \Delta T^2$$ **Equation 2-11**

where R is the radius of the eutectic grain and β_3 is a growth coefficient, which depends on the alloy and type of eutectic. At each time step, the measured and the eutectic temperatures are used to calculate undercooling as:

$$\Delta T(t) = T_{eut} - T(t)$$ **Equation 2-12**

2.2.2.1.3 Eutectic temperature

One of the key parameters required for the present microstructural model is the eutectic temperature. Although for a binary alloy system it can be found easily from the phase diagram, complications arise for multicomponent alloys. The stability temperature of each phase is concentration dependent and may change as transformation proceeds if solute is being depleted and enriched ahead of the transformation front. When dealing with a multicomponent alloy, such as the alloy used in this study (refer to **Table 2.4**), multiple solute transport equations must be solved to determine the instantaneous composition. In a multicomponent alloy system, the eutectic transformation may involve more than interlaminar solute redistribution, hence, the redistribution of all solute components must be considered.

A simplified approach using the Scheil-Gulliver model has been employed in this investigation to calculate the stability temperatures. With this approach, it is assumed that diffusion in the liquid phase is infinitely fast and that there is no diffusion in the solid phases. The Scheil-Gulliver model implementation in Thermo-Calc (Thermo-Calc is a registered trademark of Thermo-Calc AB, Sweden) using the TTAL6 database has been applied in this study. The calculated variation in liquid concentration and solid fraction with temperature are

shown in **Figure 2.17** and **Figure 2.18**. During eutectic transformation of binary Al-Cu alloys, solute element, i.e. Cu, is not partitioned between solid and liquid phases. However, as shown in **Figure 2.17**, the concentration of solute elements changes, even after the start of eutectic transformation (~820 K), for the multicomponent alloy of this study. This partitioning of solute elements leads to depression of eutectic temperature as solidification proceeds. **Figure 2.18** also shows the stability temperatures of the different phases. The portion of the curve in which Al_2Cu is stable (flat part of the curve) is the stability temperature of the eutectic phase and is used as the reference temperature (T_{eut}) in the microstructure model. For comparison, the eutectic temperature of a binary Al-Cu alloy has been also plotted (dashed-dot line). While the eutectic temperature of binary Al-Cu alloys is independent of solid fraction, the multi-component alloy used in this study exhibits a decreasing eutectic temperature with increasing solid fraction.

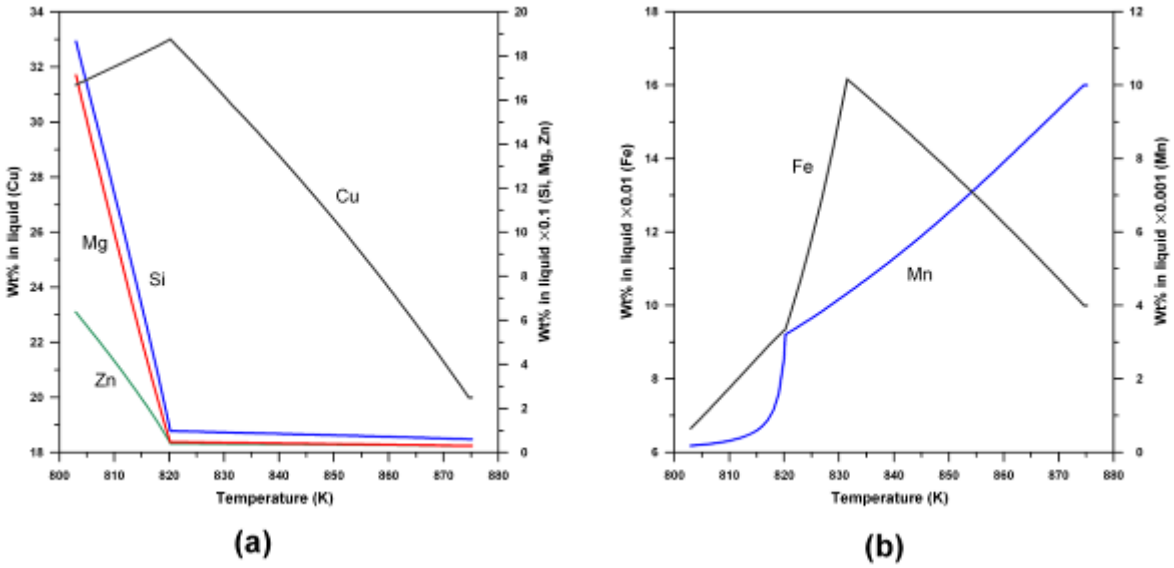

Figure 2.17 Variation of a) Cu, Si, Mg and Zn, and b) Fe and Mn concentration in the liquid with temperature for the alloy listed in Table 2.4.

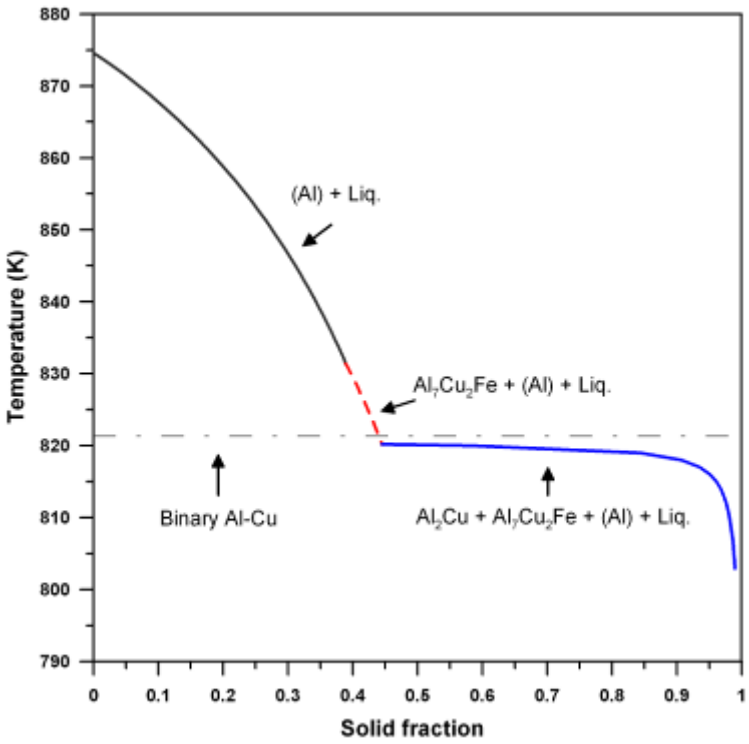

Figure 2.18 Variation of solid fraction with temperature for the alloy listed in Table 2.4. The plot also contains the stability temperature of different phases and eutecic temperature of binary Al-Cu alloy (Dash-Dot line).

2.2.2.2 Inverse analysis method

The transformation rules define the nucleation and growth behavior of the eutectic phase in the CA model and their accuracy determines the overall accuracy of the microstructure model. The three constants in the nucleation and growth kinetics equations (**Equation 2-10** and **Equation 2-11**) were initially estimated by a trial and error approach where a set of constants would be used and the resulting predictions compared with the measured results. The highly non-linear response of the model made this impractical. Instead, an approach based on the Inverse Analysis method has been applied to determine the three constants. In this approach, the measured experimental data, i.e. $f_s(t)$, $N_V(t)$, and $D_{sph.}(t)$, from each quenched sample were used to deduce $\beta=\{\beta_1, \beta_2, \beta_3\}$ via a minimization of the function:

$$R(\beta) = \sum_i \frac{[f_s^m(t_i) - f_s^c(t_i)]^2}{\sigma_{f_s}^2} + \sum_i \frac{[N_V^m(t_i) - N_V^c(t_i)]^2}{\sigma_{N_V}^2} + \sum_i \frac{[D_{sph.}^m(t_i) - D_{sph.}^c(t_i)]^2}{\sigma_{D_{sph.}}^2} + \sum_i \frac{[\beta_i^{new} - \beta_i^{old}]^2}{\sigma_\beta^2}$$

Equation 2-13

where σ_α is the typical error associated with the measurement of variable α, and superscripts m and c denote the measured and calculated variables, respectively. In order to minimize $R(\beta)$, its first derivative should be equal to zero:

$$\frac{\partial R}{\partial \beta_r} = 0$$

Equation 2-14

where β_r represents the three constants, i.e. r equals 1,2, and 3. Defining the derivative as:

$$f_r = \frac{\partial R(\beta)}{\partial \beta_r} = \sum_i \frac{-2[f_s^m(t_i) - f_s^c(t_i)]}{\sigma_{f_s}^2} \frac{\partial f_s^c(t_i)}{\partial \beta_r} + \sum_i \frac{-2[N_V^m(t_i) - N_V^c(t_i)]}{\sigma_{N_V}^2} \frac{\partial N_V^c(t_i)}{\partial \beta_r} + \sum_i \frac{-2[D_{sph.}^m(t_i) - D_{sph.}^c(t_i)]}{\sigma_{D_{sph.}}^2} \frac{\partial D_{sph.}^c(t_i)}{\partial \beta_r} + \frac{2[\beta_i^{new} - \beta_i^{old}]}{\sigma_\beta^2}$$

Equation 2-15

A sensitivity matrix may then be calculated as:

$$f_{r,q} = \frac{\partial f_r}{\partial \beta_q} = \sum_i \frac{2}{\sigma_{f_s}^2} \frac{\partial f_s^c(t_i)}{\partial \beta_r} \frac{\partial f_s^c(t_i)}{\partial \beta_q} + \sum_i \frac{2}{\sigma_{N_V}^2} \frac{\partial N_V^c(t_i)}{\partial \beta_r} \frac{\partial N_V^c(t_i)}{\partial \beta_q} + \sum_i \frac{2}{\sigma_{D_{sph.}}^2} \frac{\partial D_{sph.}^c(t_i)}{\partial \beta_r} \frac{\partial D_{sph.}^c(t_i)}{\partial \beta_q} + \frac{2\delta_{r,q}}{\sigma_\beta^2}$$

Equation 2-16

where $\delta_{r,q}$ is Kronecker's delta function of r and q. Starting with initially guessed values for β_q^0, the new β_q are calculated as:

$$\beta_q^{new} = \beta_q^{old} + \Delta\beta_q$$ **Equation 2-17**

The increments of the parameters $\Delta\beta_q$ are found for each iteration as the solution to the set linear equations:

$$f_{r,q} \cdot \Delta\beta_q = f_r$$ **Equation 2-18**

The implementation of this inverse analysis method was written as a separate computer program that calls the CA model to determine the sensitivity matrix, estimate β_q, and calculate $f_s^c(t)$, $N_V^c(t)$, and $D_{sph.}^c(t)$ once the parameters β_q are known. The calculation of $\Delta\beta_q$ continues iteratively until a converged solution is achieved based on the change of the residual function ($\Delta R(\beta) \rightarrow 0$).

2.2.3 Results and discussion

To characterize the eutectic nucleation and growth kinetics for the Al-Cu alloy used in this study, the measured microstructure data were analyzed using an inverse analysis approach coupled to the CA model. The microstructure characterization performed during experimental activities of this study will be presented initially. The application of the inverse analysis along with a sensitivity analysis and perspectives on the current approach are then discussed.

2.2.3.1 Experimental results

SEM analysis of the microstructure from each quenched sample reveals a dendritic primary Al phase, and both coarse and fine Al-Al_2Cu eutectic structures formed before and after quenching, respectively. Reference images from sample 4 showing the different phases are shown in **Figure 2.19**.

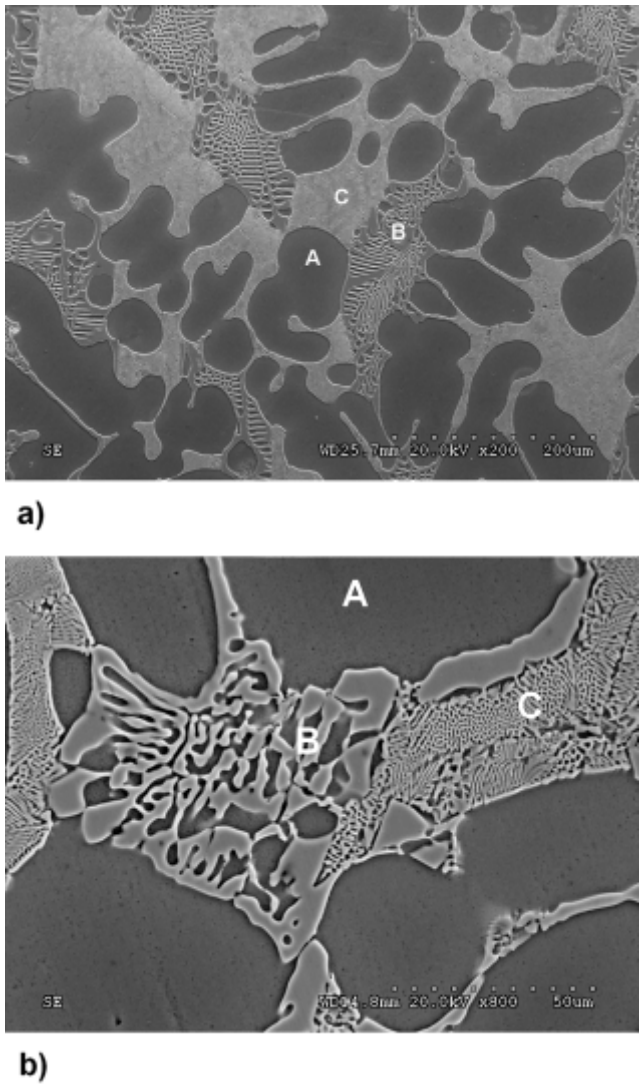

Figure 2.19 SEM micrographs of quenched sample 4 with the magnification of a) 200X and b) 800X. "A" is the primary Al phase, "B" is the pre-quench coarse Al-Al_2Cu eutectic, and "C" is the post-quench fine eutectic structure.

As shown in **Figure 2.19**, while the post-quench eutectic structure is predominantly regular, the eutectic structure before quenching exhibits some irregularity. This behavior in hypoeutectic Al-Cu alloys has been previously reported by Aravind et al. [81]. Although the different types of eutectic likely exhibit different growth rates, a single growth relation, representing the average growth velocity of all eutectic types, has been used in this study to describe the complex eutectic growth pattern. As a result, all eutectic grains were treated the

same. For each quenched sample, the number of pre-quench eutectic grains per unit area (N_A) and the average diameter of the eutectic grains in 2D ($D_{cir.}$) were measured, and as discussed in section 2.2.1.2, the corresponding values in 3D, i.e. N_V and $D_{sph.}$, were calculated. **Table 2.5** presents one measured N_V and D_{sph} for each experimental condition along with the calculated solid fraction from CCA. The reported uncertainties for f_s were estimated by approximating the "zero curve" with a polynomial. For N_V and $D_{sph.}$ the reported uncertainties were based on estimates of the measurement errors originating from distinguishing the boundaries of impinged eutectic grains.

Table 2.5 Experimentally measured parameters and calculated fraction solid for quenched samples listed in Table 2.3.

Sample	Quench time* (s)	f_s	$D_{sph.}$ (μm)	N_v $\times 10^{11}$ (m^{-3})
1	9	0.59±0.05	96±10	2.1±0.2
2	11	0.60±0.05	101±10	1.7±0.2
3	17	0.58±0.05	103±10	1.9±0.2
4	28	0.60±0.05	163±10	0.9±0.1
5	32	0.58±0.05	141±10	1.3±0.2
6	41	0.58±0.05	168±10	1.0±0.1

* Time after the start of eutectic

As shown in **Table 2.5**, the solidification rate (solid fraction divided by quench time) decreases from sample 1 to 6 as the sample diameter increases and the forced air cooling decreases. Analyzing the measured temperature history for each sample shows that the average temperature during the majority of eutectic transformation increased from samples 1 to 6. Thus, as expected, higher solidification rates result in larger undercooling.

Despite the difference in quench times, the dependence of growth velocity on undercooling can be inferred by approximating the growth velocity as average eutectic radius divided by quench time. From sample 1 to 6, the average growth velocity decreases from 11

to 4 μm/s confirming that higher growth velocity is achieved with larger undercooling. The density of eutectic grains directly depends on the maximum undercooling prior to quenching. Although the average undercooling decreased from samples 1 to 6, the maximum undercooling achieved was somewhat arbitrary. As seen in **Figure 2.13**, the maximum undercooling of sample 3 is larger than that in sample 2 and the maximum undercoolings in samples 5 and 6 are larger than that experienced in sample 4.

2.2.3.2 Inverse analysis

Using the measured values of f_s, N_V, and $D_{sph.}$, the inverse analysis technique described in section **2.2.2.2** was employed to calculate β_1, β_2, and β_3 for each sample. Starting with $\beta_1^0=4\times10^{10}\ m^{-3}K^{-\beta2}$, $\beta_2^0=2.3$, and $\beta_3^0=8\times10^{-7}\ m\ s^{-1}K^{-2}$, the incremental coefficient matrix ($\Delta\beta_q$) was calculated for each sample until a converged solution was achieved. Due to the non-linear response of the CA model, the initial guess must be realistic to enable a converged solution to be determined. For the current analysis, it was straightforward to determine realistic β^0 values. β_1^0 was estimated by relating the average measured N_V to the average of the maximum undercooling before quenching for the different experimental conditions. β_2^0 was assumed to be near 2 based on conventional Oldfield theory. β_3^0 was roughly estimated by relating the average undercooling before quenching to the measured $D_{sph.}$. It was found that for $\beta_1^0=1\times10^{10}$ to $4\times10^{10}\ m^{-3}K^{-\beta2}$, $\beta_2^0=1$ to 3, and $\beta_3^0=3\times10^{-7}$ to $8\times10^{-7}\ m\ s^{-1}K^{-2}$ the final solution is affected by only ±5%. For initial values outside these ranges, the solution does not converge.

Another factor to consider due to the non-linearity of the CA model is defining a limit for β_q increments, i.e. increments in β_q were limited to ensure that a prescribed maximum increment value ($|\Delta\beta_q^{lim}|$) was not exceeded. Another important consideration was ensuring

that the calculated values $\Delta\beta_1$ and $\Delta\beta_2$ translated to the addition (or subtraction) of at least one grain nucleus from the domain for the next iteration. Otherwise, the determinant of the sensitivity matrix is zero and Equation **2-18** cannot be solved. Therefore, it was determined that:

$$\left|\Delta\beta_1\right|^{\min} = \frac{1}{V_\Omega \Delta T_{\max}^{\beta_2}} \qquad \textbf{Equation 2-19}$$

$$\left|\Delta\beta_2\right|^{\min} = \frac{1}{V_\Omega \beta_1 \Delta T_{\max}^{\beta_2} \ln(\Delta T_{\max})} \qquad \textbf{Equation 2-20}$$

where V_Ω is the volume of the computational domain and ΔT_{max} is the maximum undercooling during eutectic solidification. The calculated increment in **Equation** 2-17 for $\Delta\beta_q>0$ is then modified as:

$$\Delta\beta_q^* = \min\left(\Delta\beta_q^{\lim}, \left[\frac{\Delta\beta_q}{\left|\Delta\beta_q\right|^{\min}} + 0.5\right]_{\text{int}} \left|\Delta\beta_q\right|^{\min}\right) \qquad \textbf{Equation 2-21}$$

For $\Delta\beta_q<0$, **Equation 2-21** is revised to return the maximum quantity. Using this modification, inverse analysis was used to predict the microstructural nucleation and growth parameters for samples 1, 3, 4, and 6. Samples 2 and 5 were excluded from this analysis to reserve data to test the forward prediction capability of the model. The residual function (**Equation 2-13**) calculated for each sample during this analysis, shown in **Figure 2.20**, monotonically decreases. This plot shows the progression of microstructure model towards correctly predicting the evolution of eutectic solidification. Since a constant value of $|\Delta\beta_q^{lim}|$ was used for all samples, the number of iterations required for convergence increases as the grain density increases. The calculated values of β_q, listed in **Table 2.6**, are consistent across the different experimental conditions. The deviations observed for the different experimental

conditions are due to the uncertainties associated with the measurement of f_s, N_V, and $D_{sph.}$ that affect the solution of the inverse algorithm. The overall solidification time and calculated values of f_s and N_V at the quenching time, listed in **Table 2.7**, are in good agreement with the experimental data (refer to **Table 2.5**). However, the calculated and measured $D_{sph.}$ show some discrepancies. Since f_s, N_V, and $D_{sph.}$ are linked parameters, the differences in $D_{sph.}$ may be related to uncertainties in measuring $D_{sph.}$ through metallography, i.e. measurement of $D_{sph.}$ is not as accurate as the measurement of f_s and N_V. The inaccuracies in the $D_{sph.}$ measurements are related to: i) the assumption of a spherical eutectic grain envelope when it may not be spherical, and ii) measuring the equivalent diameter of an impinged eutectic grain (impinged with primary phase or other eutectic grains) due to difficulties in distinguishing the boundaries.

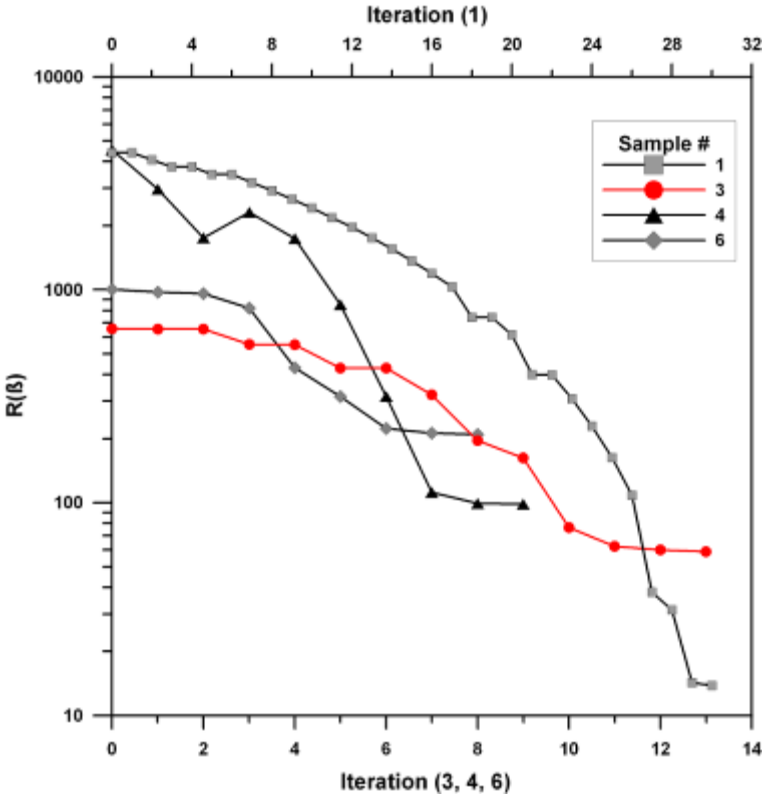

Figure 2.20 Variation of residuals (Equation 2-13) for samples 1, 3, 4, and 6.

Table 2.6 Obtained parameters through employing the inverse algorithm

Sample	Nucleation coefficient, β_1 $\times 10^{10}$ ($m^{-3} K^{-\beta 2}$)	Nucleation power, β_2	Growth coefficient, β_3 $\times 10^{-7}$ ($m\ s^{-1} K^{-2}$)
1	2.03	1.64	5.54
3	1.70	1.60	5.64
4	1.82	1.68	6.44
6	2.16	1.59	6.79

Table 2.7 Calculated parameters using β_q values in Table 2.6.

Sample	Quench time* (s)	f_s	D_{sph} (μm)	N_v $\times 10^{11}$ (m^{-3})
1	9	0.63	103.2	2.12
3	17	0.61	118.4	1.92
4	28	0.61	143.1	0.82
6	41	0.59	141.9	0.95

* Time after the start of eutectic

The evolution of the eutectic microstructure for sample 6 is shown in **Figure 2.21** at three stages during solidification corresponding to solid fractions of 0.54, 0.70 and 0.86. In the 3D maps, the primary phase is white, the remaining liquid has been removed, and the colored phase represents the eutectic phase with different colors for each index factor i.e. each grain. The influence of applying periodic boundary condition is observed in simulated microstructures, i.e. when one grain exits from one face, it enters from the opposite face. The final predicted microstructures for samples 1, 3 and 6 are shown in **Figure 2.22**. The predicted microstructures for samples 1 to 6 show that the scale of both the primary phase and the eutectic phase coarsen with decreasing cooling rate. The advantage of the present model apart from its accuracy in predicting the density and velocity of growing eutectic grains is that it provides a realistic 3D geometry of eutectic grain evolution. Obtained microstructures will be used for characterizing the permeability during equiaxed eutectic solidification.

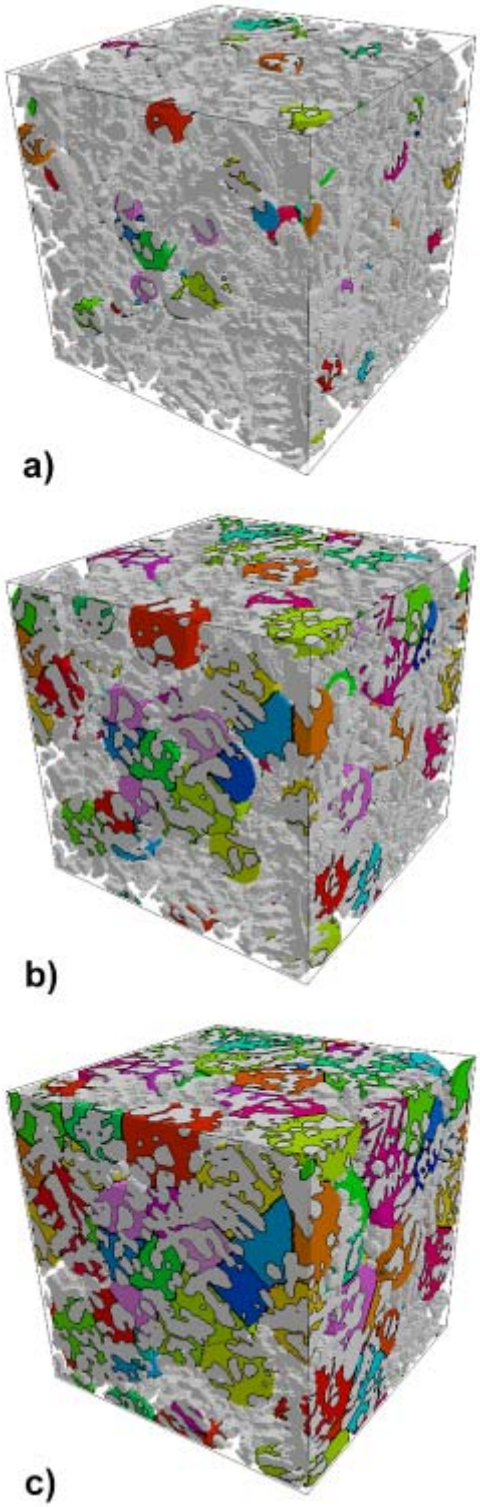

Figure 2.21 Predicted microstructure of sample 6 at solid fraction of a) 0.54, b) 0.70, and c) 0.86. The cube edge length is 1 mm.

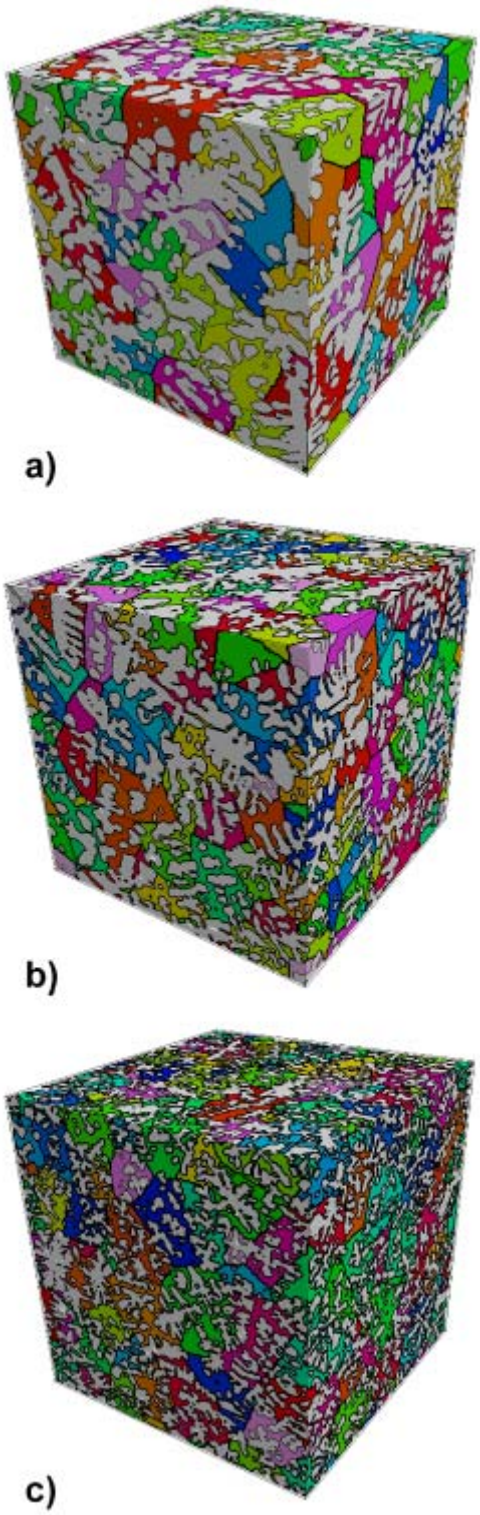

Figure 2.22 Predicted solidified microstructure of sample a) 6, b) 3, and c) 1. The cube edge length is 1 mm.

2.2.3.3 Domain size sensitivity

The size of computational domain must be carefully selected to ensure that the microstructure predictions are numerically independent. The computational domain needs to be large enough to contain a representative volume of microstructure, but no larger than necessary in order to limit computation time. To determine an appropriate size for the current problem, the inverse model was applied with computational domains of different sizes. Keeping a constant cubic cell size of 5.55 μm, the inverse calculation of the β_q parameters was performed on computational domain volumes of $N \times N \times N$ cells with N varying from 60 to 180. **Figure 2.23** shows the variation of calculated (converged) β_q parameters as a function of N for samples 1, 3 and 6. For samples 1 and 3, the β_q parameter solutions stabilize at N equal to *120*. However, stable behavior for sample 6 is not reach until N *is* equal to *140*. Based on the eutectic grain density reported in **Table 2.7**, the sensitivity to computational domain volume indicates that a minimum of ~50 eutectic grains is required in the computational domain in order to reliably calculate the β_q parameters.

2.2.3.4 Application of nucleation and growth relationships

The average values of the β_q parameters obtained via the inverse analysis (**Table 2.6**) have been used to predict the eutectic phase evolution in samples 2 and 5. The data for these samples was not considered during the inverse analysis to determine the β_q parameters. Thus, this forward calculation is meant to validate the predicted β_q. **Table 2.8** shows the calculated f_s, N_V, and D_{sph} at the different quench times employed with samples 2 and 5. The predicted microstructural information is in good agreement with the measurements (refer to **Table 2.5**), which confirms the accuracy of the β_q parameters and the validity of the technique used to calculate them.

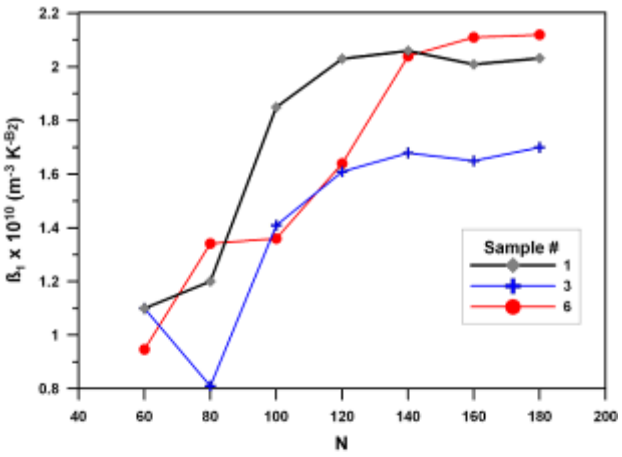

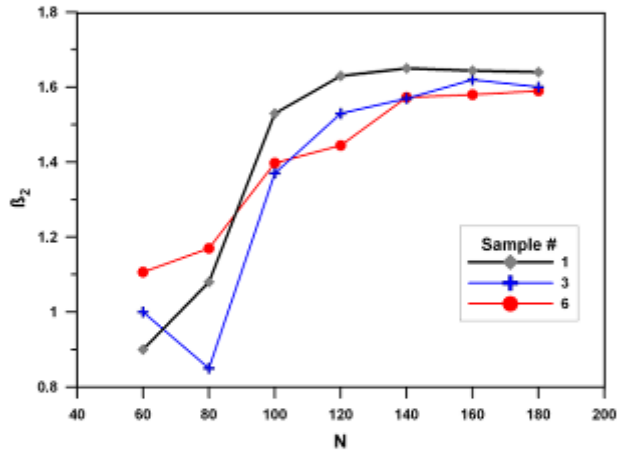

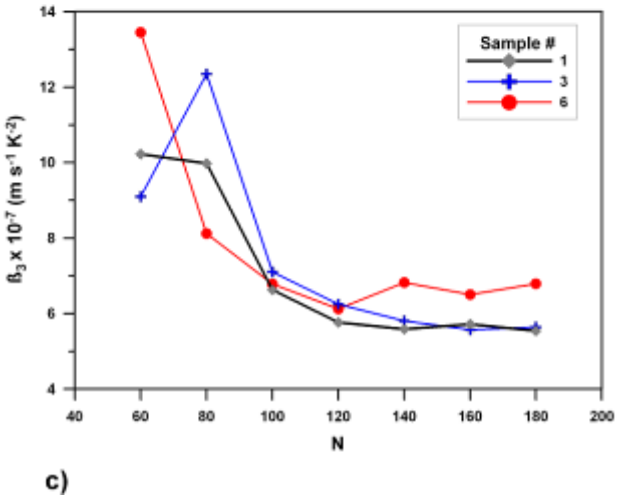

Figure 2.23 Evolution of the calculated β_q parameters as a function of computational domain size with $N \times N \times N$ cubic cells of 5.55 µm.

Table 2.8 Calculated parameters using the average of β_q values in Table 2.6.

Sample	Quench time* (s)	f_s	$D_{sph.}$ (μm)	N_v $\times 10^{11}$ (m^{-3})
2	11	0.63	114.6	1.89
5	32	0.66	128.6	1.26

* Time after the start of eutectic

Since all samples were cast from the same melt, the composition and impurity levels are assumed to be the same and hence, the nucleation and growth kinetics parameters are relevant for all the samples. It would be necessary to re-characterize β_1 and β_2 values to analyze castings made from the same alloy with different levels of impurities. Although for the range of cooling rates studied in this investigation, the growth constant (β_3) was constant, it may vary over a wider range of cooling rates. The benefit of this characterization technique, apart from its applicability to multicomponent alloy systems, is that it provides a straightforward technique to extract the necessary physical parameters for a deterministic microstructure model from basic experimental measurements.

2.3 Summary

In this chapter, the evolution of microstructure during solidification of hypoeutectic aluminum alloys was characterized i) experimentally with the aid of XMT analysis of primary dendritic phase for different Al-Cu alloy samples solidified with different cooling rates, and ii) numerically by simulating the nucleation and growth of eutectic grains on XMT characterized map of primary phase.

Experimentally characterized dendritic microstructures were analyzed to accurately determine the evolution of the microstructural length scale (either d_2 or S_v^{-1}) during solidification. From analyzing the evolution of Al-4.5wt%Cu alloy microstructure, it was

found that S_v^{-1} is proportional to d_2 and can be related to the cube root of time spent in the mushy zone.

The numerical approach presented for characterizing equiaxed eutectic solidification of hypoeutectic Al-Cu alloys provides a novel technique to determine the necessary physical parameters for deterministic microstructure model of multicomponent alloys. Moreover, it provides a realistic 3D microstructure

Obtained 3D geometries from analyzing the equiaxed dendritic solidification of primary phase and the equiaxed eutectic solidification of hypoeutectic Al-Cu alloys are used to for subsequent permeability determination.

3 Physical and Numerical Characterization of Permeability[1]

As discussed in the first chapter, permeability can be characterized using a conventional permeameter for measuring the permeability during the solidification of primary phase not withstanding the expected experimental error. However, this technique is not applicable for measuring the permeability during eutectic solidification. Numerical calculation of permeability, on the other hand, can resolve these limitations. However, careful attention must be paid to accurately formulating the analysis when numerically determining permeability. While the precision of most CFD commercial packages have been tested through comparisons with analytical solutions to standard problems, the application of these packages to real world flow problems lacks extensive validation (i.e. to address whether the model itself is a good representation of the physics of the problem).

In this chapter, the permeability of hypoeutectic aluminum alloys for the complete solidification range are determined both experimentally and numerically using the microstructures that were characterized in Chapter 2. The 3D characterization techniques employed in this study make it is possible to distinguish between liquid regions encapsulated by the solid network, which may occur at high solid fractions, that do not contribute to interdendritic flow and those linked to the source of liquid metal that contribute to

[1] A version of this chapter has been published in:

- Khajeh E, Maijer DM, "Physical and numerical characterization of the near-eutectic permeability of Al-Cu alloys", Acta Materialia, (2010) 58, pp. 6334-6344.
- Khajeh E, Maijer DM, "Permeability of dual structured hypoeutectic aluminum alloys", Acta Materialia, (2011) 59, pp. 4511-4524.
- Khajeh E, Maijer DM, "Numerical determination of permeability of Al-Cu alloys using 3D geometry from X-ray microtomography", Mat Sci Technol, (2010) 26, pp. 1469-1476.

interdendritic flow. Additionally, a new experimental methodology is introduced that represents an alternative technique to determine permeability that does not suffer from the errors associated with microstructural coarsening occurring in conventional permeameters.

3.1 The near-eutectic permeability of Al-Cu alloys

The near-eutectic permeability of aluminum–copper alloys has been determined through physical and numerical modeling using the characterized geometries discussed in section 2.1.1. Representative domains of the microstructure ($1\times1\times1$ mm^3) were extracted from each scan for use in the permeability characterization techniques.

3.1.1 Numerical model

The permeability has been determined numerically by solving the full incompressible Navier-Stokes and continuity equations. The local pressure and velocity distributions in the domain are calculated by solving:

$$\rho\left(\frac{\partial v}{\partial t} + v\cdot\nabla v\right) = -\nabla p + \mu\nabla^2 v \qquad \textbf{Equation 3-1}$$

$$\nabla\cdot v = 0 \qquad \textbf{Equation 3-2}$$

where p and v are the local pressure and velocity in the computational domain, ρ is the interdendritic liquid density and μ is the viscosity. The permeability tensor for the cubic domain has been sequentially calculated by applying a flow with low Reynolds number in the directions normal to each face. By computing the pressure drop (ΔP) and discharge velocity (q) over the length of the domain (L), in the direction of flow, each component of the permeability tensor may be calculated using Darcy's Law:

$$K = \frac{q\mu L}{\Delta P} \qquad \textbf{Equation 3-3}$$

The flow has been solved using a 2^{nd}-order accurate Finite Volume Method (FVM) approach with the commercial CFD software, ANSYS CFX (CFX is a trademark of ANSYS, Inc., USA). The boundary conditions for this analysis are a low Reynolds number velocity inlet (*Re* equal to *0.1*), total pressure outlet (*0 Pa*), free-slip condition on the outer walls and no-slip conditions on the walls representing the solid/liquid interface. The effect of using a free-slip boundary condition for the later boundary condition has been assessed. In order to prevent the formation of dead zones and unexpected flow directions at the inlet and outlet, two thin layers of liquid (5% of the domain length) were added to the inlet and outlet (as in [23]).

Two types of control volumes have been used to describe the interdendritic liquid geometry: uniform hexahedra and unstructured tetrahedra. Cubic hexahedral mesh was generated directly from the 3D voxels of the binarised (0 for the eutectic and 1 the primary) XMT images with the coordinate of each voxel at the center of a cube. A different procedure was developed to generate the unstructured tetrahedral meshes. First, an isosurface representing the solid/liquid interface was needed. A Marching Cube approach was used to convert the voxel-based 3D geometry to a general surface-based format using the visualization software, AMIRA (AMIRA is a trademark of TGS template graphics software, Inc.). Since the number of resulting triangles was very high (more than 25 million for the original image of 540^3 voxels), a smoothing procedure was employed to combine low angle adjacent triangles. The resulting geometries had less than 1.5 million triangles and less than a 2% volume and 8% area difference compared to the initial triangulated geometry. The corresponding geometries were then meshed using the Octree algorithm in ANSYS ICEM CFD (ICEM CFD is a trademark used by ANSYS, Inc. under License.), a commercial

preprocessing software. The unstructured mesh had 4-5 million tetrahedral cells with a minimum quality factor of 0.3 (quality factor is the aspect ratio of the tetrahedral elements). For most geometries, a quality factor greater than 0.3 is essential; while a ratio of 0.15 for complicated geometries is usually sufficient [90]. **Figure 3.1** shows the stages of generating an unstructured mesh on a 2D sample.

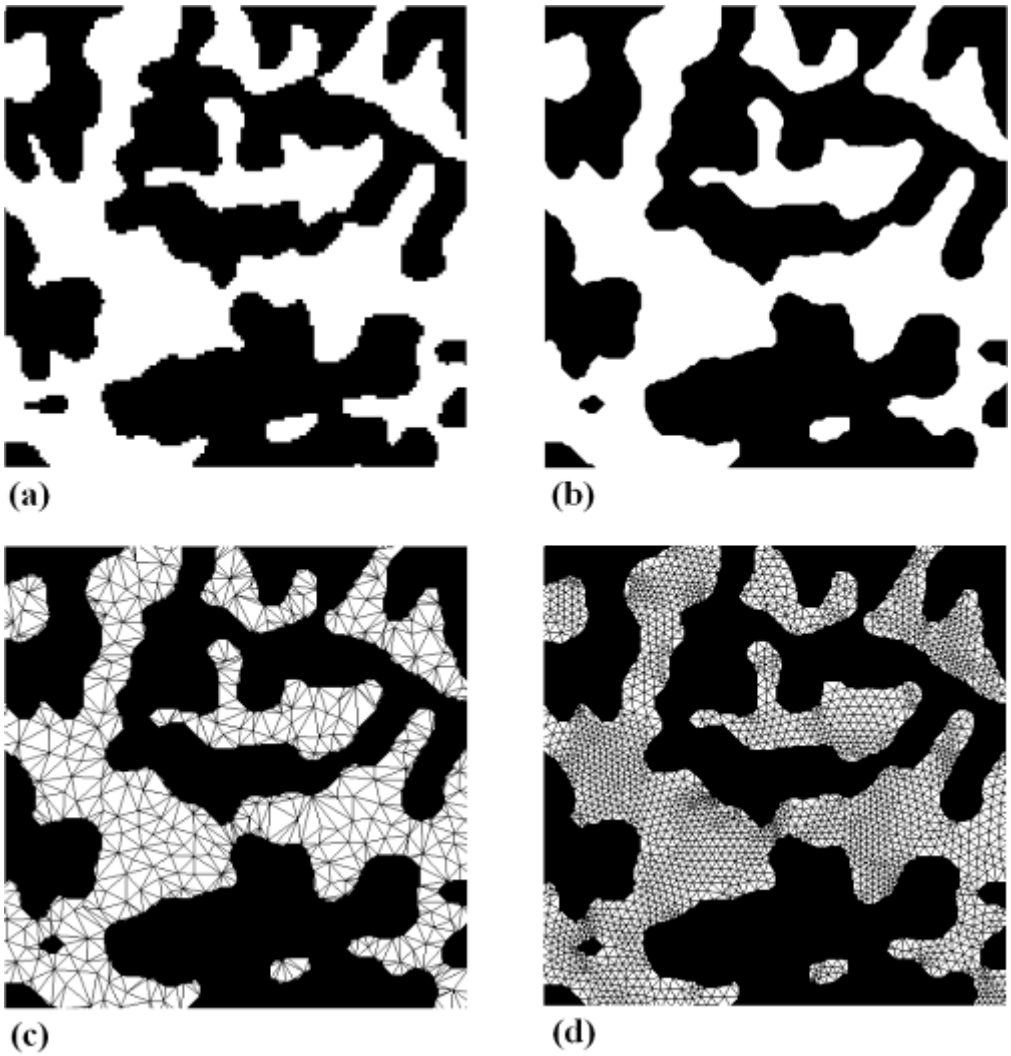

Figure 3.1 (a) 2D section of Al–19wt%Cu (30 mm) microstructure from original voxel based geometry, (b) Marching square (2D equivalent of Marching–Cube) transformation of (a), (c) simplified triangulated surface and (d) final mesh

3.1.2 Physical model

In an effort to avoid the experimental difficulties associated with the direct measurement of permeability in the mushy zone, a physical modeling approach has been developed. The representative domains of the microstructure (1x1x1 mm^3) extracted from each XMT scan were used to construct scaled replicas of the primary Al phase using a rapid prototyping technique. Replicas were then used for permeability measurement.

3.1.2.1 Rapid Prototyping (RP)

The rapid prototyping technique utilizes geometric information generated from either a solid modeling package or a three-dimensional object scan to drive a computer-controlled machine that either mills away unwanted portions of a solid or builds-up material layer-by-layer to create a three dimensional object. For this purpose, the simplified triangulated geometries (refer to **Figure 3.1c**) were used.

The corresponding geometries were scaled by a factor of 50 and used to construct scaled physical models via the Selective Laser Sintering (SLS) rapid prototyping technique. In this process, a high intensity laser selectively fuses polyamide particles on a layer-by-layer basis by tracing cross-sections generated from the surface-based description of the part onto the surface of a powder bed. After each slice is completed, the powder bed is lowered by one layer thickness, a new layer of polyamide powder is applied on top, and the fusing process is repeated until the part is completed. Uncured material is then removed by brushing off the part or flushing interior cavities with forced air. In this study, parts were also cleaned in an ultrasonic bath for 30 min in an attempt to ensure complete removal of all uncured material. The SLS rapid prototype machine (sPro60 HD) used to produce the samples for this study was capable of an accuracy of 0.5 mm, which provided excellent surface resolution and

feature detail. **Figure 3.2** shows an example of the surface-based (triangulated interface) microstructure along with the corresponding scaled replica.

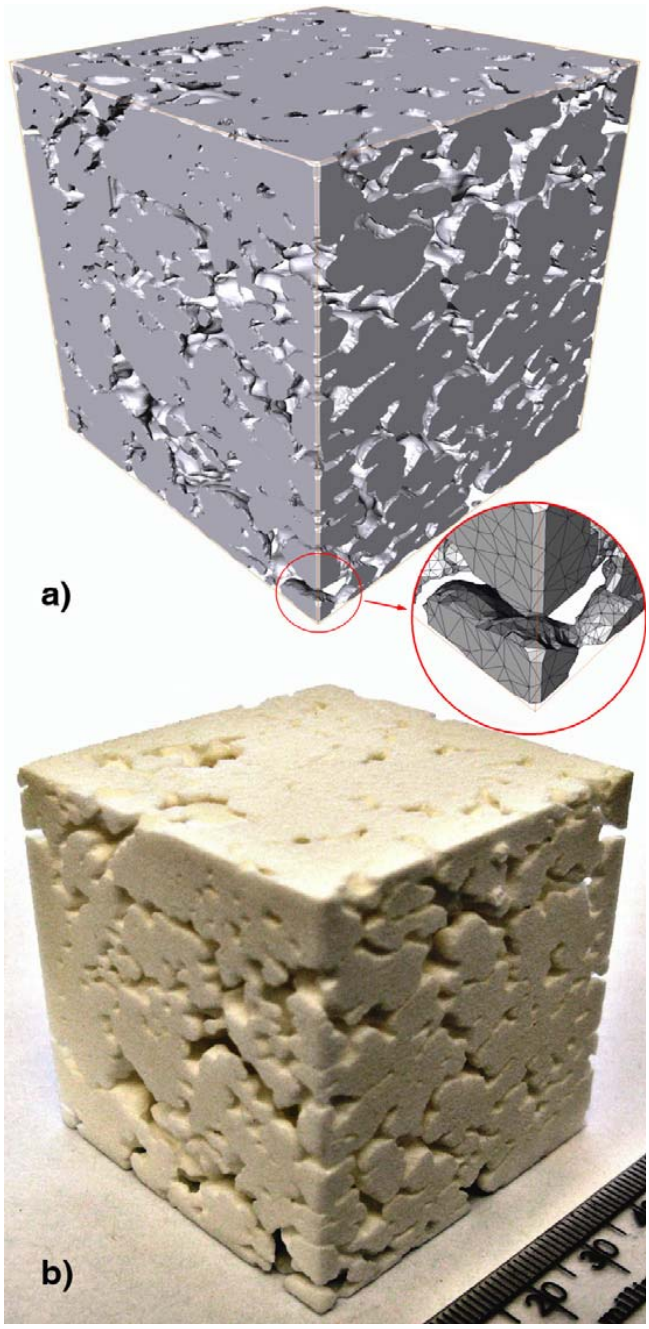

Figure 3.2 (a) Surface-based (triangulated interface) representation of Al-12 wt%Cu, 50 mm from chill, with an edge length of 1 mm; (b) polyamide replica of (a) with an edge length of 50 mm.

3.1.2.2 Permeability measurement

The permeability of each microstructure replica was measured using the purpose-built setup shown in **Figure 3.3**. In this apparatus, a pressure drop is established across the sample to force the working fluid through the sample and the flow rate is measured at steady state. To achieve similitude with the flow conditions ($Re < 1$) occurring in a solidifying alloy, it was necessary to use a liquid with a high viscosity. Two glycerin-based fluids were selected for use in these measurements: laboratory-grade pure glycerin and a solution of 10wt% water in 90wt% glycerin. A 40L, pressurized tank, connected via a 30mm diameter pipe, was used as a fluid reservoir for the apparatus. Due to the low discharge rates of glycerin solution during a measurement and the large diameter of the reservoir tank (~40 cm), the fluid level in the reservoir and the resulting supply pressure were effectively constant during each test.

To adapt the cube-shaped microstructure replicas to the round pipe cross-section, an insert was fabricated from silicone rubber and bonded to the inside of a section of 4" pipe. During a test, a replica was mounted inside the cubic cavity of the holder and the side-surfaces were sealed with silicone gel sealant. To assess whether the working fluid could by-pass the interior of the replica by flowing along the outside surface of the replica and/or along the insert/pipe interface, a leak check was performed with a solid cube. At pressures corresponding to the maximum pressure used during testing, no flow was detected.

Once a replica sample had been loaded and the piping resealed, the following steps were performed during each test:

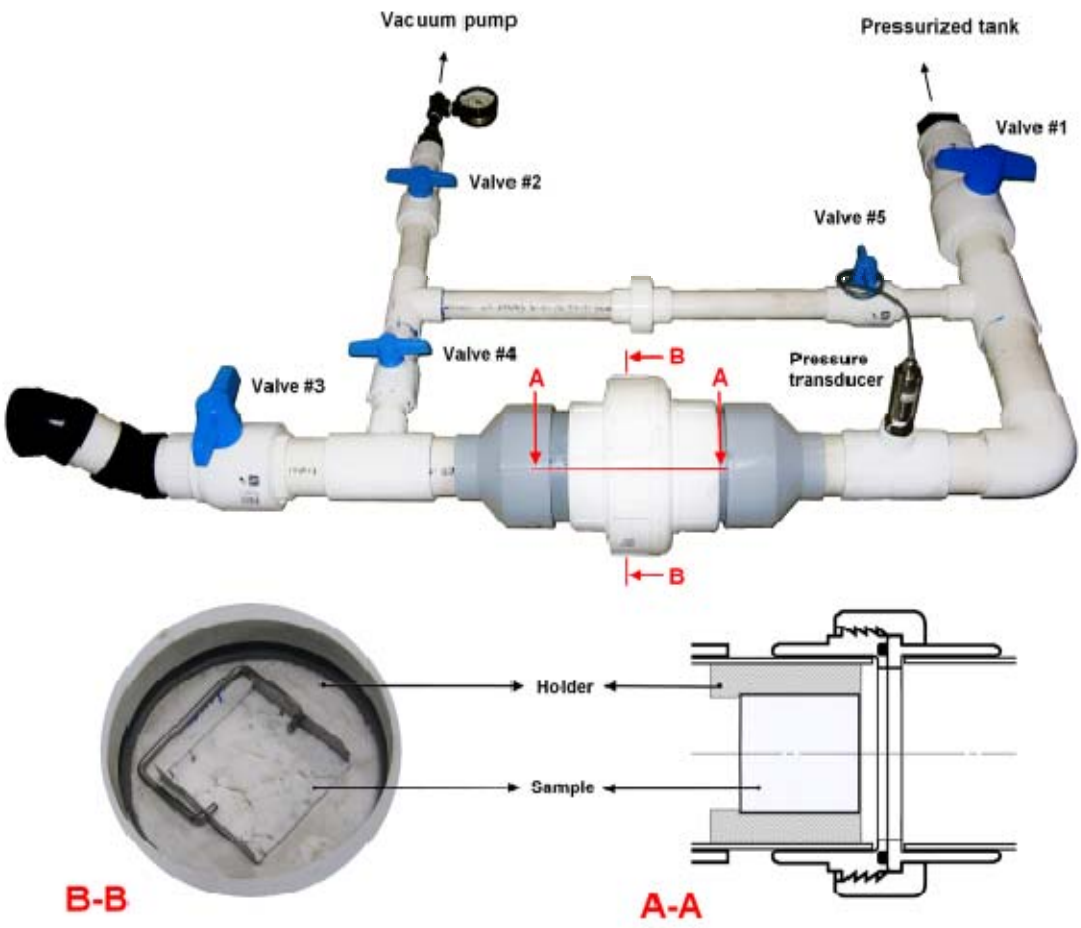

Figure 3.3 Layout of the apparatus built to measure the permeability of replica samples showing the cross-section area surrounding the sample holder (Section A–A) and close-up image of sample inside the holder (Section B–B).

Step 1: Valves #1 and #3 were closed and valves #2, #4 and #5 were opened. A vacuum source, connected on the outlet near valve #2, was activated to extract the air in the system from both sides of the sample. The evacuation continued until a vacuum pressure of -97 kPa was reached.

Step 2: Valves #2 and #3 were closed and valves #1, #4 and #5 were opened. The working fluid entered the system from the fluid reservoir and filled around and into the replica sample from both sides. The vacuum applied during the previous step ensures proper

filling of the system including the replica sample and eliminates the possibility of air bubble formation during filling.

Step 3: Valves #2, #4 and #5 were closed and valves #1 and #3 were opened. Once valve #3 was opened, the outlet pipe of the system (left side of valve #3) filled with liquid. Once steady state flow conditions were achieved, the permeability measurement was performed.

The pressure of the liquid supplied to the apparatus was set at gauge pressure values of up to 200 kPa and was controlled by adjusting the pressure in the fluid reservoir with compressed air. The pressure at the entry of the replica sample, P_{in}, was measured by a calibrated pressure transducer, with an accuracy of ±1.5 kPa. The outlet pressure, P_{out}, was assumed to be equal to atmospheric pressure or a gauge pressure of zero. For each replica sample, the volumetric flow rate, Q, was determined for an applied pressure drop by measuring the time to fill a volume-calibrated container after steady state flow was achieved. The permeability was then calculated using Darcy's Law:

$$\frac{Q}{A} = q = \frac{K}{\mu}\left(\frac{P_{in} - P_{out}}{L}\right) \qquad \textbf{Equation 3-4}$$

where A is the cross-sectional area of the replica sample, q is the superficial velocity, K is the permeability, L is the length of the replica sample, and μ is the viscosity of the fluid. The viscosity of the fluid was measured at the test temperature using a rotational viscometer (Brookfield DV-E viscometer) with an accuracy of ±1% FS.

The permeability tensor was measured by sequentially reorienting the replica sample inside the holder. To assess the consistency of the measurements, 4-10 successive measurements of the flow rate for different applied pressure were performed for each replica sample orientation.

3.1.3 Results and discussion

The non-zero components of the numerically calculated and experimentally measured permeability tensors along with the inverse of the specific surface area (S_v^{-1}), solid fraction and the fraction of isolated liquid regions are summarized in **Table 3.1** for each scaled-replica sample. The K_{zz} component of the permeability tensors is aligned with the direction normal to the chill surface from the experiments (**Figure 2.1**).

Table 3.1 Numerically and physically determined permeabilities of near-eutectic aluminum-copper samples.

Sample #	Alloy (wt%Cu)	Distance from chill (mm)	Solid fraction	Isolated liquid fraction	S_v^{-1} * (mm)	Numerical permeability ($\times 10^{-8}$ m^2)			Physical permeability ($\times 10^{-8}$ m^2)		
						K_{xx}	K_{yy}	K_{zz}	K_{xx}	K_{yy}	K_{zz}
1	10	30	0.807	0.049	2.64	0.54	0.92	0.74	-	-	-
2	10	30	0.840	0.048	2.78	0.13	0.05	0.74	-	-	-
3	10	50	0.840	0.041	3.19	0.54	0.58	0.52	0.32	0.41	0.30
4	12	10	0.832	0.041	2.08	0.37	0.42	0.29	-	-	-
5	12	30	0.815	0.038	2.55	1.85	1.47	0.70	1.37	1.27	0.72
6	12	30	0.828	0.034	2.66	1.15	0.94	0.74	0.90	0.78	0.70
7	12	50	0.792	0.029	3.51	4.51	3.95	3.35	3.66	3.47	3.56
8	15	10	0.666	0.028	1.23	3.09	2.15	2.85	-	-	-
9	15	30	0.677	0.021	1.48	3.39	5.10	4.78	3.04	4.75	4.13
10	15	50	0.650	0.013	2.16	13.50	18.71	10.21	17.41	20.13	11.75
11	19	10	0.552	0.011	1.06	9.51	7.63	12.29	-	-	-
12	19	30	0.581	0.008	1.28	10.73	10.88	19.80	13.17	12.57	14.54
13	19	30	0.586	0.007	1.25	10.14	11.87	13.22	13.04	13.11	15.16
14	19	50	0.571	0.003	1.74	29.27	28.31	14.62	20.20	26.57	17.08
15	25	10	0.283	0.000	0.46	40.64	41.08	41.48	-	-	-
16	25	30	0.292	0.000	0.69	81.10	76.62	65.02	-	-	-
17	25	50	0.301	0.000	0.81	98.53	101.11	108.08	-	-	-

* reported S_v^{-1} is for 50x replica of microstructure

As shown in **Table 3.1**, the absolute values of both the numerically and physically determined permeability increases with decreasing solid fraction and increasing distance from the chill (coarser microstructure). While the numerically calculated permeabilities cover a wide range of solid fractions from 0.28 to 0.84, the experimental measurements are only available for solid fractions above 0.57 due to the fact that at low solid fractions the dendritic

network is incoherent and replication of a cubic specimen was impossible. For most samples, the permeability tensors of these equiaxed microstructures are isotropic. The minor deviations observed are due to the randomness of dendrite locations and anisotropy in the growth pattern of dendrite branches caused by the interaction of neighboring dendrite diffusion fields. For dendritic structures, the unstructured representation of the geometry, originally obtained from a simplified Marching Cube isosurface, provides a better area representation.

3.1.3.1 Assessment of flow conditions

Example plots of the measured superficial velocity multiplied by the viscosity of the working fluid (μq) versus pressure drop ($\Delta P/L$) are presented in **Figure 3.4**. The working fluids were laboratory-grade pure glycerin at 12, 14 and 22°C and a solution of 10wt% water in 90wt% glycerin at 20°C. The viscosities of these fluids, measured via rotational viscometer, were 3.47, 2.21, 1.27 and 0.27 Pa·s, respectively. The plots of $-\partial p/\partial x$ versus μq are linear (R^2 equal to 0.98) indicating that the flow during the permeability measurements was in the Darcian regime. The slope of each line in **Figure 3.4** is the inverse of the permeability (based on **Equation 3-4**). The Reynolds number, calculated as [38]:

$$\mathrm{Re} = \frac{\rho\sqrt{K}q}{\mu} \qquad \textbf{Equation 3-5}$$

is less than 0.05 for each result reported in **Figure 3.4**, as well as the other samples not shown, further justifying the application of **Equation 3-4**.

The predicted pressure distributions used in the numerical calculation of the permeability in the z-direction (K_{zz}) for samples 7 and 14 are shown in **Figure 3.5**. Similar to the

measured permeability analysis, using the predicted pressure gradient and superficial velocity of the fluid, the permeability can be calculated using **Equation 3-4**.

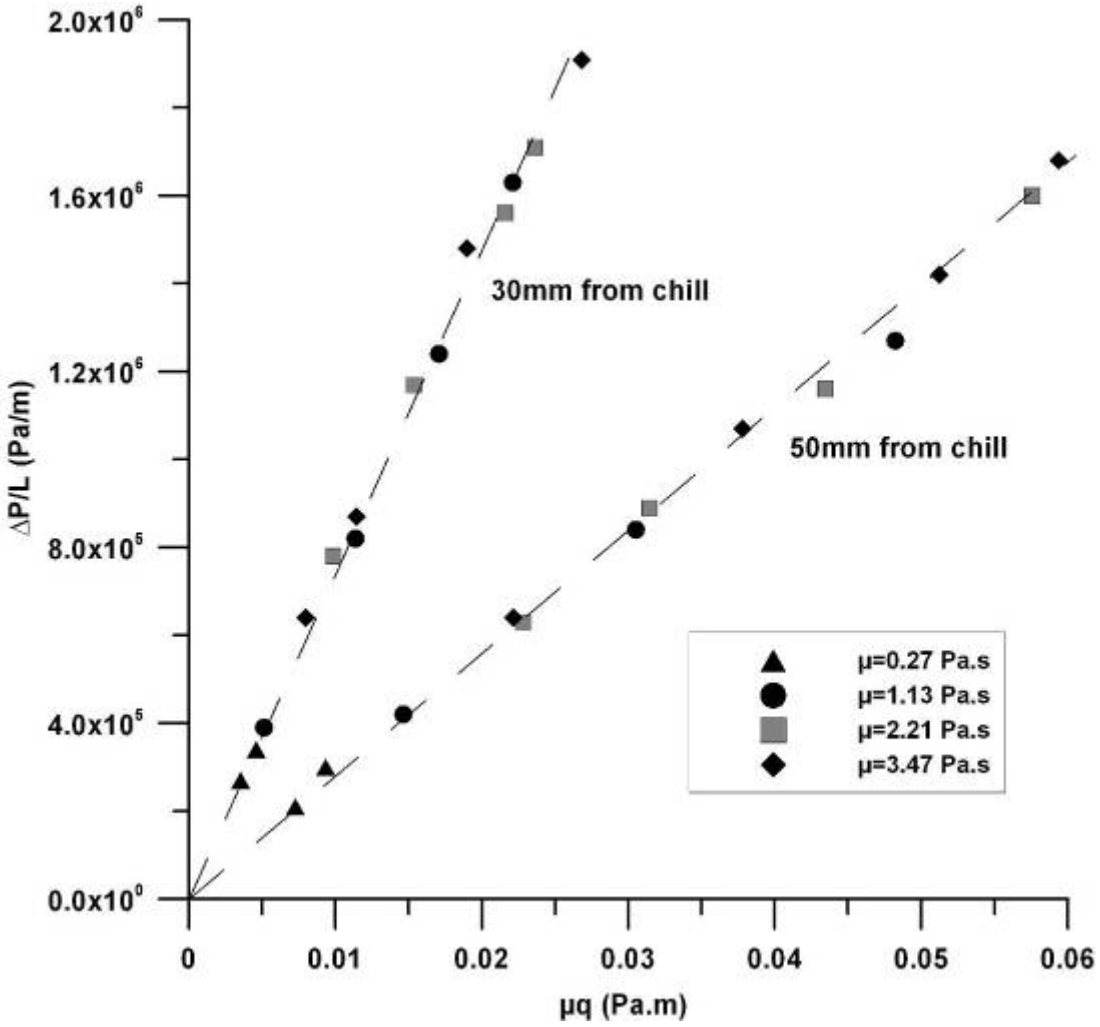

Figure 3.4 Pressure gradient in the x-direction, measured for two replicas of Al–12 wt.% Cu (30 and 50 mm from chill) vs. viscosity multiplied by the superficial velocity. The slope of each line corresponds to the inverse of the permeability resulting in K_{xx} of 1.37×10^{-8} and 3.66×10^{-8} m^2 for samples, 30 and 50 mm from chill (samples #5 and #7 in Table 3.1), respectively.

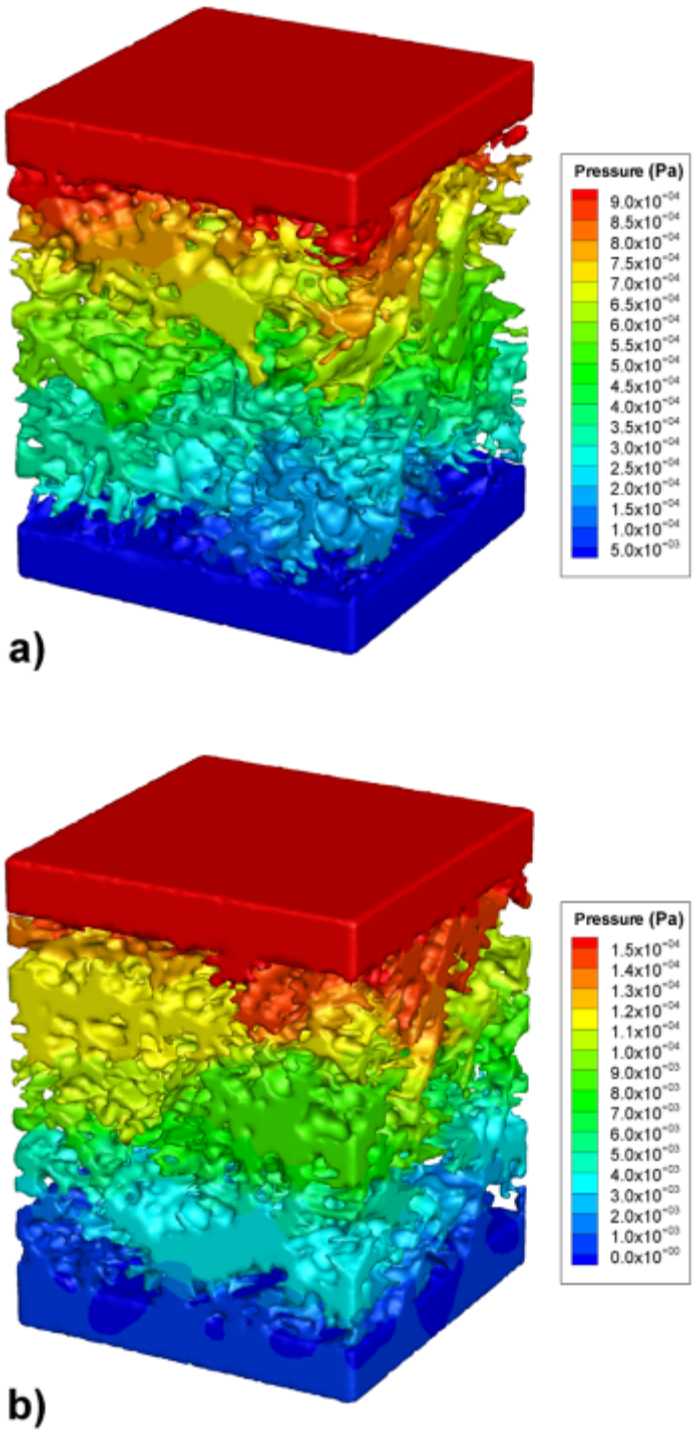

Figure 3.5 Pressure contours for a) Al-12wt%Cu, 50 mm from chill, and b) Al-19wt%Cu, 50 mm from chill. An inlet condition of superficial velocity (q) equal to a) 0.045 m/s and b) 0.032 m/s was applied in z-direction. The calculated pressure drop was a) 9.4×10^4 Pa, and b) 1.5×10^4 Pa resulting in a permeability of a) $K_{zz}=3.35\times10^{-8}$ m^2 (sample #7 in Table 3.1), and b) $K_{zz}=1.46\times10^{-7}$ m^2 (sample #14 in Table 3.1).

3.1.3.2 Comparison of physical and numerical techniques

The numerically calculated permeabilities, as listed in **Table 3.1**, are in good agreement with the permeabilities measured on the scaled replicas. For most samples, the numerically calculated permeabilities were within ±30% of those determined through measurement. Sample 3 is an exception where the numerically calculated permeability was 60% lower than the measured permeability. This sample had the highest solid fraction of the scaled replicas and may have contained residual uncured polyamide powder from the SLS process that was locked in the sample and occluding flow channels. This limitation suggests that replication of microstructures at solid fractions above 0.82 was unreliable. The differences between the numerically calculated and experimentally measured permeabilities, in general, can be attributed to uncertainties in the measurement technique, differences between the boundary conditions applied in the numerical model and those realized in the measurements, and the accuracy of SLS replicas.

Neglecting the uncertainty of sample dimensions, i.e. L and A, the measured variables in the experiments (refer to **Equation 3-4**) were the pressure drop (ΔP), the volumetric flow rate (Q), and the viscosity of the working fluid (μ). By estimating the uncertainty in the measurements of each of these variables, the overall uncertainty of the permeability measurements can be analyzed. The Root Sum Square (RSS) of the estimated uncertainties has been used to calculate the propagated uncertainty as:

$$u_K = \sqrt{(\frac{\partial K}{\partial \Delta P} u_{\Delta P})^2 + (\frac{\partial K}{\partial Q} u_Q)^2 + (\frac{\partial K}{\partial \mu} u_\mu)^2} \qquad \textbf{Equation 3-6}$$

By applying **Equation 3-6** to **Equation 3-4**, u_K is given by:

$$u_K = \frac{L}{A}\sqrt{(\frac{Q\mu}{\Delta P^2} u_{\Delta P})^2 + (\frac{\mu}{\Delta P} u_Q)^2 + (\frac{Q}{\Delta P} u_\mu)^2} \qquad \textbf{Equation 3-7}$$

$u_{\Delta P}$ is the uncertainty of pressure measurement and was equal to ±1500 Pa based on the pressure transducer used in this study. The accuracy of the viscosity measurement, u_{μ}, was equal to ±0.03 Pa s. The volumetric flow rate, Q, was measured based on the time to fill a volume-calibrated container. Neglecting the uncertainty of filling time ($u_t \approx 0$), u_Q can be expressed as:

$$u_Q = \frac{1}{t} u_V \qquad \textbf{Equation 3-8}$$

where u_V is the uncertainty of the container volume and was equal to ±10 cc. Using the elemental uncertainties and **Equation 3-7**, the relative uncertainty for each sample was calculated and found to be in the range of 7-15%.

In addition to the uncertainties inherent in measuring ΔP, Q and μ, the boundary condition applied to the outer walls (free-slip) in the numerical permeability calculations is different than the conditions present in the physical permeability tests. A free-slip boundary condition is more representative of the conditions present when trying to simulate the permeability of the bulk microstructure with a limited computational domain. However, in the measurements conducted for this study, the interface between the scaled replica and its holder acts as a no-slip boundary. Applying a no-slip condition to the outer walls in the numerical model results in a maximum 7% decrease in the calculated permeability compared with the free-slip outer walls predictions.

Another factor causing differences between the numerically calculated and physically measured permeability is the accuracy of SLS replicas. As discussed in section **3.1.2.1**, the minimum accuracy of replication was 0.5 mm. Although median filtering of 5 voxels (equivalent to 0.5mm at the 50x scale) was used to smooth the scanned images, the SLS machine will not be able to accurately reproduce features of sizes equal to the minimum

accuracy leading to growth, shrinkage, or smearing of features in the cured solid which affects the solid fraction and specific surface area.

3.1.3.3 Effect of geometry variability

The influence of sample geometry variation, i.e that caused by sampling variability, on the permeability was studied by comparing results for duplicate sample conditions. Two samples were extracted at the same distance from the chill from castings of three different alloys (sample #'s 1 & 2, 5 & 6, and 12 & 13 in **Table 3.1**). The permeability values for these samples exhibit variability, which is related to the variability in f_s and S_v^{-1}. Thus, samples #12 and #13 show relatively small permeability differences because f_s and S_v^{-1} are similar. However, the large differences in f_s and S_v^{-1} in the other samples (1 & 2 and 5 & 6) result in substantially different permeabilities. This variability may also have been caused by variability in segregation fields, different dendrite density, and disturbances during the XMT scans resulting in different gray-scale levels of existing phases.

3.2 Permeability evolution during equiaxed dendritic solidification

Physical and numerical modeling techniques were employed too characterize the evolution of permeability during equiaxed dendritic solidification of Al-4.5wt%Cu,. The surface-based geometries resulting from the microstructure characterization of each sample (discussed in section **2.1.2**) were used to construct microstructure replicas and to generate computational domains for the physical and numerical determination of permeability, respectively.

3.2.1 Physical determination of permeability

Representative cubic domains with an edge length of 1.11 mm were extracted from each

processed XMT dataset for use in characterizing the permeability. The corresponding surface-based geometry of the dendritic structures were then scaled by a factor of 45 (resulting in cubes with an edge length of 50 mm) and used to construct physical models via the Selective Laser Sintering (SLS) rapid prototyping technique. The SLS rapid prototype machine used to produce the samples for part of the study was capable of an accuracy of 0.15 mm. **Figure 3.6** shows an example of the surface-based (triangulated interface) microstructure along with the corresponding scaled replica. The permeability of each microstructure replica was then measured by passing a working fluid through the physical model and measuring the resulting discharge flow rate and pressure drop.

3.2.2 Numerical determination of permeability

The permeability values of the Al-4.5wt%Cu samples characterized for this study were also determined numerically by solving the full incompressible Navier-Stokes and continuity equations on non-scaled geometries using the physical properties of glycerin. For this purpose, the same procedure as discussed in section **3.1.1** was used.

An example of the predicted pressure distribution used in the calculation of the permeability is shown in **Figure 3.7**. Using the predicted pressure gradient and superficial velocity of the fluid, the permeability was calculated using **Equation 3-4**.

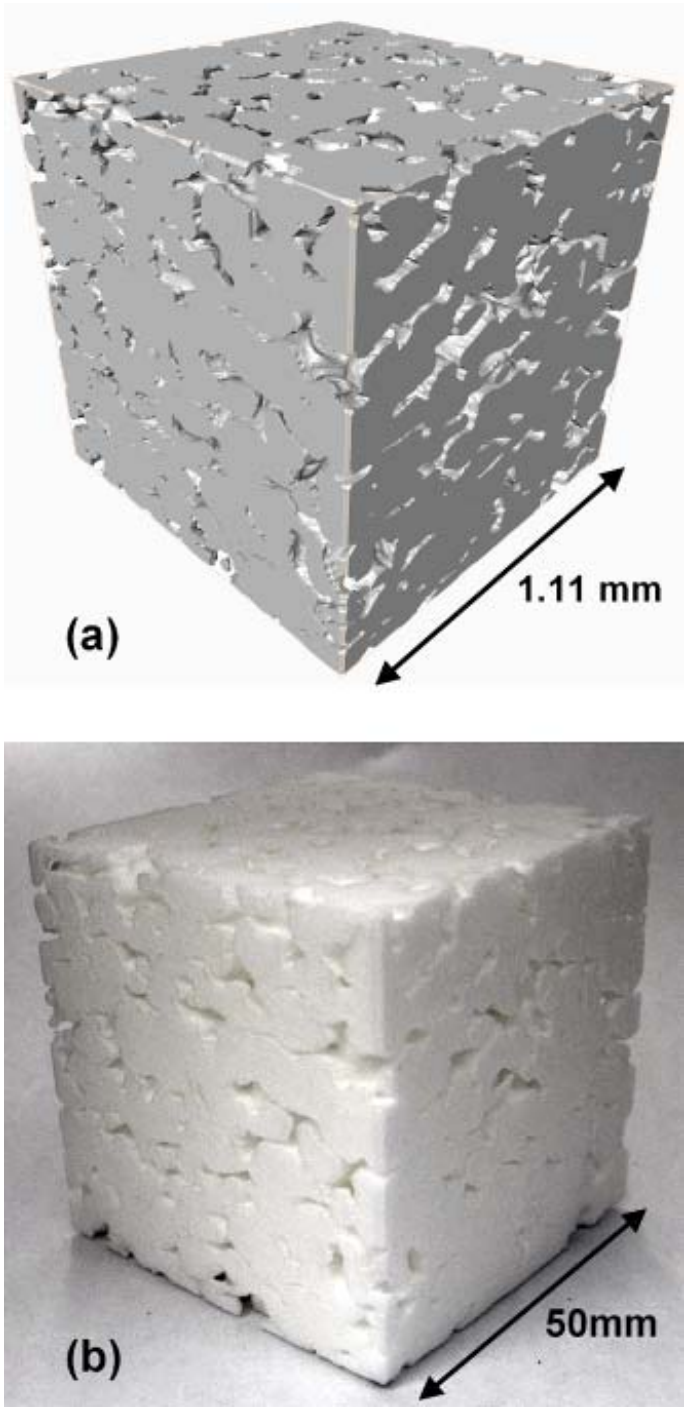

Figure 3.6 (a) Surface-based (triangulated interface) representation of the microstructure of a sample cast with a mold diameter of 29 mm and quenched at 898 K. (b) SLS replica of (a).

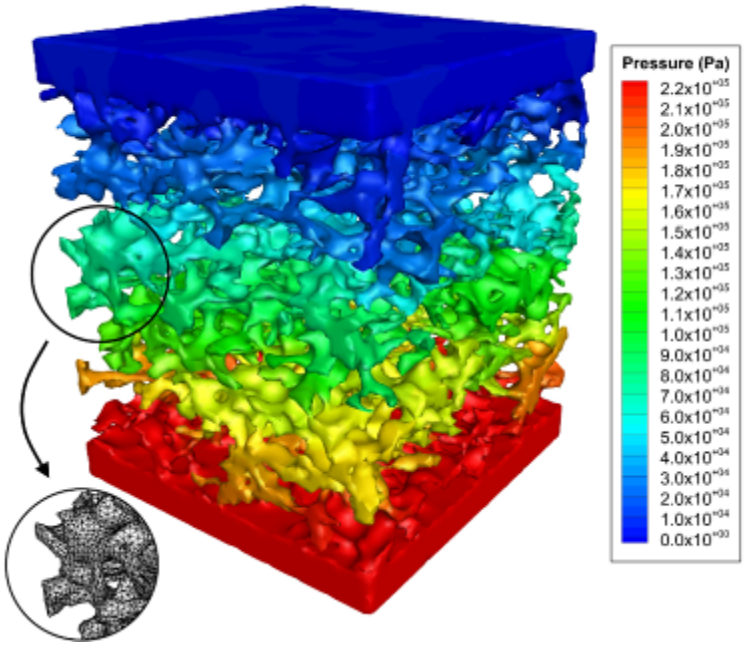

Figure 3.7 Simulated pressure contour for the unstructured mesh of a domain corresponding to a sample cast with a mold diameter of 29 mm and quenched at 898 K. An inlet condition of superficial velocity equal to 1.0 mm/s was applied in the z-direction resulting in a permeability of K_{zz}=6.3×10^{-12} m^2.

3.2.3 Comparison of physical and numerical permeabilities

The numerically calculated and experimentally measured permeability tensors along with the secondary dendrite arm spacing (SDAS), inverse of the specific surface area (S_v^{-1}), and the solid fraction for the samples described in section 2.1.2 are summarized in **Table 3.2**. As shown in **Table 3.2**, the absolute values of both the numerically and physically determined permeability increase with decreasing solid fraction. For most samples, the permeability tensors of these equiaxed microstructures are isotropic. The small variations observed are due to the random variations in the dendritic structure and anisotropy in the growth pattern of dendrite branches caused by the interaction of neighboring dendrite diffusion fields.

Table 3.2 Numerical and physical permeabilities (values are for non-scales microstructure)

Sample #	Mold diameter (mm)	Quench Temp. (K)	Solid fraction	SDAS (μm)	S_v^{-1} (μm)	Numerical permeability ($\times 10^{-11}$ m^2)			Physical permeability ($\times 10^{-11}$ m^2)		
						K_{xx}	K_{yy}	K_{zz}	K_{xx}	K_{yy}	K_{zz}
1	19	915	0.34	26±5	6.39	4.46	4.99	3.40	-	-	-
2	19	913	0.44	28±6	8.41	2.36	2.36	2.89	-	-	-
3	19	910	0.53	39±7	9.76	1.43	1.37	0.92	1.09	0.97	0.70
4	19	905	0.61	48±7	12.12	0.76	1.02	0.74	0.53	0.73	0.51
5	19	902	0.65	49±7	13.18	0.55	0.54	0.54	-	-	-
6	19	883	0.79	59±7	17.07	0.14	0.11	0.12	-	-	-
7	29	915	0.37	41±5	11.62	10.30	11.80	11.12	-	-	-
8	29	913	0.48	53±5	12.83	2.92	2.61	3.81	2.21	2.11	2.91
9	29	910	0.57	58±6	14.59	1.71	1.71	1.96	-	-	-
10	29	903	0.65	68±6	18.02	0.84	1.10	1.08	-	-	-
11	29	898	0.70	70±7	20.52	0.53	0.69	0.63	0.39	0.53	0.48
12	29	893	0.74	71±7	20.18	0.28	0.39	0.34	-	-	-

As listed in **Table 3.2**, the numerically calculated permeabilities are in close agreement with the measured permeabilities (within ±30%). The differences between the numerically calculated and experimentally measured permeabilities, as discussed in section 3.1.3.2 can be attributed to uncertainties in the measurement technique, differences between the boundary conditions applied in the numerical model and those realized in the measurements, and the accuracy of SLS replicas. The cumulative uncertainty of the measured permeabilities from all sources is roughly estimated as ±40%. This is an acceptable uncertainty when compared with conventional permeameter measurements.

3.3 Permeability evolution during equiaxed eutectic solidification

The permeability of the equiaxed dendritic/eutectic structure formed during the solidification of an Al-20wt%Cu alloy has been characterized through physical and numerical modeling. To accomplish this task, the evolution of eutectic grains in an experimentally characterized dendritic structure was first simulated (refer to section **2.2**). A CA model was used to predict the eutectic microstructure that forms for different nucleation densities (N_v equal to 6, 50 and 90 mm^{-3}). The simulated eutectic microstructure for N_v equal

to 50 mm^{-3} is shown in **Figure 3.8** at four stages during solidification corresponding to solid fractions between 0.6 and 0.9. The permeability was then determined through physical and numerical modeling using the predicted geometry of the instantaneous liquid channels, which represents the remaining liquid during eutectic solidification.

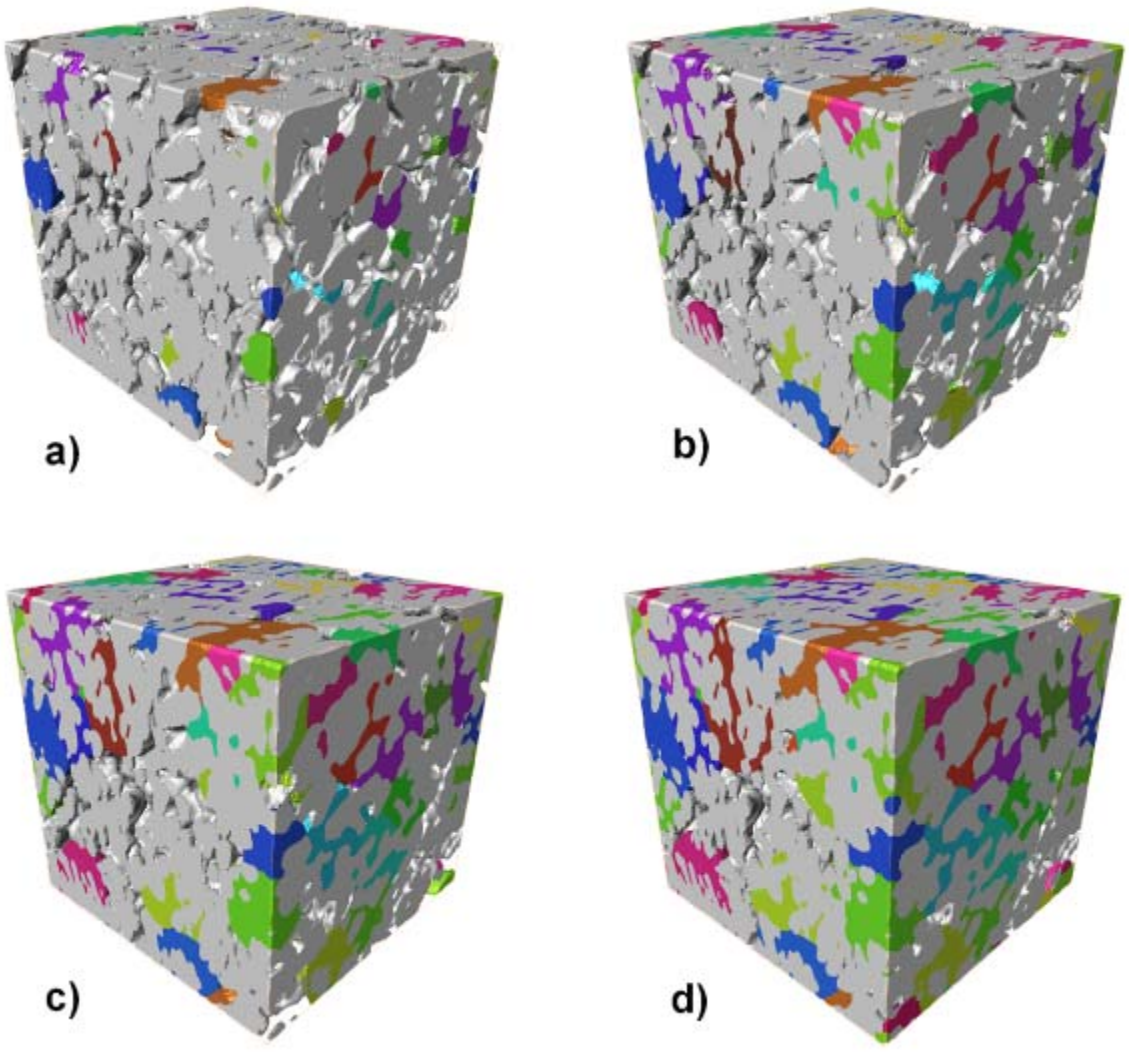

Figure 3.8 Predicted microstructure for Al-20wt%Cu with N_v=50 mm^{-3} at solid fraction of a) 0.6, b) 0.7, c)0.8, and d) 0.9. In the 3D maps, the primary phase is grey, the remaining liquid has been removed, and the colored phase represents the eutectic phase with different colors for each index factor, i.e. each grain. The cube edge length is 1 mm.

3.3.1 Physical determination of permeability

The physical model technique, described in Section **3.1.2**, has been used to measure the permeability of the microstructure during eutectic solidification. Representative microstructures predicted by the CA technique described in Section **2.**2 for N_v equal to 90 mm^{-3} at solid fractions of 0.52, 0.63, 0.73, and 0.83 were used to construct scaled replicas of the solid phase (primary α phase and the solidified eutectic grains).

For this study, the voxel-based simulated microstructures were first manipulated to identify the isosurface representing the solid/liquid interface. The corresponding geometries were then scaled by a factor of 50 and used to construct scaled physical models via Selective Laser Sintering (SLS). The SLS rapid prototype machine used to produce the samples for part of the investigation was capable of an accuracy of 0.15 mm, which provided excellent surface resolution and feature detail. **Figure 3.9** shows an example of the surface-based (triangulated interface) microstructure along with the corresponding scaled replica.

The permeability of each microstructure replica was measured by passing a working fluid through the physical models and measuring the discharge flow rate and pressure drop. The permeability was then calculated using Darcy's Law (refer to **Equation 3-4**) and multiplied by a factor of 50^{-2} to correct the permeability to reflect the unscaled microstructure. Detailed description of the apparatus used in this study and complete instructions of the measurement procedure has been discussed in section 3.1.2.

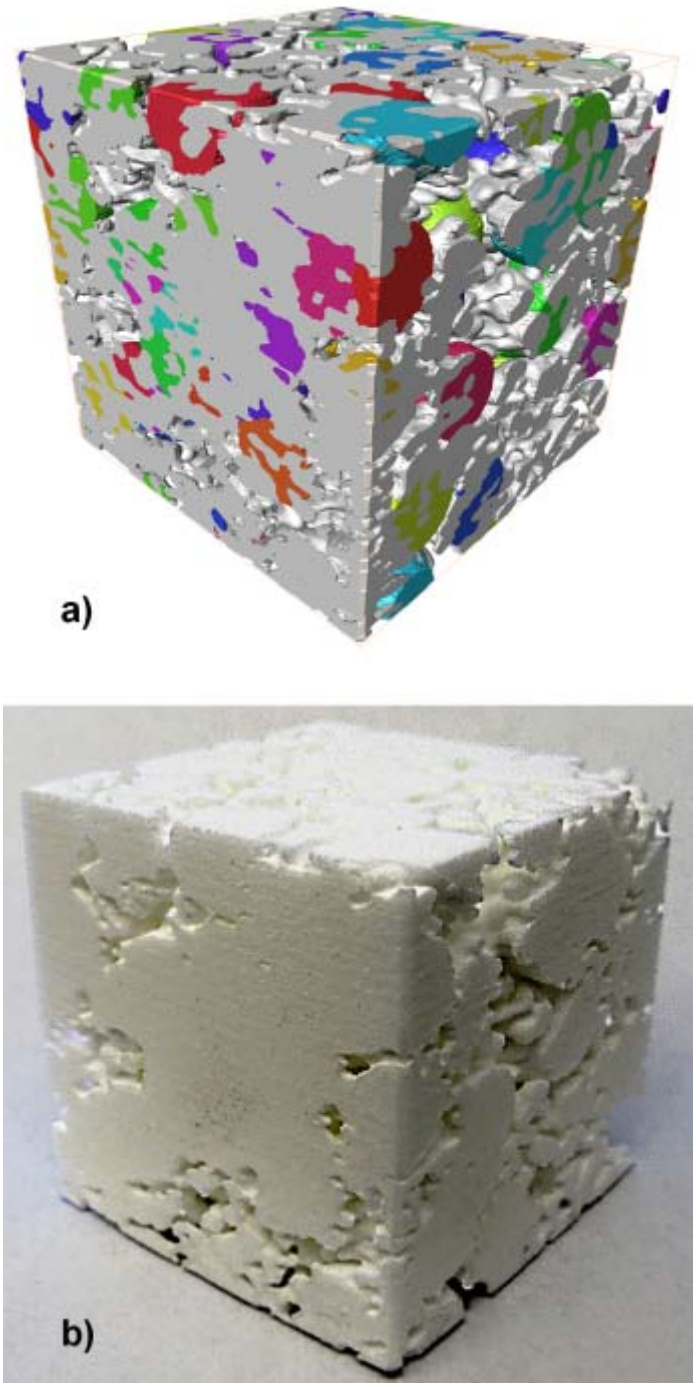

Figure 3.9 (a) Surface-based (triangulated interface) representation of solidifying microstructure for Al-20wt%Cu with N_v=90 mm^{-3} at solid fraction of 0.73, with the edge length of 1 mm and (b) SLS replica of (a) with the edge length of 50 mm.

3.3.2 Numerical determination of permeability

The permeability of the hypoeutectic Al-20wt%Cu alloy during eutectic solidification for N_v equal to 6, 50 and 90 mm^{-3} was determined numerically by solving the full incompressible Navier-Stokes and continuity equations. These simulations were performed on the unscaled geometries of the simulated microstructures using a fluid with the physical properties of glycerin. For this purpose, the same procedure as discussed in section **3.1.1** was used.

An example of the predicted pressure distribution used in the calculation of the permeability is shown in **Figure 3.10**. Using the predicted pressure gradient and superficial velocity of the fluid, the permeability was calculated using **Equation 3-4**.

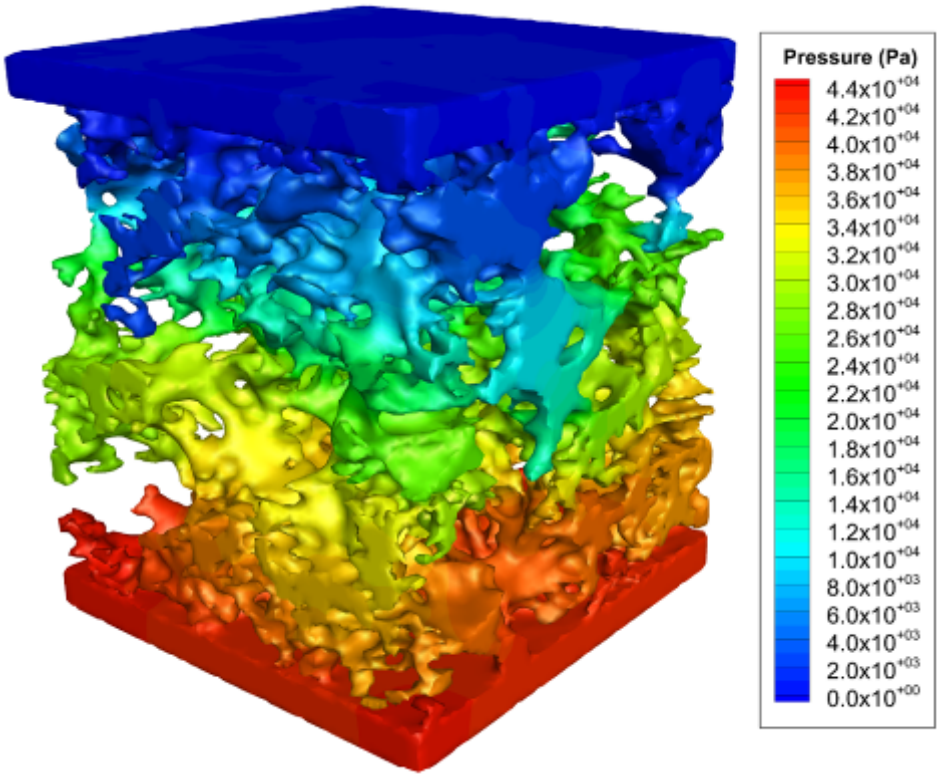

Figure 3.10 Simulated pressure contour for solid sample in Fig. 4 for flow in x-direction. An inlet condition of superficial velocity equal to 1 mm/s was applied in x-direction resulting in a permeability of K_{xx}=2.71×10^{-11} m^2.

3.3.3 Comparison of physical and numerical permeabilities

The non-zero components of the numerically calculated and experimentally measured permeability tensors along with the inverse of the specific surface area (S_v^{-1}) and the effective solid fraction (solid fraction plus the fraction of isolated liquid regions) are summarized in **Table 3.3** for Al-20wt%Cu with a eutectic grain density of N_v equal to 90 mm^{-3}. The absolute values of both the numerically and physically determined permeability increase with decreasing solid fraction. The numerically calculated permeabilities listed in **Table 3.3** are in close agreement with the permeabilities measured on the scaled replicas (within ±30% of those determined through measurement). The differences between the numerically calculated and experimentally measured permeabilities, as discussed in section **3.1.3.2** can be attributed to uncertainties in the measurement technique, differences between the boundary conditions applied in the numerical model and those realized in the measurements, and the accuracy of SLS replicas.

Table 3.3 Numerical and physical permeabilities for Al-20wt%Cu with N_v=90 mm^{-3}. Reported values are for unscaled microstructure.

Sample #	Effective Solid Fraction	S_v^{-1} (µm)	Numerical Permeability ($\times 10^{-11}$ m^2)			Physical Permeability ($\times 10^{-11}$ m^2)		
			K_{xx}	K_{yy}	K_{zz}	K_{xx}	K_{yy}	K_{zz}
1	0.524	25.0	9.84	12.51	10.60	7.96	8.56	9.40
2	0.626	34.8	5.76	6.44	5.96	3.70	4.60	6.39
3	0.732	52.8	2.71	3.72	3.67	2.51	2.47	2.82
4	0.831	87.4	1.76	0.90	1.50	1.22	0.74	1.09
5	0.893	142.4	0.25	0.13	0.80	-	-	-

Comparing the physically and numerically determined permeability, and considering the uncertainties in the techniques used for this study, the results suggests that the numerical modeling technique provides a good representation of the physics of this problem. Thus, this

technique was employed to calculate the evolution of permeability for Al-20wt%Cu with different eutectic grain densities.

3.4 Summary

The permeability tensor for hypoeutectic Al-Cu alloys has been determined for a wide range of solid fractions by conducting measurements on scaled microstructure replicas and numerical modeling. The permeability of the primary, equiaxed, dendritic phase has been characterized using geometries obtained by X-ray microtomographic analysis of near-eutectic Al-Cu alloys and Al-4.5wt%Cu alloy samples quenched at different temperatures after the start of solidification. The permeability during equiaxed eutectic solidification was characterized on simulated dendritic/eutectic microstructures predicted using a Cellular Automaton technique. A glycerin-based working fluid was passed through the scaled replicas and the permeability was calculated from measurements of the discharge flow rate and pressure drop. Mathematical models, considering the continuity and momentum equations, were developed for the corresponding unstructured meshes of the 3D geometries used for the scaled replicas.

Comparison of the numerical and measured permeabilities showed close agreement (within ±30%). Considering the uncertainties in the techniques used for this study, the results suggest that the numerical modeling techniques employed in this study provide a good representation of the physics of this problem. Thus, the numerically characterized permeabilities can be reliably used for investigating the evolution of permeability.

4 Permeability of Equiaxed Dendritic Structures[1]

In addition to quantifying the permeability behavior using numerical and experiemtnal techniques, research continues on determining a comprehensive equation capable of accurately predicting the permeability for use in macroscale models. For equiaxed dendritic solidification, the Carman-Kozeny equation, derived from the solution of the Poiseuille equation, is often used to describe the permeability, K, as [19]:

$$K = \frac{(1-f_s)^3}{k_C S_v^2 f_s^2} \qquad \textbf{Equation 4-1}$$

where f_s is the solid fraction, k_C is a constant, and S_v is the microstructural length scale defined as solid/liquid interfacial area per unit volume of solid. As noted in the literature review presented in Chapter 1, there is still considerable uncertainty regarding appropriate values for S_v and k_C as well as possible links to more practical parameters for use in models of casting processes.

In this chapter, the physically and numerically characterized permeability results for equiaxed dendritic structures (refer to Chapter 3) are put into perspective by comparison with the conventional Carman-Kozeny expression. The validity of this equation will be assessed and the values for S_v and k_C will be linked to more practical parameters available in macroscale solidification models.

[1] A version of this chapter has been published in:

- Khajeh E, Maijer DM, "Physical and numerical characterization of the near-eutectic permeability of Al-Cu alloys", Acta Materialia, (2010) 58, pp. 6334-6344.
- Khajeh E, Maijer DM, "Numerical determination of permeability of Al-Cu alloys using 3D geometry from X-ray microtomography", Mat Sci Technol, (2010) 26, pp. 1469-1476.

4.1 The near-eutectic permeability of Al-Cu alloys

The standard procedure for comparing permeability across different microstructures is to evaluate the dimensionless permeability. In the following sections, the dimensionless permeabilities, i.e. absolute values of permeability normalized with S_v as presented in **Table 3.1** , are analyzed and compared with prediction through Carman-Kozeny expression.

4.1.1 Effect of mesh

Figure 4.1 shows the dimensionless numerically and physically determined permeabilities (average of K_{xx}, K_{yy} and K_{zz}) plotted versus the effective solid fraction for the near-eutectic samples listed in **Table 3.1**. For comparison, the dimensionless permeabilities, calculated with the Carman-Kozeny expression for k_C equal to 1, 3, and 5, have been plotted as lines in **Figure 4.1**. The two data sets (numerical and physical models) from the current study are in good agreement and consistent with the Carman-Kozeny expression for a k_C of 3. The results of Brown et al. [23], who reported dimensionless permeability values as a function of the effective solid fraction, have also been included in **Figure 4.1**. Although Brown et al. [23] corrected for the presence of isolated liquid regions, K and S_v were calculated using uniform cubic meshes of the sample domains. As shown, the dimensionless permeabilities of the current study (unstructured tetrahedral mesh) and those from Brown et al. [23] (uniform cubic mesh) are significantly different. Since the permeability directly depends on the tortuosity of the channels, it is likely that the different representation of the geometry resulting from the different mesh types has led to this discrepancy. To verify this, a uniform cubic mesh was developed for two samples from the current study and used to calculate the dimensionless permeability (both K and S_v). The uniform mesh results are compared with the equivalent unstructured mesh results in **Table 4.1** and **Figure 4.1**. The absolute permeability

is higher for domains with unstructured mesh. Since the permeability depends directly on the tortuosity of the flow channels, using a uniform mesh increases the complexity of the solid/liquid interface and results in increased resistance to flow.

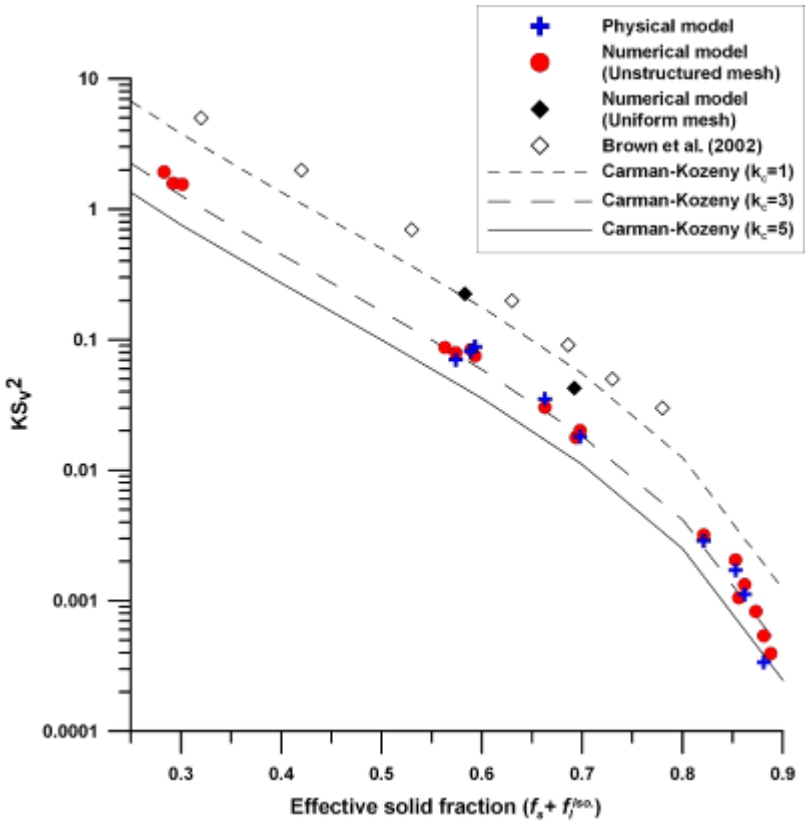

Figure 4.1 Dimensionless permeability versus effective solid fraction. Blue crosses represent measured permeability normalized with S_v obtained from unstructured mesh (data in Table 3.1); Closed (red) circles represent calculated permeability for unstructured mesh geometries with S_v obtained from the mesh (data in Table 3.1); Closed diamonds represent calculated permeability for uniform mesh with S_v obtained from uniform mesh (data in Table 4.1); and open diamonds are results reported by Brown et al. (2002). Lines indicate dimensionless permeability based on the Carman-Kozeny expression with k_C equal to *1*, *3* and *5*.

Table 4.1 Calculated permeability and microstructural length scale for unstructured and uniform meshes.

Sample #	Unstructured tetrahedra			Uniform cubic		
	Effective solid fraction	S_v^{-1} (mm)	K_{xx} ($\times 10^{-8}$ m^2)	Effective solid fraction	S_v^{-1} (mm)	K_{xx} ($\times 10^{-8}$ m^2)
9	0.698	1.48	3.39	0.692	0.69	2.01
13	0.593	1.25	10.14	0.583	0.44	4.46

Figure 4.1 shows that uniform mesh geometries result in higher dimensionless permeabilities than those for an unstructured mesh. Also, as expected the uniform mesh results are closer to the values reported by Brown et al. [23]. Although using techniques like the Marching Cube method to calculate the solid/liquid interfacial area improves the estimation of S_v (refer to **Table 4.1**), the corresponding S_v of the computational domain (uniform mesh) used for the flow solution will be different. Overall, the use of uniform mesh affects both the absolute permeability and the S_v. Thus, the permeability and the S_v calculated on an unstructured mesh provide a better description of the real interdendritic geometry. The agreement between the permeabilities calculated for the unstructured mesh (K and S_v from the unstructured mesh) and those obtained from replica measurements supports this observation.

4.1.2 Comparison with conventional permeameter measurements

Figure 4.2 shows a comparison between the numerically and physically determined dimensionless permeability and various reported results from permeameter experiments [25, 27, 31, 36]. In the available experimental results, the microstructures were analyzed using 2D microscopy and thus the isolated liquid fractions were not quantified nor corrected for. As a result, the permeability results from this investigation have been normalized with S_v and plotted as a function of the solid fraction rather than the effective values of S_v and solid

fraction. As shown, the results of this investigation are situated within the scatter of the experimental data. However, unlike **Figure 4.1**, the Carman-Kozeny expression with a constant k_C does not adequately represent the numerically and physically determined permeabilities at high solid fractions (> 0.7). Thus, the Carman-Kozeny expression with a constant k_C can only reproduce the numerical and physical permeabilities if the effective f_s and S_v^{-1} are used.

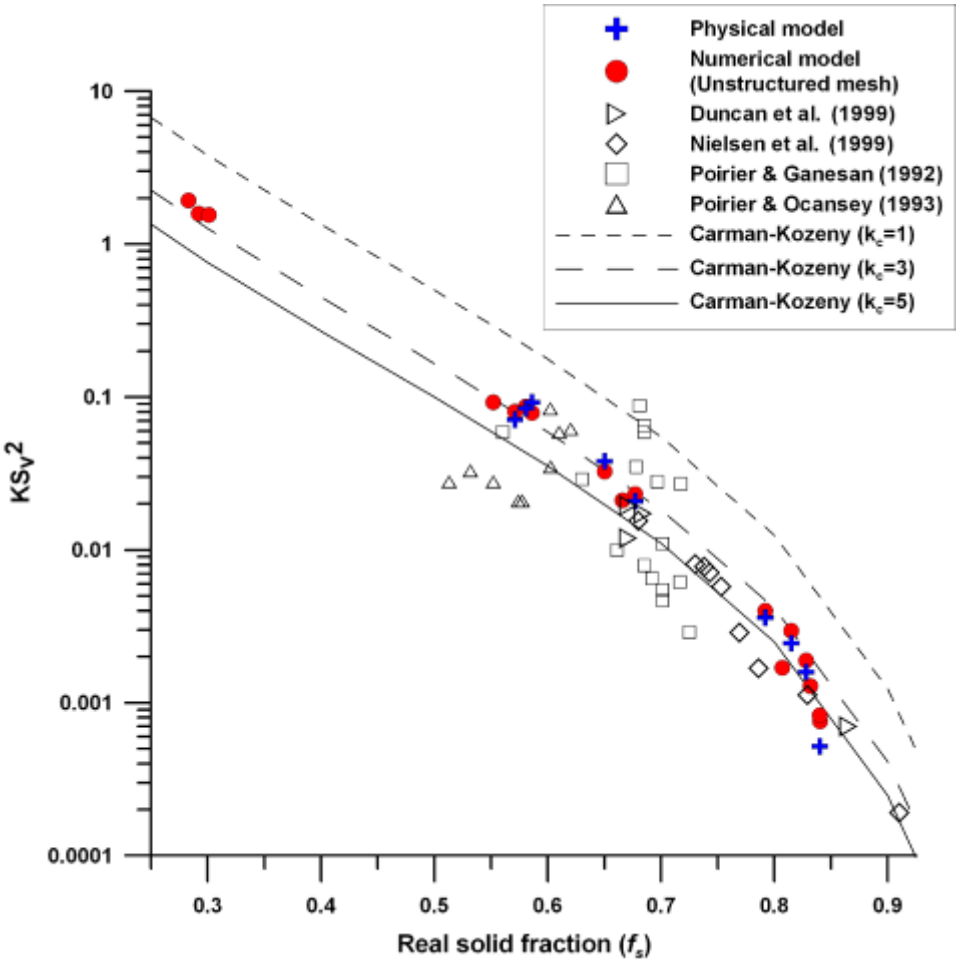

Figure 4.2 Comparison of dimensionless numerical and measured permeabilities with experimental data obtained from permeameter measurements.

It should be noted that there is considerable scatter in the experimental results (±300% as depicted in **Figure 4.2**) as discussed in [27]. The issues due to the experimental difficulties (discussed in section **1.4.2.3**) were overcome in the current work. There is a lack of experimental data at lower solid fractions due to limitations in the experimental method for determining permeability for a non-coherent dendritic network. By validating the numerically calculated permeabilities with measurements at medium to high solid fractions, the numerical technique can be applied to study permeabilities at lower solid fractions.

4.2 Permeability of equiaxed dendritic structures during solidification of Al-4.5wt%Cu

In an effort to present a predictive methodology for calculating permeability based on alloy composition and/or thermal condition, the microstructure evolution during equiaxed dendritic solidification Al-4.5wt%Cu alloy was characterized (section 2.1.2) and used for permeability determination. By comparing the permeabilities characterized by numerical and physical models with calculated values based on the Carman-Kozeny expression, it is possible to link the values of S_v^{-1} and k_C to readily available parameters in solidification models.

4.2.1 Comparison with related studies

Figure 4.3 shows the dimensionless permeabilities (average of K_{xx}, K_{yy} and K_{zz}) determined via the physical and numerical methodologies employed for this study (refer to **Table 3.2**) versus the effective solid fraction. For comparison, various results from reported conventional permeameter measurements [25, 27, 31, 36, 91], near-eutectic permeabilities of various Al-Cu alloys (section **4.1**) and lines representing the Carman-Kozeny expression with k_C equal to 1, 3 and 5 have been include in **Figure 4.3**.

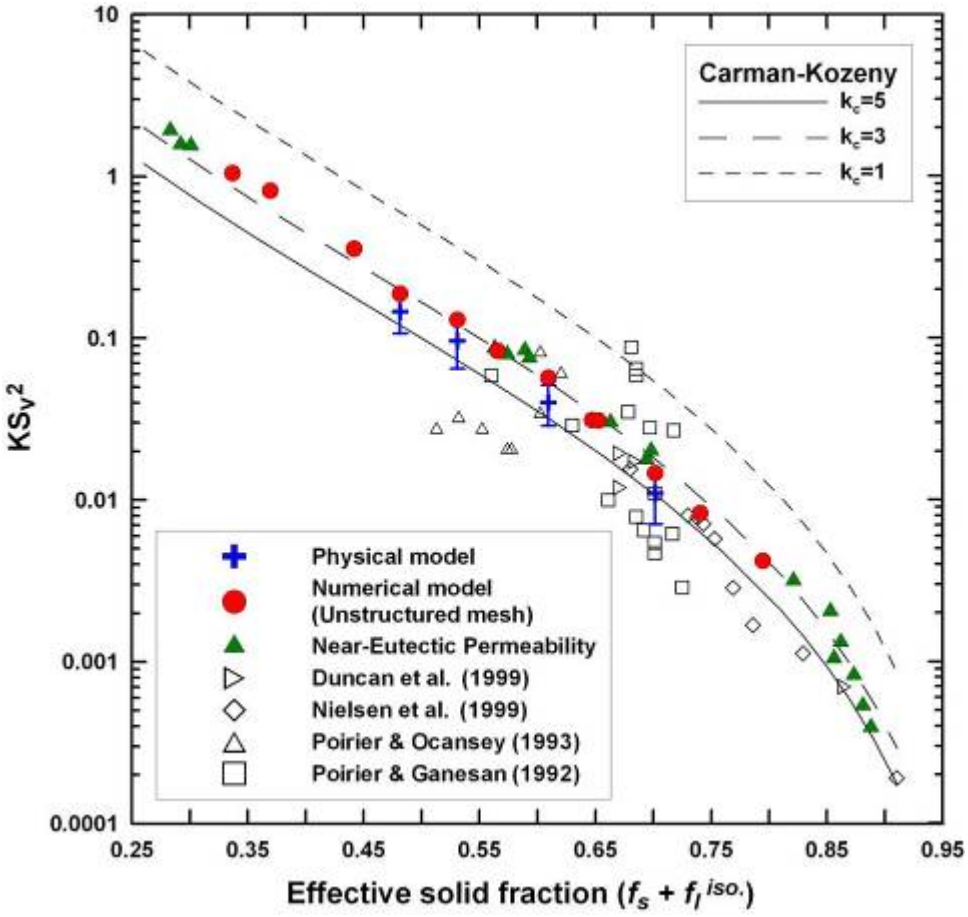

Figure 4.3 Comparison of dimensionless numerical and physical permeabilities with various reported results. Lines represent dimensionless permeability based on the Carman–Kozeny expression with k_C = 1, 3 and 5.

The two data sets (numerically and physically determined permeabilities) for Al-4.5wt% Cu are in good agreement and consistent with the near-eutectic permeabilities of various Al-Cu alloys (Section **4.1**) characterized via the same techniques. Moreover, using the effective solid fraction, the Carman-Kozeny expression with a k_C value of ~3 is found to be accurate for predicting the evolution of permeability throughout the equiaxed dendritic solidification range of this alloy.

The results of the current work are situated within the scatter of the experimental data from various reported permeameter measurements. In the available experimental results, the

microstructures were analyzed using 2D image analysis and thus the isolated liquid fractions were not quantified nor corrected for. As a result, the reported solid fractions have been used as the effective solid fraction. It should be noted that there is considerable scatter in the experimental results (i.e. a factor of six as depicted in **Figure 4.3**), which has been attributed to experimental difficulties (discussed in [37]). Using the current characterization techniques, these limitations were overcome.

4.2.2 Extension to macroscale models

Although the results of the current study suggest that k_C in the Carman-Kozeny expression is equal to ~3, there is still a need to link the value of S_v to more practical parameters available in macro-scale solidification models. As previously discussed in section **2.1.2.4.2**, the cylindrical assumption of the secondary dendrite arm shape appears to be an acceptable representation of dendritic structure and S_v in the Carman-Kozeny expression of permeability can be roughly estimated as $4 / d_2$. Moreover, d_2 was found to be proportional to the cube root of time spent in the mushy zone ($t^{1/3}$).

Using a constant value of ~3 for k_C and correlating the variation of S_v with the time spent in the mushy zone, the Carman-Kozeny expression of permeability can be linked to practical parameters available in macro-scale solidification models. **Figure 4.4** shows the permeability prediction using the Carman-Kozeny expression as a function of solidification time. To take out the dependence of solid fraction to time permeability has been normalized with solid fraction. For comparison the physically and numerically characterized permeabilities determined for the Al-4.5wt% Cu samples in this study have been included in the plot. This result suggests that the Carman-Kozeny expression, based on solid fraction and solidification time, is accurate for predicting the variation of permeability to within ±30%.

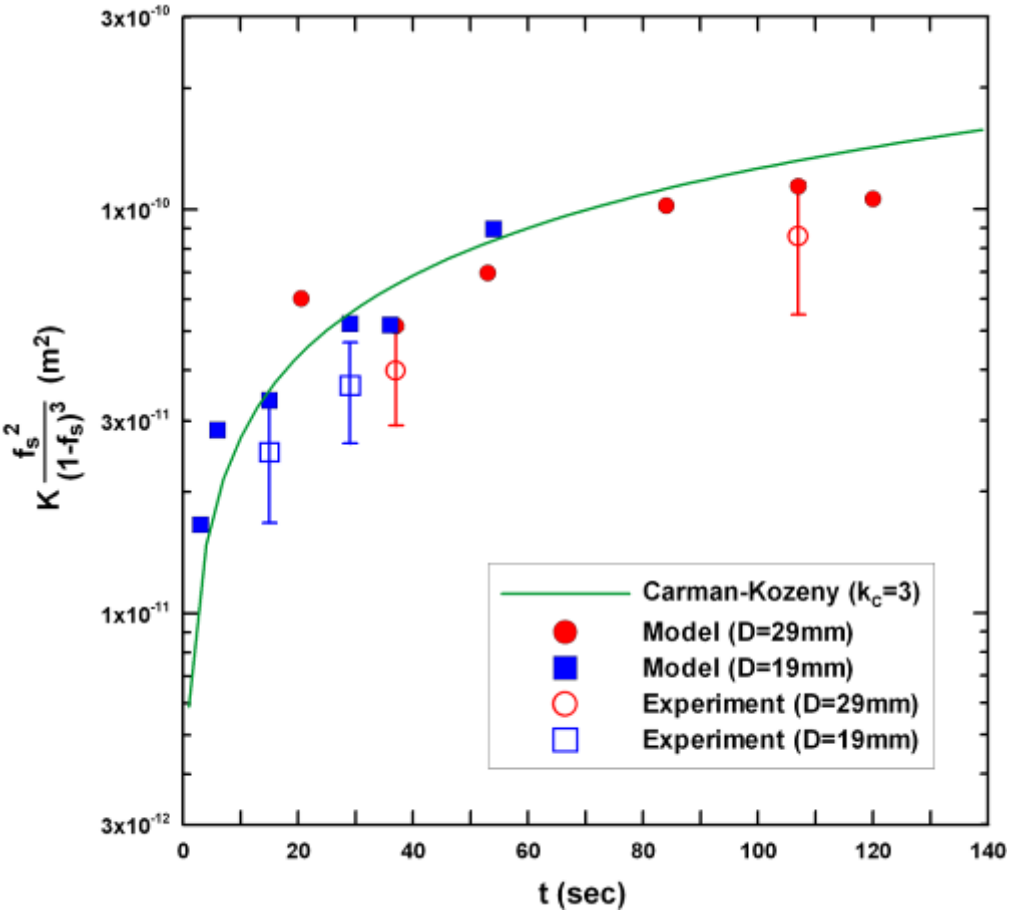

Figure 4.4 Comparison of the variation of calculated permeability based on the Carman-Kozeny expression as a function of solidification time with physically and numerically characterized permeabilities.

4.3 Summary

The evolution of permeability during the equiaxed dendritic solidification, characterized with the aid of physical and numerical determination techniques, was analyzed and compared with values calculated by the Carman-Kozeny expression. Using the effective solid fraction, the Carman–Kozeny expression with a k_C equal to ~3 was shown to be accurate for

predicting the near-eutectic permeability of Al-Cu alloys and the evolution of permeability during equiaxed solidification of Al–4.5wt%Cu.

5 Permeability of Dual Structured Hypoeutectic Aluminum Alloys[1]

As discussed in chapter 4, the Carman-Kozeny expression with a constant k_C of ~3 is suitable for predicting the permeability of equiaxed dendritic structures. However, uncertainty exists as to whether the Carman-Kozeny is applicable over the complete solidification range (from dendritic to dendritic/eutectic phases) and for a wide variation in microstructure. For example, it has been shown that k_C is equal to ~3 (refer to chapter 4) and ~5 [24] for dendritic and granular microstructures, respectively. Thus, the value of k_C is dependent on the geometry of liquid channels.

For the limiting cases where complete equiaxed dendritic or eutectic solidification occurs, the morphology of the liquid channels is either dendritic or globular, respectively. However, during equiaxed solidification of hypoeutectic aluminum alloys, eutectic grains solidify in an existing dendritic network. Hence, the geometry of liquid channels undergoes a transition from dendritic to globular. During this transition, the solidifying microstructure can be regarded as a dual structured porous medium. For an idealized dual structured porous medium, Liu et al. [93] introduced a mathematical expression, based on an analytical solution [94] to the Brinkman-Darcy equation, to describe the effective permeability of an array of square impermeable blocks placed in a fluid saturated porous medium. They focused on an equivalent continuum model and proposed a mathematical relation for determining the effective permeability. Sano et al. [95] extended Liu et al.'s [93] work to calculate the

[1] A version of this chapter has been published. Khajeh E, Maijer DM, "Permeability of dual structured hypoeutectic aluminum alloys", Acta Materialia, (2011) 59, pp. 4511-4524.

effective permeability of a porous medium with obstacles of different sizes. Both studies showed excellent agreement between the permeabilities calculated with the developed mathematical expressions and experimental measurements. These results suggest that mathematical expressions developed based on solutions to the Brinkman-Darcy equation may be applicable to non-idealized dual structured porous media.

In this chapter, a new theoretical expression for the permeability of a dual structured porous media is derived. The proposed equation describes the evolution of permeability throughout the solidification range (from equiaxed dendritic to equiaxed eutectic/dendritic) for hypoeutectic aluminum alloys.

5.1 Theory

In hypoeutectic aluminum alloys, equiaxed eutectic grains grow inside the network established by the preceding primary dendritic phase solidification. This growth sequence causes the geometry of the flow channels to evolve from dendritic to more globular. The solidifying microstructure may be treated as a dual structured porous medium and based on the solution of Brinkman-Darcy equation applied to dendritic/eutectic microstructures, a mathematical expression can be derived to predict the evolution of permeability.

5.1.1 Permeability based on Brinkman-Darcy equation

Considering a steady-state, incompressible, and very slow flow ($Re<1$) through a horizontal channel filled with a porous medium of absolute permeability K and liquid fraction f_l, the governing equation for the fully developed flow, namely the Brinkman-Darcy equation, is [93]:

$$-\frac{dp}{dx}+\frac{\mu}{f_l}\frac{d^2u}{dy^2}-\frac{\mu}{K}u=0 \qquad \textbf{Equation 5-1}$$

where p is pressure, u is local velocity, μ is the dynamic viscosity, and x and y are Cartesian coordinates parallel and normal to the direction of flow, respectively. Based on Kaviany's exact solution [96] for flow through two parallel plates, separated by a distance d, with the boundary conditions of $du/dy=0$ at the position midway between the plates and $u=0$ at the walls, the bulk velocity, u_B, is given by:

$$u_B = f_l \frac{d^2}{4\mu}(-\frac{dp}{dx})G(\theta) \qquad \textbf{Equation 5-2}$$

where

$$G(\theta) = \frac{1}{\theta^2} - \frac{\tanh(\theta)}{\theta^3} \qquad \textbf{Equation 5-3}$$

$$\theta = \frac{d}{2}\sqrt{\frac{f_l}{K}} \qquad \textbf{Equation 5-4}$$

Assuming a dual structured porous medium of liquid fraction $f_{l,t}$ consisting of Porous Medium 1 (with liquid fraction of $f_{l,1}$) in which the void space is filled with a Porous Medium 2 (with liquid fraction of $f_{l,2}$ and permeability of K_2), the superficial velocity is calculated by adopting **Equation 5-2** as:

$$\overline{u}_s = f_{l,1} f_{l,2} \frac{L_{s,1}^2}{\mu}(-\frac{dp}{dx})G(\theta) \qquad \textbf{Equation 5-5}$$

$$\theta = L_{s,1}\sqrt{\frac{f_{l,2}}{K_2}} \qquad \textbf{Equation 5-6}$$

where $L_{s,1}$ is a length scale associated with the flow channels of the Porous Medium 1. The total liquid fraction of the dual structured porous medium is:

$$f_{l,t} = f_{l,1} f_{l,2} \qquad \textbf{Equation 5-7}$$

By substituting **Equation 5-5** into the Darcy equation,

$$\overline{u}_s = -\frac{K_t}{\mu}\frac{dp}{dx} \qquad \textbf{Equation 5-8}$$

the total permeability of the dual structured porous medium is:

$$K_t = f_{l,1} f_{l,2} L_{s,1}^2 G(\theta)$$ **Equation 5-9**

The length scale, $L_{s,1}$, is proportional to the characteristic length of the flow channels in the Porous Medium 1 defined as the ratio of liquid volume, V_L, to the solid/liquid interfacial area, $A_{S/L}$. Defining $S_{v,1}$ as the solid/liquid interfacial area per unit volume of solid for Porous Medium 1, $L_{s,1}$ is given by:

$$L_{s,1} = C \frac{f_{l,1}}{(1 - f_{l,1}) S_{v,1}}$$ **Equation 5-10**

where C is a proportionality constant. Substituting (5.10) in (5.9), the total permeability is

$$K_t = C^2 \frac{f_{l,2} f_{l,1}^3}{(1 - f_{l,1})^2 S_{v,1}^2} G(\theta)$$ **Equation 5-11**

The preceding derivation has been presented in a general form to allow the structure parameters of C, $f_{l,1}$, $f_{l,2}$, $S_{v,1}$ and K_2 to be related to dendritic/eutectic microstructural parameters. Moreover, to present a comprehensive expression capable of accurately predicting the permeability for use in macroscale models, these values must be linked to practical variables available in solidification models.

5.1.2 Extension to dendritic/eutectic structure

The mathematical expression for dual structured permeability (refer to **Equation 5-11**) can be extended to describe equiaxed eutectic solidification, which is defined for this study as the instantaneous and independent heterogeneous nucleation of eutectic grains within the interdendritic spaces of a primary phase. The partially solidified microstructure (referred to as the real microstructure in **Figure 5.1**), can be treated as a network of eutectic grains overlaid by a dendritic network (referred to as the hypothetical microstructure in **Figure 5.1**).

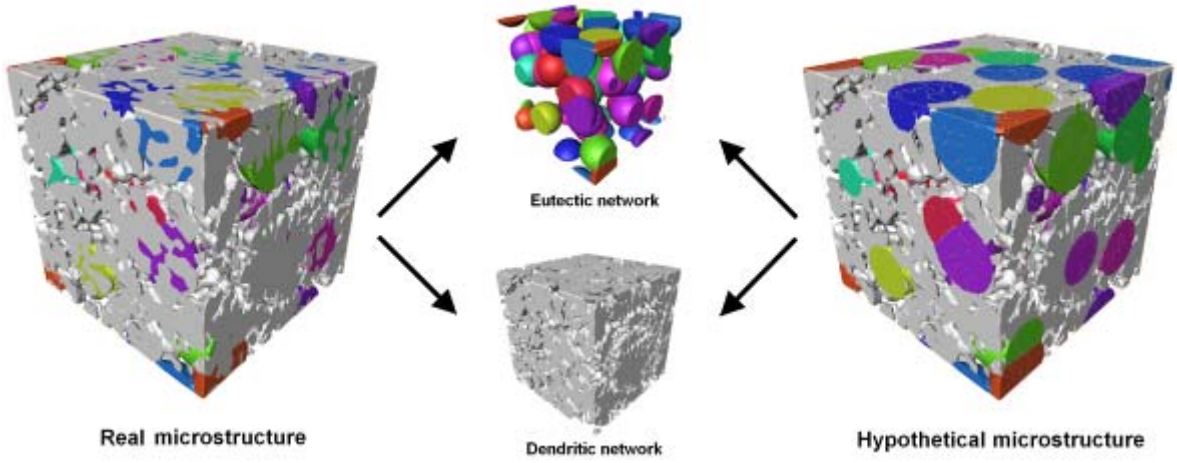

Figure 5.1 The "real microstructure" of hypoeutectic aluminum alloy during equiaxed eutectic solidification is regarded as a "dendritic network" overlaid by a "eutectic network". The "hypothetical microstructure" is defined for this analysis in which the void space of the "eutectic network" is filled with the "dendritic network". The geometries of flow channels in both real and hypothetical microstructures are the same.

Both the real and hypothetical microstructures will have the same liquid channel geometry and permeability. The permeability of the hypothetical dual structured microstructure can be studied by considering the eutectic and dendritic networks as Porous Media 1 and 2, respectively. Although the assumption that the eutectic network is Porous Medium 1 is not in keeping with the solidification sequence observed for a hypoeutectic alloy, it is has been made for mathematical convenience. The liquid fraction of the dendritic network is:

$$f_{l,d} = 1 - f_{\alpha} \qquad \textbf{Equation 5-12}$$

where f_{α} is the solid fraction of the primary (α) phase. By substituting **Equation 5-12** in **Equation 5-7**, the liquid fraction of the eutectic network is given by:

$$f_{l,e} = \frac{1 - f_{s,t}}{1 - f_{\alpha}} \qquad \textbf{Equation 5-13}$$

where $f_{s,t}$ is the total solid fraction. For the limiting case when there are no dendritic grains (i.e. an alloy of eutectic composition), $K_d \rightarrow \infty, f_{l,d} \rightarrow 1$ and $\theta \rightarrow 0$ (refer to **Equation 5-6**). For this case (refer to **Figure 5.2**),

$$\lim_{\theta \to 0} G(\theta) = \frac{1}{3} \qquad \textbf{Equation 5-14}$$

and **Equation 5-11** reduces to:

$$K_t \mid_{\theta \to 0} = \frac{C^2}{3} \frac{f_{l,e}^3}{(1 - f_{l,e})^2 S_{v,e}^2} \qquad \textbf{Equation 5-15}$$

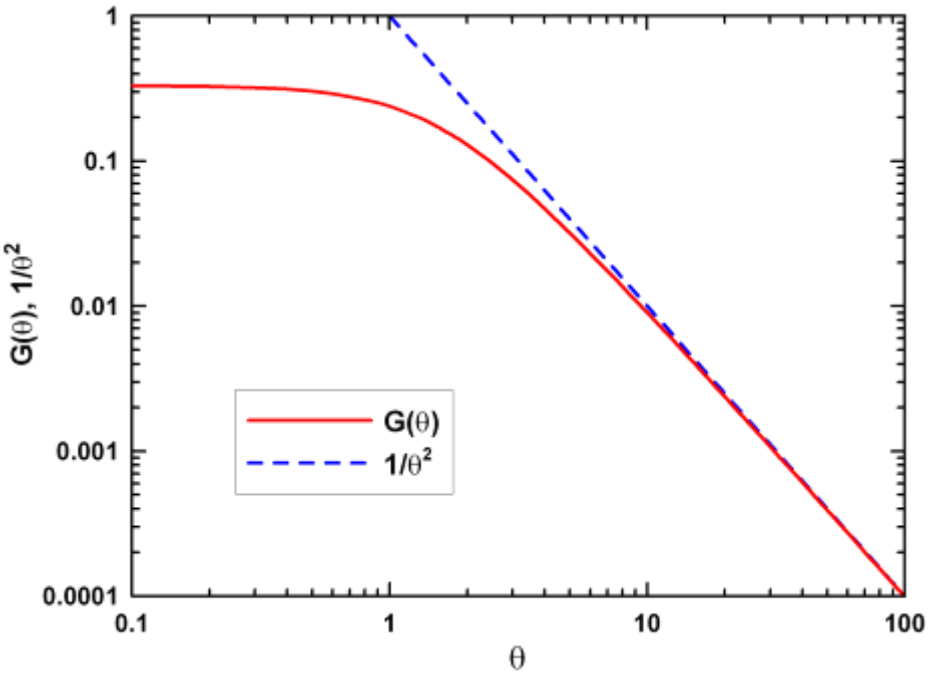

Figure 5.2 G(θ) function (refer to Equation 5-3) and $1/\theta^2$ versus θ. G(θ) is converged to 1/3 when θ→0 and $1/\theta^2$ when θ→∞.

For conditions where instantaneous nucleation occurs, all eutectic grains have the same diameter, D_e, during eutectic solidification. The empirical Carman-Kozeny equation for a packed bed can be used to describe this case [97]:

$$K_t \mid_{\theta \to 0} = \frac{f_{l,e}^3 D_e^2}{180(1 - f_{l,e})^2} \qquad \textbf{Equation 5-16}$$

Equating **Equation 5-15** and **Equation 5-16**, $C^2/3S_{v,e}^2$ is equal to $D_e^2/180$. Therefore, the total permeability of the dendritic/eutectic structure is given by:

$$K_t = \frac{f_{l,d} f_{l,e}^3 D_e^2}{60(1-f_{l,e})^2} G(\theta) \qquad \textbf{Equation 5-17}$$

where

$$\theta = \frac{f_{l,e} D_e}{7.75(1-f_{l,e})} \sqrt{\frac{f_{l,d}}{K_d}} \qquad \textbf{Equation 5-18}$$

Equation 5-18 is obtained by substituting **Equation 5-10** in to **Equation 5-6** and equating $C/S_{v,e}$ to $D_e/7.75$. With a known value of K_d, **Equation 5-17** can be used for the complete solidification range. The verification of the current mathematical expression for the limiting cases of $\theta \rightarrow 0$ and $\theta \rightarrow \infty$ are presented in section 5.2 and calculated values of permeability are then compared with permeability characterized via physical and numerical modeling.

5.1.3 Extension to equiaxed dendritic structure

The mathematical expression for the permeability of dual structured porous media (refer to **Equation 5-17**) can be employed to calculate the permeability during the solidification of hypoeutectic aluminum alloys. After developing the expression for dendritic/eutectic structures, the expression is now applied to the limiting case of primary equiaxed dendritic solidification. For this case there are no eutectic grains which results in $D_e \rightarrow 0$ and $f_{l,e} \rightarrow 1$ in **Equation 5-17**. Moreover, considering the direct proportionality of $1-f_{l,e}$ to the volume of eutectic grains, $1-f_{l,e}$ is proportional to D_e^3 . This ultimately leads to $\theta \rightarrow \infty$, $G(\theta) \rightarrow 1/\theta^2$ (refer to **Figure 5.2**) and $K_t \rightarrow K_d$. The permeability of dendritic structure, K_d, is then defined as:

$$K_d = \frac{(1-f_\alpha)^3}{k_{C,d} S_{v,d}^2 f_\alpha^2} \qquad \textbf{Equation 5-19}$$

where f_α is the instantaneous fraction of primary dendritic phase and $S_{v,d}$ is the solid/liquid

interfacial area per unit volume of dendritic structure. The validity of this equation for describing the permeability of equiaxed dendritic structures has been shown in chapter 4.

5.2 Verification of the dual structured permeability expression

The proposed mathematical expression for permeability considers the dendritic/eutectic structure as a dual structured porous medium. For the limiting case when there is no primary dendritic phase and the microstructure is made up of eutectic grains, $f_{l,d} \rightarrow 1$ and $\theta \rightarrow 0$ (i.e. a eutectic alloy). For this case, **Equation 5-17** reduces to **Equation 5-16**. The permeability of this network of eutectic grains (refer to **Figure 5.1**) was determined numerically. Fifty grains were randomly distributed and grown in a cubic domain, with 1 mm edge length. The permeability was determined for microstructures predicted with four random nuclei distributions (i.e. eutectic grains were randomly distributed four times) to assess the sensitivity to distribution. **Figure 5.3** shows the numerically determined permeabilities normalized with the eutectic grain diameter, D_e. For comparison, the line representing the dimensionless permeability has been calculated with the Carman-Kozeny expression for packed beds (refer to **Equation 5-16**). Although the numerically determined permeabilities are somewhat distribution dependent (especially at high solid fraction), the determined values are consistent with the permeabilities calculated with **Equation 5-16** for this limiting case. Further this analysis, verifies the use of the Carman-Kozeny expression for estimating the length scale in the eutectic network during the derivation of the dual structured permeability expression.

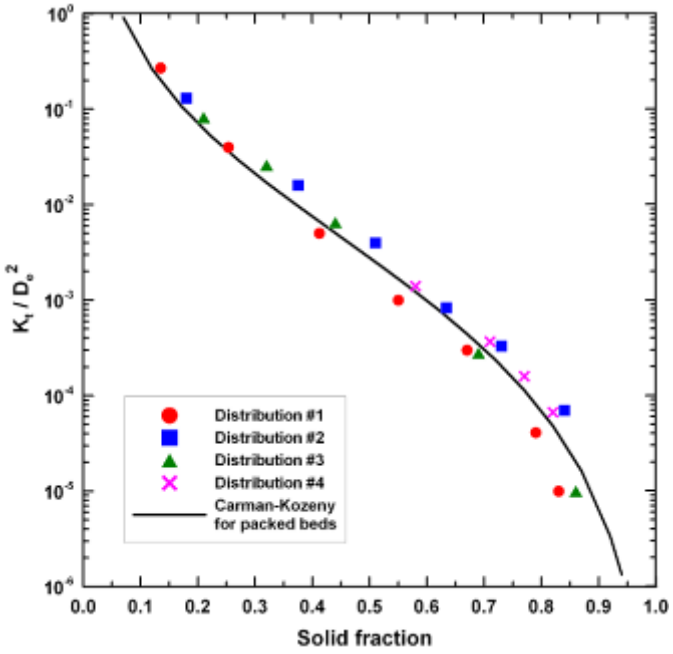

Figure 5.3 Dimensionless permeability versus solid fraction for eutectic network with four distributions of grains location. Line indicates dimensionless permeability based on the Carman-Kozeny expression for packed beds (refer to Equation 5-16).

For the other limiting case where the permeability of the eutectic network is much larger than the permeability of the dendritic network, i.e. small K_d, large D_e, and/or large $f_{l,e}$, then θ is large. For this case, as shown in **Figure 5.2**, $G(\theta)$ (refer to **Equation 5-18**) approaches $1/\theta^2$ as θ increases and the total permeability expression (refer to **Equation 5-17**) becomes:

$$K_t|_{\theta\to\infty} = f_{l,e}K_d \qquad \textbf{Equation 5-20}$$

Gerke and Van-Genuchten [98] previously developed a permeability expression to describe water flow in a structured soil system (micro-scale soil in a macro-scale rock matrix). Assuming no fracture in the rock, the problem is physically similar to the case of large θ and the dual structured permeability expression reduces to **Equation 5-20**. This equation is also in agreement with expressions proposed by Churchill and Usagi [99] and Wang et al. [100] for a composite channel when similar physics are applied.

As discussed in section 5-1-2, for the limiting case when there is no eutectic ($f_{l,e} \rightarrow 1$), $\theta \rightarrow \infty$, $G(\theta) \rightarrow 1/\theta^2$ and $K_t \rightarrow K_d$. Thus, the expression can be used to describe the evolution of permeability during primary dendritic solidification before transitioning to the dual structured case of the equiaxed dendritic/eutectic structure.

5.3 Permeability prediction via mathematical expression for hypoeutectic alloys

In this study, the evolution of permeability during equiaxed eutectic solidification has been investigated for a wide range of N_v from 0.1 to 90 mm^{-3} corresponding to low and high grain densities. As discussed in chapter 2, N_v of 90 mm^{-3} and higher were achieved using a similar material, i.e. Al-20wt%Cu, cast in the same manner. Although low grain densities were not achieved for the Al-Cu system, it has been reported that Sr additions in Al-Si alloys inhibit the nucleation of eutectic grains and dramatically decrease the eutectic grain density [101].

The modeling technique described in chapter 3 was used to produce numerically calculated permeabilities for eutectic grain densities varying from 6 to 90 mm^{-3}. **Figure 5.4** shows the calculated permeabilities (average of K_{xx}, K_{yy} and K_{zz}) versus the effective solid fraction, i.e. $f_{s,t}$ (calculated from the simulated microstructures), for N_v equal to 6, 50 and 90 mm^{-3}. For comparison, lines representing the permeabilities calculated using the mathematical expression (refer to **Equation 5-17**) for N_v equal to 0.1, 1, 6, 50, and 90 mm^{-3} have been plotted in **Figure 5.4**. This was done by extracting the variation of $f_{s,t}$ and D_e for each N_v from the simulated microstructures for use in **Equation 5-17**. As shown, the permeability values calculated by **Equation 5-17** decrease with increasing solid fraction. Moreover, as N_v increases, the permeability decreases because the tortuosity of the flow channels increases with the resulting finer microstructure. The evolution of permeability with

solid fraction described by the mathematical expression is in good agreement with the numerically calculated values of permeability. The small deviations observed are attributed to the sensitivity of numerically calculated permeability to variations in the grain distribution, as discussed in section 5-2.

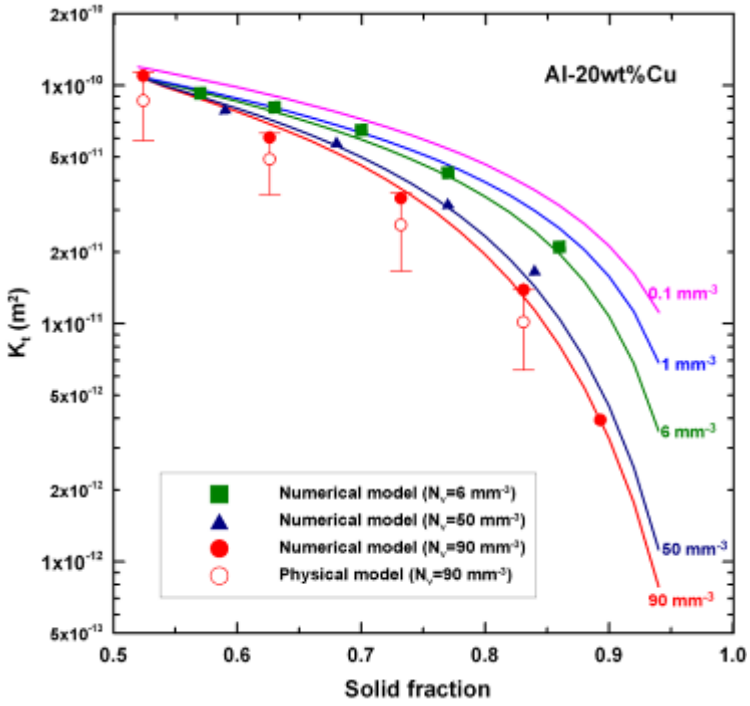

Figure 5.4 Absolute permeability versus solid fraction for Al-20wt%Cu eutectic. Closed symbols represent the numerically determined permeabilities for N_v equal to 6, 50, and 90 mm^{-3}. Open circles with error bars represent measured permeability for N_v equal to 90 mm^{-3}. Lines indicate permeability based on the Equation 5-17 for N_v equal to 0.1, 1, 6, 50, and 90 mm^{-3}.

5.4 Comparison with Carman-Kozeny expression

Figure 5.5 shows the dimensionless permeability (KS_v^2) variation versus the effective solid fraction, i.e. $f_{s,t}$, for Al with 12, 20 and 25 wt%Cu calculated with the dual structured permeability expression (**Equation 5-17**) for N_v equal to 90 and 0.1 mm^{-3}. The data necessary to create **Figure 5.5**, namely the variation of $f_{s,t}$, S_v and D_e for each N_v, was extracted from CA model predictions for each condition.

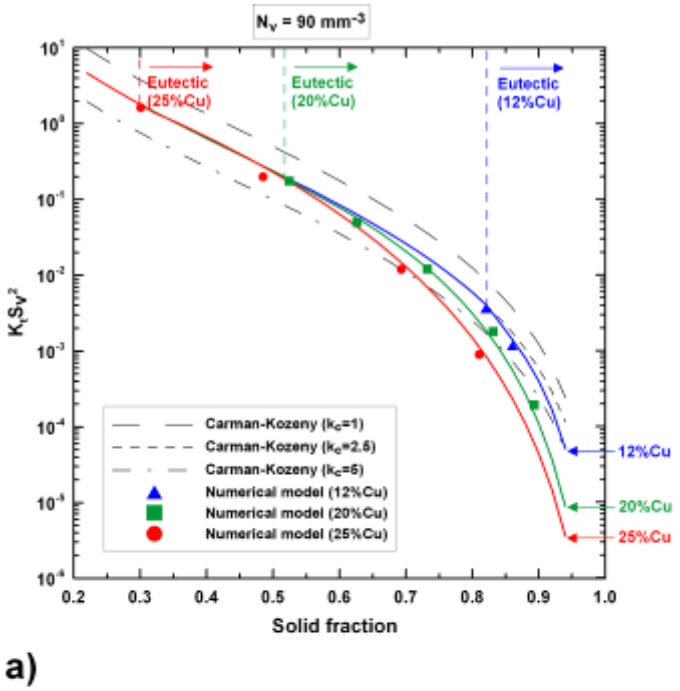

a)

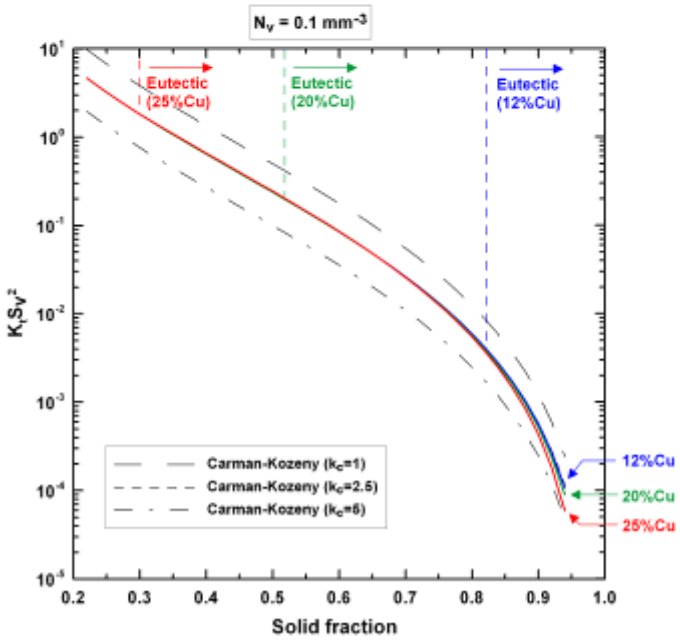

b)

Figure 5.5 Dimensionless permeability versus solid fraction for Al with 12, 20, and 25 wt%Cu alloys for N_v equal to a) 90 mm^{-3}, and b) 0.1 mm^{-3}. Symbols represent the numerically determined permeabilities. Solid lines represent calculated permeabilities from Equation 5-17 for Al with 12, 20 and 25 wt%Cu alloys and normalized with S_v obtained from triangulated microstructure, i.e. CA simulation. Dash lines indicate dimensionless permeability based on the Carman-Kozeny expression with k_C equal to 1, 2.5 and 5.

The results shown in **Figure 5.5** cover the entire solidification range from the primary dendritic solidification to the eutectic solidification event. For comparison, the dimensionless permeability, characterized numerically with N_v=90 mm^{-3}, for Al with 12 and 25 wt%Cu based on the XMT geometries presented in section 2-1-1 has been included in **Figure 5.5** along with the results for Al-20wt%Cu. Lines representing the dimensionless permeabilities calculated with the Carman-Kozeny expression (refer to **Equation 4-1**) for k_C equal to 1, 2.5 and 5 have also been included in **Figure 5.5**. As shown, the numerically calculated permeabilities and those predicted with **Equation 5-17** are in good agreement for Al with 12, 20 and 25 wt%Cu alloys with eutectic fractions ranging from 0.18 to 0.7. These results demonstrate the validity of the permeability expression for different hypoeutectic aluminum alloys with different fractions of eutectic phase.

For conditions representing primary dendritic solidification, $f_\alpha = f_{s,t}$ and the lines representing the proposed permeability expression and the Carman-Kozeny expression with constant k_C are equivalent. Additionally, the first numerical permeability characterization values for each alloy composition, presented in **Figure 5.5a**, represents the calculated permeability for the initial dendritic structure (i.e. $f_{s,e} = 0$) and is also in excellent agreement. Thus, the evolution of K_d is described by the conventional Carman-Kozeny expression by replacing f_s with f_α. In the previous chapter, the validity of this equation for describing the permeability of equiaxed dendritic structures has been shown.

During eutectic solidification, the results deviate from the Carman-Kozeny expression with constant k_C as N_v increases. With low eutectic grain density, the solid/liquid interfacial area of dendritic network is much larger than the eutectic network. The total solid/liquid interfacial area per unit volume, $S_{s,t}$ can be estimated as a function of the active solid/liquid

interfacial area of dendritic network per unit volume, $S_{s,d}$ as:

$$S_{s,t}\,|_{\theta\to\infty} = f_{l,e} S_{s,d} \qquad \textbf{Equation 5-21}$$

For low eutectic grain density, θ is large and as noted in section 5-2, the permeability converges to $f_{l,e}K_d$ (refer to **Equation 5-20**). Applying **Equation 5-11** for K_d and replacing $f_\alpha S_{v,d}$ with $S_{s,d}$, the total permeability is:

$$K_t\,|_{\theta\to\infty} = f_{l,e}\frac{(1-f_\alpha)^3}{k_{C,d}S_{s,d}^2} = f_{l,e}^3\frac{(1-f_\alpha)^3}{k_{C,d}S_{s,t}^2} = \frac{(1-f_{s,t})^3}{k_{C,d}S_{s,t}^2} \qquad \textbf{Equation 5-22}$$

Thus, for low eutectic grain density, the total permeability of dendritic/eutectic network is equivalent to Carman-Kozeny expression with constant k_C. However, the permeability deviates from the Carman-Kozeny expression as N_v increases. This highlights the impact of eutectic grain density on the transition from the Carman-Kozeny expression to the dual structured behavior of solidifying dendritic/eutectic microstructure.

The parameters describing the solidifying microstructure, and consequently the permeability behavior, are $f_{l,d}$, $f_{l,e}$, K_d, and D_e. Defined in **Equation 5-19**, θ incorporates $f_{l,d}$, $f_{l,e}$, K_d, and D_e in a single parameter. **Figure 5.6** shows the variation of θ versus solid fraction for the alloys of Al with 12, 20 and 25 wt%Cu with N_v equal to 0.1 and 90 mm^{-3}. For dendritic solidification, θ goes to infinity, however, it decreases with increasing N_v and the solid fraction during eutectic solidification. During dendritic solidification, i.e. $f_{l,e}\approx 1$, θ is very large and the total permeability is controlled by the permeability of dendritic network. As noted, this is equivalent to the Carman-Kozeny expression with constant k_C. As eutectic grains grow, θ decreases, and if / when it reaches a small value, the total permeability exhibits the dual structured behavior and is controlled by the permeability of both the dendritic and eutectic networks. However, if θ remains large, the permeability of

dendritic/eutectic structure is controlled by the permeability of active dendritic network ($f_{l,e}K_d$).

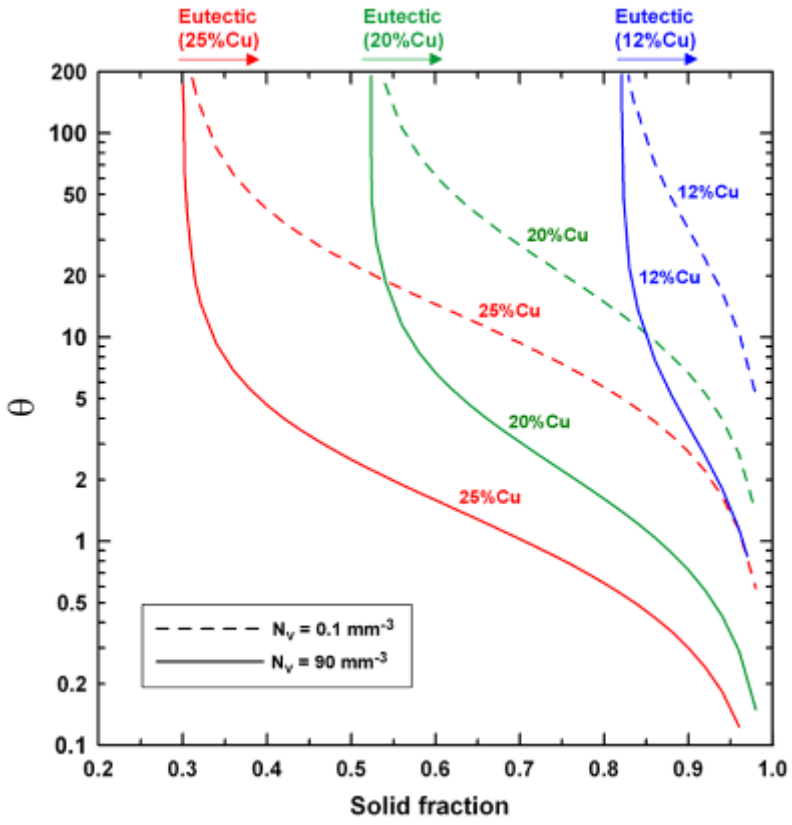

Figure 5.6 Variation of θ versus solid fraction for Al with 12, 20, and 25 wt%Cu alloys. Lines represent calculated θ from Equation 5-19 for N_v equal to 0.1 and 90 mm^{-3}.

5.5 Extension to macroscale models

In this study, a mathematical expression (refer to **Equation 5-17**) has been developed to characterize the evolution of permeability during equiaxed eutectic solidification with instantaneous nucleation. The current expression links the permeability to $f_{l,d}$, $f_{l,e}$, K_d, and D_e. The first two parameters may be obtained from the fraction of primary phase, f_α, and instantaneous solid fraction, $f_{s,t}$, according to **Equation 5-12** and **Equation 5-13**, respectively. The dendritic permeability, K_d, can be linked to the secondary dendrite arm

spacing and f_α. To calculate D_e as a function of practical parameters, the Johnson-Mehl-Avrami-Kolmogorov (JMAK) model can be employed by writing the real solid fraction in the eutectic network, $f_{s,e}$, as a function of the non-impinged solid fraction, $f_{s,e}^{\ 0}$ [73]:

$$f_{s,e} = 1 - \exp(-f_{s,e}^{0}) \qquad \textbf{Equation 5-23}$$

Assuming spherical eutectic grains, $f_{s,e}^{\ 0}$ is expressed as:

$$f_{s,e}^{0} = N_v \frac{\pi}{6} D_e^3 \qquad \textbf{Equation 5-24}$$

D_e is then given by:

$$D_e = [-\frac{6}{\pi N_v} \ln(f_{l,e})]^{\frac{1}{3}} \qquad \textbf{Equation 5-25}$$

The applicability of the JMAK model to describe the growth of spherical eutectic grains at random nucleation sites was assessed by Charbon and Rappaz [73] and was found to be appropriate for estimating D_e. By linking D_e to N_v, the mathematical expression for permeability developed in this study can be calculated with readily available parameters from solidification models.

5.6 Summary

A mathematical expression has been developed to calculate the permeability of hypoeutectic aluminum alloys for the complete solidification range (from the primary dendritic phase to the final dendritic / eutectic microstructure). The dendritic/eutectic microstructure has been treated as a dual structured porous medium consisting of a network of eutectic grains overlaid by a dendritic network (hypothetical microstructure), which is equivalent to the actual solidified microstructure. Based on the solution of the Brinkman-Darcy equation, a mathematical expression has been developed to calculate the permeability

as a function of practical parameters available in macroscale solidification models. In order to assess the accuracy of the mathematical expression, the eutectic permeability of Al-20wt%Cu alloy was characterized through physical and numerical modeling. The mathematical expression for permeability was verified for the limiting cases of $\theta \rightarrow \infty$ and $\theta \rightarrow 0$ and found to be in agreement with related studies. Comparison of the numerical and measured permeabilities showed close agreement (within ±30%) with values calculated through the mathematical expression.

The dual structured permeability expression was used to analyze the permeability evolution of three hypoeutectic Al-Cu alloys. The results showed deviation from Carman-Kozeny expression with constant k_C as N_v increases, i.e. θ decreases. The dimensionless parameter θ has been shown to significantly influence the permeability behavior of dendritic/eutectic structure. For large values of θ, the total permeability is controlled by the permeability of active dendritic network, but for small values, the total permeability has a dual behavior and is controlled by the permeability of both the dendritic and eutectic networks.

6 Concluding Remarks

This work aims to present a new theoretical expression that describes the evolution of permeability throughout the solidification range (from equiaxed dendritic to equiaxed eutectic/dendritic) for hypoeutectic aluminum alloys. The proposed theoretical expression has been verified and validated through physical and numerical modeling.

6.1 Summary and conclusions

6.1.1 Microstructure characterization

The evolution of microstructure during solidification of hypoeutectic aluminum alloys was characterized i) experimentally with the aid of XMT analysis of primary dendritic phase for different Al-Cu alloy samples solidified with different cooling rates, and ii) numerically by simulating the nucleation and growth of eutectic grains on XMT characterized map of primary phase.

Al-4.5wt%Cu castings with a range of dendritic microstructures were produced by varying the pre-solidification cooling rate and by quenching at intermediate points during solidification. Samples from these castings were characterized by XMT analysis, which allowed the pre-quench dendritic microstructure to be separated from the post-quench phases based on grey-scale. For solid fractions from 0.35 to 0.8 and for the cooling rates studied, the assumption of cylindrically shaped dendrite arms and the estimation of S_v by $4/d_2$ were shown to be acceptable. Moreover, although evidence of the coalescence mechanism of coarsening was observed, the evolution of Sv^{-1} was found to be in agreement with the

theoretical ripening model ($Sv^{-1} \propto t^{1/3}$) suggesting that ripening is the dominant mechanism of dendrite coarsening for the range of solid fraction and cooling rate studied in Al-4.5wt%Cu.

The equiaxed eutectic solidification in hypoeutectic Al–Cu alloys was also studied. A series of Al-20wt%Cu alloy castings were produced to i) analyze the evolution of solid fraction versus temperature, ii) characterize the eutectic grain structure resulting from mid-eutectic transformation quenching, and iii) determine the 3D microstructure for use as the initial condition in a CA model. XMT analysis was performed to characterize the 3D structure of the primary phase in the cast samples. The resulting 3D geometries were used to generate the computational domains for a eutectic microstructure model. By applying a stochastic nucleation approach and a deterministic CA technique to simulate the eutectic grain growth, the evolution of eutectic grains within the characterized interdendritic network was predicted. An inverse algorithm has been coupled with the CA model to extract the deterministic nucleation and growth relationships through comparison with experimental data. This inverse algorithm uses a minimization function based on a least squares calculation using the measured and predicted eutectic structure data.

A sensitivity analysis on domain size indicated that a minimum of 50 eutectic grains are necessary in a domain to obtain a reliable estimate of physical parameters. The present approach is capable of predicting the evolution of eutectic grain structure for multicomponent alloys and provides a novel technique to determine the necessary physical parameters for a deterministic microstructure model.

6.1.2 Physical and numerical characterization of permeability

The permeability of hypoeutectic Al-Cu alloys for the complete solidification range was determined through physical and numerical modeling. The physical models were large-scale

analogues of interdendritic structures produced by a rapid prototyping technique from 3D characterized microstructures. A glycerin-based working fluid was passed through the scaled replicas and the permeability was calculated from measurements of the discharge flow rate and pressure drop. Mathematical models, considering the continuity and momentum equations, were developed for the corresponding unstructured meshes of the 3D geometries used for the scaled replicas. Comparison of the numerical and measured permeabilities showed close agreement (within ±30%).

For the same sample (alloy and cast condition), the calculated permeability was significantly smaller for domains constructed from uniform mesh. Since the permeability depends directly on the tortuosity of the flow channels, using a uniform mesh increases the complexity of solid/liquid interface and results in a lower absolute permeability. These observations show the necessity of using unstructured mesh for such CFD application.

By analyzing the microstructure in 3D, it was possible to distinguish between liquid regions isolated by the solid network and separate them from those contributing to the interdendritic flow. The fraction of isolated liquid regions increases as S_v^{-1} decreases, i.e. interdendritic channels become more tortuous, and f_s increases. The analysis demonstrates that there is a considerable amount of isolated liquid at solid fractions above 0.8 which do not participate in interdendritic flow.

6.1.3 Mathematical expression for predicting the permeability

A mathematical expression has been developed to calculate the permeability of hypoeutectic aluminum alloys for the complete solidification range (from the primary dendritic phase to the final dendritic/eutectic microstructure). The dendritic/eutectic microstructure has been treated as a dual-structured porous medium consisting of a network

of eutectic grains overlaid by a dendritic network (hypothetical microstructure), which is equivalent to the actual solidified microstructure. Based on the solution of Brinkman-Darcy equation, a mathematical expression has been proposed to describe the permeability as a function of practical parameters available in macroscale solidification models. The proposed permeability expression is valid over the complete solidification range and for a wide range of compositions.

The proposed mathematical expression for permeability was verified for the limiting cases of $\theta \rightarrow \infty$ and $\theta \rightarrow 0$ and found to be in agreement with related studies. For the other limiting case of primary equiaxed dendritic solidification, the expression reduces to the conventional Carman-Kozeny expression. Comparison of the characterized permeabilities and predictions through the Carman-Kozeny expression showed that using the effective solid fraction, the Carman–Kozeny expression with a k_C equal to ~3 is accurate for predicting the permeability of equiaxed dendritic structures during solidification of Al-Cu alloys. Comparison of the characterized permeabilities during equiaxed eutectic solidification of hypoeutectic Al-Cu alloys showed close agreement (within ±30%) with values calculated through the mathematical expression.

The results of analyzing the permeability behavior of three hypoeutectic Al-Cu alloys showed a deviation from Carman-Kozeny expression with constant k_C as N_v increases, i.e. θ decreases. The dimensionless parameter θ determines the permeability behavior of dendritic/eutectic structure. For large values of θ, the total permeability is controlled by the permeability of active dendritic network, but for small values, the total permeability has a dual behavior and is controlled by the permeability of both the dendritic and eutectic networks.

6.2 Future work

To enhance the present understanding, several suggestions can be made as follow:

- Further investigation is required to characterize the evolution of the microstructural length scale (either SDAS or S_v^{-1}) during equiaxed dendritic solidification. The relationships that link the SDAS to solidification time [76] and/or cooling rate [92] are based on the assumption that dendrite coarsening occurs as a ripening phenomenon. Thus, the coalescence of dendrites as a means of coarsening and its link to process variables requires further investigation [64].
- The microstructure prediction model for equiaxed eutectic solidification was based on the assumption of a spherical eutectic grain envelope. A more accurate microstructure description could be achieved by employing a model capable of predicting the anisotropic growth of eutectic grains.
- Characterizing the evolution of permeability during coalescence of dendritic structures and as to whether a constant value of k_C is still valid should also be assessed.
- Another consideration for accurately describing the permeability is to distinguish between liquid regions isolated by the solid network and separate them from those contributing to the interdendritic flow. Hence, a straightforward way of correlating the fraction of isolated liquid regions to practical parameters is required.
- The mathematical expression for predicting the permeability of hypoeutectic aluminum alloys was developed for the case of instantaneous nucleation of eutectic grains with spherical shape. Further investigation is required to present an expression for the case of continuous nucleation and for the case of non-spherical eutectic grains.

References

[1] Zhang B, Cockcroft S, Maijer D, Zhu J, Phillion A. Casting defects in low-pressure die-cast aluminum alloy wheels. JOM Journal of the Minerals, Metals and Materials Society 2005;57:36.

[2] ASM Handbook: Casting, 1988.

[3] Flemings MC. Solidification Processing. New York: McGraw-Hill, 1974.

[4] Kubo K, Pehlke RD. Mathematical modeling of porosity formation in solidificaiton. Metallurgical Transactions B-Process Metallurgy 1985;16:359.

[5] Campbell J. On the origin of porosity in long freezing range alloys. The British Foundryman 1969;62:147.

[6] Campbell J. Castings. Oxford, UK: Butterworth-Heinemann, 2003.

[7] Santos RG, Melo M. Permeability of interdendritic channels. Materials Science and Engineering a-Structural Materials Properties Microstructure and Processing 2005;391:151.

[8] Piwonka TS, Flemings MC. Pore formation in solidification. Transactions of the Metallurgical Society of Aime 1966;236:1157.

[9] Zhu JD, Cockcroft SL, Maijer DM. Modeling of microporosity formation in A356 aluminum alloy casting. Metallurgical and Materials Transactions a-Physical Metallurgy and Materials Science 2006;37A:1075.

[10] Sabau AS, Viswanathan S. Microporosity prediction in aluminum alloy castings. Metallurgical and Materials Transactions B-Process Metallurgy and Materials Processing Science 2002;33:243.

[11] Lee PD, Chirazi A, See D. Modeling microporosity in aluminum-silicon alloys: a review. Journal of Light Metals 2001;1:15.

[12] Ampuero J, Charbon C, Hoadley AFA, Rappaz M. Modeling of microporosity evolution during the solidification of metallic alloys, in Materials Processing in the Computer Age, V.R. Voller, M.S. Stachowiez, B.G. Thomas Eds. TMS Publ., Warendale, Pennsylvania 1991; 377.

[13] M'Hamdi M, Magnusson T, Pequet C, Arnberg L, Rappaz M. Modeling of microporosity formation during directional solidification of an Al-7 % Si alloy, in Modeling of Casting, Welding and Advanced Solidification Processes, Destin, Florida, 2003; 311.

[14] Pequet C, Gremaud M, Rappaz M. Modeling of microporosity, macroporosity, and pipe-shrinkage formation during the solidification of alloys using a mushy-zone refinement method: Applications to aluminum alloys. Metallurgical and Materials Transactions a-Physical Metallurgy and Materials Science 2002;33:2095.

[15] Melo M, Rizzo EMS, Santos RG. Numerical model to predict the position, amount and size of microporosity formation in Al-Cu alloys by dissolved gas and solidification shrinkage. Materials Science and Engineering a-Structural Materials Properties Microstructure and Processing 2004;374:351.

[16] Darcy H. Les Fontaines Publiques de la ville de Dijon. Paris: Dalmont, 1856.

[17] Spittle JA, Brown SGR. A micro-model to account for hot tearing susceptibility in Al-Cu alloys, Modeling of microporosity formation during directional solidification of an Al-7 % Si alloy, in Modeling of Casting, Welding and Advanced Solidification Processes, Destin, Florida, 2003;99.

[18] Spittle JA, Brown SGR. Numerical modelling of permeability variation with composition in aluminium alloy systems and its relationship to hot tearing susceptibility. Materials Science and Technology 2005;21:1071.

[19] Carman PC. Flow of gases through porous media. London, UK: Butterworth Scientific, 1956.

[20] Gaskell DR. An introduction to transport phenomena in materials engineering: Prentice Hall, 1991.

[21] Poirier DR, Geiger GH. Transport phenomena in materials processing. US: The Minerals, Metals and Materials Society (TMS), 1994.

[22] Heinrich JC, Poirier DR. Convection modeling in directional solidification. Comptes Rendus Mecanique 2004;332:429.

[23] Brown SGR, Spittle JA, Jarvis DJ, Walden-Bevan R. Numerical determination of liquid flow permeabilities for equiaxed dendritic structures. Acta Materialia 2002;50:1559.

[24] Sun Z, Loge RE, Bernacki M. 3D finite element model of semi-solid permeability in an equiaxed granular structure. Computational Materials Science 2010;49:158.

[25] Duncan AJ, Han Q, Viswanathan S. Measurement of liquid permeability in the mushy zones of aluminum-copper alloys. Metallurgical and Materials Transactions B-Process Metallurgy and Materials Processing Science 1999;30:745.

[26] Han Q, Duncan AJ, Viswanathan S. Permeability measurements of the flow of interdendritic liquid in equiaxed aluminum-silicon alloys. Metallurgical and Materials Transactions B-Process Metallurgy and Materials Processing Science 2003;34:25.

[27] Nielsen O, Arnberg L, Mo A, Thevik H. Experimental determination of mushy zone permeability in aluminum-copper alloys with equiaxed microstructures. Metallurgical and Materials Transactions a-Physical Metallurgy and Materials Science 1999;30:2455.

[28] Poirier DR. Permeability for flow of interdendritic liquid in columnar dendritic alloys. Metallurgical Transactions B-Process Metallurgy 1987;18:245.

[29] Khajeh E, Mirbagheri SMH, Davami P. Modeling of permeability with the aid of 3D interdendritic flow simulation for equiaxed dendritic structures. Materials Science and Engineering a-Structural Materials Properties Microstructure and Processing 2008;475:355.

[30] Ocansey P, Bhat MS, Poirier DR, Finn TL. Permeability for liquid flow in the mushy zones of equiaxed castings, Light Metals 1994, Mannweiler, U., ed., The Minerals, Metals, and Materials Society, Warrendale, PA, 1994; 807.

[31] Poirier DR, Ocansey P. Permeability for flow of liquid through equiaxial mushy zones. Materials Science and Engineering a-Structural Materials Properties Microstructure and Processing 1993;171:231.

[32] Apelian D, Flemings MC, Mehrabia.R. Specific permeability of partially solidified dendritic networks of Al-Si alloys. Metallurgical Transactions 1974;5:2533.

[33] Streat N, Weinberg F. Interdendritic fluid flow in a Lead-Tin alloy. Metallurgical Transactions B-Process Metallurgy 1976;7:417.

[34] Murakami K, Shiraishi A, Okamoto T. Interdendritic fluid flow normal to primary dendrite arms in cubic alloys. Acta Metallurgica 1983;31:1417.

[35] Murakami K, Shiraishi A, Okamoto T. Fluid flow in interdendritic space in cubic alloys. Acta Metallurgica 1984;32:1423.

[36] Poirier DR, Ganesan S. Permeabilities for flow of interdendritic liquid in equiaxial structures. Materials Science and Engineering a-Structural Materials Properties Microstructure and Processing 1992;157:113.

[37] Nielsen O, Arnberg L. Experimental difficulties associated with permeability measurements in aluminum alloys. Metallurgical and Materials Transactions a-Physical Metallurgy and Materials Science 2000;31:3149.

[38] Despois JF, Mortensen A. Permeability of open-pore microcellular materials. Acta Materialia 2005;53:1381.

[39] James JD, Brown SGR, Spittle JA, Lavery NP. Experimental apparatus for validation of computer models of the permeability of metallic alloys in mushy zone. Modeling of

Casting, Welding and Solidification Processes – XI. Opio, France: The Minerals, Metals, and Materials Society (TMS), 2006. p.1189.

[40] Papathanasiou TD, Lee PD. Morphological effects on the transverse permeability of arrays of aligned fibers. Polymer Composites 1997;18:242.

[41] Bhat MS, Poirier DR, Heinrich JC. Permeability for cross flow through columnar dendritic alloys. Metallurgical and Materials Transactions B-Process Metallurgy and Materials Processing Science 1995;26:1049.

[42] Ganesan S, Chan CL, Poirier DR. Permeabilities for flow parallel to primary dendrite arms. Materials Science and Engineering a-Structural Materials Properties Microstructure and Processing 1992;151:97.

[43] Bernard D, Nielsen O, Salvo L, Cloetens P. Permeability assessment by 3D interdendritic flow simulations on microtomography mappings of Al-Cu alloys. Materials Science and Engineering a-Structural Materials Properties Microstructure and Processing 2005;392:112.

[44] Madison J, Spowart J, Rowenhorst D, Aagesen LK, Thornton K, Pollock TM. Modeling fluid flow in three-dimensional single crystal dendritic structures. Acta Materialia 2010;58:2864.

[45] Wojnar L. Image analysis: applications in materials engineering: CRC Press, 1999.

[46] Herbert MJ, Jones CB. Contour correspondence for serial section reconstruction: complex scenarios in palaeontology. Computers & Geosciences 2001;27:427.

[47] Yanuka M, Dullien FAL, Elrick DE. Serial sectioning and digitization of porous media for two dimensional and three dimensional analysis and reconstruction. Journal of Microscopy-Oxford 1984;135:159.

[48] Moss VA, Jenkinson DM, Elder HY. Automated image segmentation and serial section reconstruction in microscopy. Journal of Microscopy-Oxford 1990;158:187.

[49] Alkemper J, Voorhees PW. Quantitative serial sectioning analysis. Journal of Microscopy-Oxford 2001;201:388.

[50] Alkemper J, Voorhees PW. Three-dimensional characterization of dendritic microstructures. Acta Materialia 2001;49:897.

[51] Kral MV, Spanos G. Three dimensional morphology of cementite precipitates. Scripta Materialia 1997;36:875.

[52] Li M, Ghosh S, Richmond O. An experimental-computational approach to the investigation of damage evolution in discontinuously reinforced aluminum matrix composite. Acta Materialia 1999;47:3515.

[53] Li M, Ghosh S, Richmond O, Weiland H, Rouns TN. Three dimensional characterization and modeling of particle reinforced metal matrix composites part II: damage characterization. Materials Science and Engineering a-Structural Materials Properties Microstructure and Processing 1999;266:221.

[54] Li M, Ghosh S, Richmond O, Weiland H, Rouns TN. Three dimensional characterization and modeling of particle reinforced metal matrix composites: part I - Quantitative description of microstructural morphology. Materials Science and Engineering a-Structural Materials Properties Microstructure and Processing 1999;265:153.

[55] Madison J, Spowart J, Rowenhorst D, Pollock T. The three-dimensional reconstruction of the dendritic structure at the solid-liquid interface of a Ni-based single crystal. JOM Journal of the Minerals, Metals and Materials Society 2008;60:26.

[56] ROBO-MET.3D documentaion.

[57] Salvo L, Cloetens P, Maire E, Zabler S, Blandin JJ, Buffiere JY, Ludwig W, Boller E, Bellet D, Josserond C. X-ray micro-tomography an attractive characterisation technique in materials science. Nuclear Instruments & Methods in Physics Research Section B-Beam Interactions with Materials and Atoms 2003;200:273.

[58] Watson IG, Lee PD, Dashwood RJ, Young P. Simulation of the mechanical properties of an aluminum matrix composite using X-ray microtomography. Metallurgical and Materials Transactions a-Physical Metallurgy and Materials Science 2006;37A:551.

[59] Bernard D, Gendron D, Heintz JM, Bordere S, Etourneau J. First direct 3D visualisation of microstructural evolutions during sintering through X-ray computed microtomoaraphy. Acta Materialia 2005;53:121.

[60] Babout L, Maire E, Buffiere JY, Fougeres R. Characterization by X-ray computed tomography of decohesion, porosity growth and coalescence in model metal matrix composites. Acta Materialia 2001;49:2055.

[61] Maire E, Buffiere JY, Salvo L, Blandin JJ, Ludwig W, Letang JM. On the application of X-ray microtomography in the field of materials science. Advanced Engineering Materials 2001;3:539.

[62] Maire E, Grenier JC, Daniel D, Baldacci A, Klocker H, Bigot A. Quantitative 3D characterization of intermetallic phases in an Al-Mg industrial alloy by X-ray microtomography. Scripta Materialia 2006;55:123.

[63] Stock SR. X-ray microtomography of materials. International Materials Reviews 1999;44:141.

[64] Limodin N, Salvo L, Boller E, Suery M, Felberbaum M, Gailliegue S, Madi K. In situ and real-time 3-D microtomography investigation of dendritic solidification in an Al-10 wt.% Cu alloy. Acta Materialia 2009;57:2300.

[65] Boettinger WJ, Warren JA, Beckermann C, Karma A. Phase-field simulation of solidification. Annual Review of Materials Research 2002;32:163.

[66] Brown SGR, Spittle JA. Computer simulation of grain growth and macrostructure development during solidification. Materials Science and Technology 1989;5:362.

[67] Spittle JA, Brown SGR. Computer simulation of the effects of alloy variables on the grain structures of castings. Acta Metallurgica 1989;37:1803.

[68] Rappaz M, Gandin CA, Desbiolles JL, Thevoz P. Prediction of grain structures in various solidification processes. Metallurgical and Materials Transactions a-Physical Metallurgy and Materials Science 1996;27:695.

[69] Stefanescu DM. Science and Engineering of Casting Solidification. US: Springer, 2009.

[70] Hesselbarth HW, Gobel IR. Simulation of recrystallization by cellular automata. Acta Metallurgica Et Materialia 1991;39:2135.

[71] Rappaz M, Gandin CA. Probabilistic modeling of microstructure formation in solidification processes. Acta Metallurgica Et Materialia 1993;41:345.

[72] Gandin CA, Rappaz M, Tintillier R. 3-dimensional probabilistic simulation of solidification grain structures - application to superalloy precision castings. Metallurgical Transactions a-Physical Metallurgy and Materials Science 1993;24:467.

[73] Charbon C, Rappaz M. 3D probabilistic modeling of equiaxed eutectic solidification. Modelling and Simulation in Materials Science and Engineering 1993;1:455.

[74] Charbon C, LeSar R. A 2D stochastic micro-macro model of equiaxed eutectic solidification. Modelling and Simulation in Materials Science and Engineering 1997;5:53.

[75] Oldfield W. A quantitative approach to casting solidification - freezing of cast iron. Asm Transactions Quarterly 1966;59:945.

[76] Kurz W, Fisher DJ. Fundamentals of Solidification. US: Trans Tech Publications Ltd, 1998.

[77] Jackson KA, Hunt JD. Lamellar and rod eutectic growth. Transactions of the Metallurgical Society of Aime 1966;236:1129.

[78] Jones H, Kurz W. Relation of interphase spacing and growth temperature to growth velocity in Fe-C and Fe-Fe3C eutectic alloys. Zeitschrift Fur Metallkunde 1981;72:792.

[79] Maijer D, Cockcroft SL, Patt W. Mathematical modeling of microstructural development in hypoeutectic cast iron. Metallurgical and Materials Transactions a-Physical Metallurgy and Materials Science 1999;30:2147.

[80] Yang BJ, Stefanescu DM, Leon-Torres J. Modeling of microstructural evolution with tracking of equiaxed grain movement for multicomponent Al-Si alloy. Metallurgical and Materials Transactions a-Physical Metallurgy and Materials Science 2001;32:3065.

[81] Aravind M, Yu P, Yau MY, Ng DHL. Formation of Al2Cu and AlCu intermetallics in Al(Cu) alloy matrix composites by reaction sintering. Materials Science and Engineering a-Structural Materials Properties Microstructure and Processing 2004;380:384.

[82] Rohatgi PK, Adams CM. Colony and dendritic structures produced on solidification of eutectic Al-Cu alloy. Transactions of the Metallurgical Society of Aime 1969;245:1609.

[83] Abbaschian R, Abbaschian L, Reed-Hill RE. Physical Metallurgy Principles: Cengage Learning, 2008.

[84] Braquelaire A, Lachaud JO, Vialard A. Discrete Geometry for Computer Imagery: LNCS 2301, 2002.

[85] Young KP, Kirkwood DH. Dendrite arm spacings of Al-Cu alloys solidified under steady-state conditions. Metallurgical Transactions 1975;6:197.

[86] Terzi S, Salvo L, Suery M, Dahle AK, Boller E. Coarsening mechanisms in a dendritic Al-10% Cu alloy. Acta Materialia 2010;58:20.

[87] Stefanescu DM, Upadhya G, Bandyopadhyay D. Heat transfer solidification kinetics modeling of solidification of castings. Metallurgical Transactions a-Physical Metallurgy and Materials Science 1990;21:997.

[88] Emadi D, Whiting LV, Nafisi S, Ghomashchi R. Applications of thermal analysis in quality control of solidification processes. Journal of Thermal Analysis and Calorimetry 2005;81:235.

[89] Russ JC. Practical Stereology. New York: Plenum Press, 1986.

[90] ANSYS ICEM CFD 11.0 documentation.

[91] Khajeh E, Maijer DM. Physical and numerical characterization of the near-eutectic permeability of aluminum-copper alloys. Acta Materialia 2010;58:6334.

[92] Chen M, Kattamis TZ. Dendrite coarsening during directional solidification of Al-Cu-Mn alloys. Materials Science and Engineering a-Structural Materials Properties Microstructure and Processing 1998;247:239.

[93] Liu J, Sano Y, Nakayama A. A simple mathematical model for determining the equivalent permeability of fractured porous media. International Communications in Heat and Mass Transfer 2009;36:220.

[94] Nakayama A, Koyama H, Kuwahara F. An analysis on forced convection in a channel filled with a Brinkman-Darcy porous medium - exact and approximate solutions. Warme Und Stoffubertragung-Thermo and Fluid Dynamics 1988;23:291.

[95] Sano Y, Noguchi K, Kuroiwa T. An Experimental Investigation into the Effective Permeability of Porous Media whose Matrices are Composed of Obstacles of Different Sizes. The Open Transport Phenomena Journal 2009;1:15.

[96] Kaviany M. Laminar flow through a porous channel bounded by isothermal parallel paltes. International Journal of Heat and Mass Transfer 1985;28:851.

[97] Dullien FAL. Porous Media: Fluid Transport and Pore Structure. New York: Academic Press, 1979.

[98] Gerke HH, Vangenuchten MT. A dual-porosity model for simulating the preferential movement of water and solutes in structured porous media. Water Resources Research 1993;29:305.

[99] Churchil.Sw, Usagi R. General expression for correlation of rates of transfer and other phenomena. Aiche Journal 1972;18:1121.

[100] Wang CY, Ahuja S, Beckermann C, Degroh HC. Multiparticle interfacial drag in equiaxed solidification. Metallurgical and Materials Transactions B-Process Metallurgy and Materials Processing Science 1995;26:111.

[101] McDonald SD, Nogita K, Dahle AK. Eutectic grain size and strontium concentration in hypoeutectic aluminium-silicon alloys. Journal of Alloys and Compounds 2006;422:184.